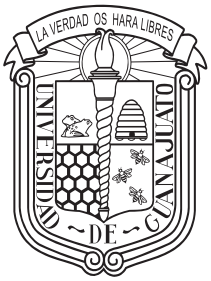

UNIVERSIDAD DE GUANAJUATO

Campus Irapuato-Salamanca
División de Ingenierías
Departamento de Ingeniería Mecánica

A novel kinematic knee model as a parallel mechanism for computing ligament length variations

THESIS
to obtain the degree of
MASTER IN MECHANICAL ENGINEERING
presenting

Mauricio Arredondo Soto

Advisors:
Dr. Mario A. García Murillo
Dr. Agustín Vidal Lesso

Salamanca, Gto., August, 2019

Dedicado a mi familia,
especialmente a mi madre.

Acknowledgments

I would like to thank to the National Council for Science and Technology (CONACyT) for the sponsorship provided during my whole Masters degree.

I want to specially thank Dr. Mario A. García Murillo for giving me the opportunity to work with him developing this project, and for being, in addition to my advisor, my friend. I also want to thank Dr. Agustín Vidal Lesso for the support that he gave me as my co-advisor.

I want to thank the professors of the Dynamics and Robotics department, who taught me in my Master's coursework. I want to give special thanks to Dr. José Ma. Rico Martínez for helping me to discover my passion for dynamics and for the support and advisement during the bachelors.

Thanks to all the people who helped me in some way to make this thesis possible. Professors; Dr. Luz A. Aguilera, Dr. José Colín, Dr. Roberto Rojas, Dr. Julián M. Estudillo, Dr. Edgar Alvarado and Dr. Diego A. Nuñez. And Friends; Fernando, Camilo, Carlos, Charlie, Esteban, Alan, Juan Carlos and Amatista.

I would also like to thank Dr. Dario Villarreal for giving me the opportunity to participate in a summer research program at the Southern Methodist University.

Finally, but not least important, I want to thank to my parents Ofelia and Victor, and my sister Hannia, who provided me with unconditional love, comprehension and support. I will never disappoint you. To my life partner Ma. Gabriela for the love granted to me during my Master's degree. And to my family; uncle Armando, aunt Alicia, grandma Rosa, ... to everyone. You were always there for me in the good and in the bad times.

Abstract

Measurement of the knee motion and the computing of its geometrical parameters is a complex task that requires the use of specialized facilities and equipment to perform data acquisition, as well as clinicians with training in physiology to place the markers correctly on anatomical landmarks. Additionally, the existing kinematic knee models have important limitations in their ability to reproduce complex movements different than pure flexion-extension, since their mobility have been limited to 1-DoF. The architecture of these models has evolved over the years from the planar mechanisms to the recent spatial parallel platforms, improving their capability to reproduce spatial movements of the knee, but only during passive motion. Moreover, these models take the ligaments as isometric links, therefore, not allowing to simulate their actual behavior.

In order to overcome the drawbacks, a photogrammetric measurement system is proposed, which uses only one camera and two planar patterns to extract 3D kinematic data. An accuracy study of the measurement system was developed to ensure the reliability of it. With this mesurement system, a new experimental procedure to acquire the work-space of three motion tasks (passive flexion-extension, passive internal-external rotation and semi-active flexion-extension) and compute the geometrical parameters of the knee is proposed.

Then, a new kinematic knee model as a parallel platform with 4-DoF and a RRPP+4-SPS architecture with high anatomic significance is proposed, which is capable of reaching a subject-specific flexion work-space obtained experimentally as well as being able to simulate the ligament length variations of: ACL PCL MCL and LCL by the distance between the spherical pairs in the SPS kinematic chains. Likewise, the inverse kinematic analysis by means of the Denavit-Hartenberg notation and the mobility analysis are presented for the proposed kinematic knee model. Finally, an optimization process is developed to set the ligament length variation curves of the model as the prescribed ones taken from the literature.

Two examples of the kinematic knee model before and after the optimization process have been validated by the computer software Solidworks®.

Key words: **kinematic knee model**, **measurement system**, **motion task**, **optimization process**, **ligament length variation**.

Resumen

La medición de los movimientos de la rodilla y el cálculo de sus parámetros geométricos es una tarea compleja que requiere de instalaciones y equipo especializado para realizar la adquisición de datos, así como de clínicos con entrenamiento en fisiología para posicicionar correctamente los marcadores en posiciones estratégicas del cuerpo. Adiciconalmente, los modelos cinemáticos de rodilla que existen actualmente tienen limitaciones importantes en su habilidad para emular movimientos complejos además de solo flexión-extensión, ya que su movilidad está restringida a 1-GdL. La arquitectura de los modelos ha evolucionado a través de los años, desde los mecanismos planos hasta los de plataformas paralellas propuestos recientemente, mejorando su capacidad de reproducir movimientos espaciales de la rodilla, aunque solo durante movimiento pasivo. Además, estos modelos asumen los ligamentos como elementos isométricos, lo que no permite simular su comportamiento real.

Con el fin de superar estos inconvenientes, se propone un sistema de medición basado en fotogrametría, el cual usa una sola cámara y dos patrones planos para extraer datos cinemáticos en 3D. Se realizó un estudio de precisión para asegurar la confiabilidad del sistema. Con este sistema de medición se propone además un nuevo procedimiento experimental para medir el espacio de trabajo de la rodilla durante tres tareas de movimiento (flexión-extensión pasiva, rotación interna-externa pasiva y flexión semi-activa) y calcular sus sus parámetros geométricos.

Entonces, se propone un nuevo modelo cinemático de rodilla, como una plataforma parallela con 4-GdL y arquitectura RRPP+4-SPS con significancia anatómica, capaz de emular un espacio de trabajo de flexión específico de un paciente obtenido experimentalmente, así como de simular variaciones de longitud de los ligamentos: ACL, PCL, MCL y LCL, a través de las distancias ente los pares esféricos de las cadenas cinemáticas SPS. De igual manera, se presenta el análisis cinemático inverso mediante notación de Denavit-Hartenberg y el análisis de movilidad. Finalmente, se desarrolla un proceso de optimización para obtener curvas de variones de longitud de los ligamentos similares a unas pre-escritas tomadas de la literatura.

Dos ejemplos del modelo cinemático de rodilla antes y después del proceso de optimización han sido validados mediante el software SolidWorks®.

Palabras clave: **modelo cinemático de rodilla**, **sistema de medición**, **tarea de movimiento**, **proceso de optimización**, **variaciones en la longitud de los ligamentos**.

Contents

List of Figures

List of Tables

Nomenclature

Acronyms

MT	Motion task.
STA	Soft tissue artifact.
MKO	Multibody kinematic optimization.
SVD	Singular value decomposition.
ISB	International society of biomechanics.
FEA	Flexion-extension axis.
WS	Work-space.
SPM	Spatial parallel mechanism.
DoF	Degree of Freedom.
ACL	Anterior cruciate ligament.
PCL	Posterior cruciate ligament.
MCL	Medial collateral ligament.
LCL	Lateral collateral ligament.
TF	Tibio-femoral.
PF	Patello-femoral.
FCS	Femur coordinate system.
TCS	Tibia coordinate system.
DH	Denavit-Hartenberg.

Notation

S	Spherical pair.
R	Revolute pair.
P	Prismatic pair.
U	Universal pair.
$\mathbf{J}(\boldsymbol{u})$	Jacobian matrix.
$\boldsymbol{d}(\boldsymbol{u})$	Vector of residuals.
$\boldsymbol{u}$	Vector of variables to optimize.
$\hat{\boldsymbol{n}}$	Vector perpendicualr to the plane.
T	Spatial coordinate system.
${}^{A}\mathbf{R}^{B}$	Rotation matrix of the system B relative to the system A.
${}^{A}\boldsymbol{t}^{B}$	Translation vector of the system B relative to the system A.
${}^{A}\mathbf{T}^{B}$	Homogeneous transform of the system B relative to the system A.
\$	Screw.
S	Screw line.
$\hat{\boldsymbol{s}}$	Line axis.
$\boldsymbol{s}_O$	Line moment about the origin.
$\boldsymbol{b}$	Rodrigues's vector.
$\mathrm{C}\theta$	$\cos\theta$.
$\mathrm{S}\theta$	$\sin\theta$.
θ, d, α, a	Denavit-Hartenberg parameters.
$\mathbf{A}$	Intrinsic matrix of the camera.
α, β	Focal length parameters.
γ	Skewness.
$\mathbf{H}$	Homography matrix.
s	Standard deviation.
s_r	Standard deviation of the repeatability.
s_R	Standard deviation of the reproducibility.

Chapter 1

Introduction

The knee is one of the largest and most complex joints in the body. It is essential in the human life because it allows a number of important functions [8], such as:

- supports the body in upright position without muscles having to work,
- helps in lowering and raising body e.g. sitting, climbing and squatting,
- allows rotation/twisting of the leg to place and position foot accurately,
- makes walking more efficient,
- acts with the ankle joint as a strong forward propeller of the body - particularly important when running,
- provides stability and proprioception of the leg,
- acts as a shock absorber.

In addition, the knee faces the mechanical challenge of reconciling two contradictory requirements: 1) to have great stability in full extension when the knee is severely stressed and 2) to display great mobility in flexion, as needed for running and for the optimal orientation of the foot relative to the irregularities of the ground. The knee solves these problems by using highly ingenious mechanical devices such as: ligaments, menisci, cartilage, tendons, muscles and articular surfaces. However, this complex system renders the knee liable to injuries, such as; chondromalacia patella, knee osteoarthritis, meniscal tear, cruciate ligament strain or tear, medial collateral ligament strain or tear, patellar subluxation, patellar tendonitis, etc. [9]. In severe cases, surgery may be necessary. Whether it was just a knee injury or a surgery, some type of physical therapy is always necessary to get the strength back and put the patient on the road to recovery.

Therefore, a deep and precise knowledge of the kinematic good behavior of the knee joint becomes essential to ensure full recovery, prevent injuries and stop problems coming back. In addition, a kinematic knee model is very important since it allows the design and evaluation of the physical therapy processes such as rehabilitation tasks before being implemented in real patients, in order to improve and expedite the recovery.

The present work has two principal topics, **Determination of geometrical parameters of the knee** and **Synthesis of a kinematic knee model**.

These topics are intimately related since a new kinematic knee model must be evaluated with some reference to the real knee motion. In this particular case the final kinematic knee model is tested by its capability to reproduce the knee work-space experimentaly obtained.

The present work is focused in the passive and semi-active motions of the knee joint, that is, the motion of the joint under virtually unloaded conditions i.e. totally assisted motion and self-motion without external loads.

1.1 Review: Knee motion measurements

Historically, researchers have been interested in measuring the knee movements. The first attemps were focused only in flexion-extension motion in the sagittal plane [10, 11], since it is the main movement of the knee. Then, in the past two decades, the research has focused on measuring the 3-Dimensional body segment position and orientation (altogether hereinafter also referred to as 'pose') of the femur bone and the tibia and fibula skeletal structure, and their relative displacements during the execution of different motor tasks, some studies also include the movement of the patella relative to the femur. The most common methods for tracking the body segments are: the use of wearable sensors as accelerometers or gyroscopes [12, 13], 3D laser reconstruction [14] and the use of photogrammetric systems [15], by far the most widespread technique used. When a photogrammetric technique is used as a measurement system it is necessary a set of reflective markers to reconstruct the 3D coordinate frame systems relative to a global system.

The measurements can be performed *in vitro* (cadaver specimens) or *in vivo* (patients and volunteers). Since the real target of the motion analysis are the bones or skeletal structures, the *in vitro* data is more reliable because the markers can be attached directly to the bones as is shown in the Figure 1.1, which is no possible for *in vivo* experiments.

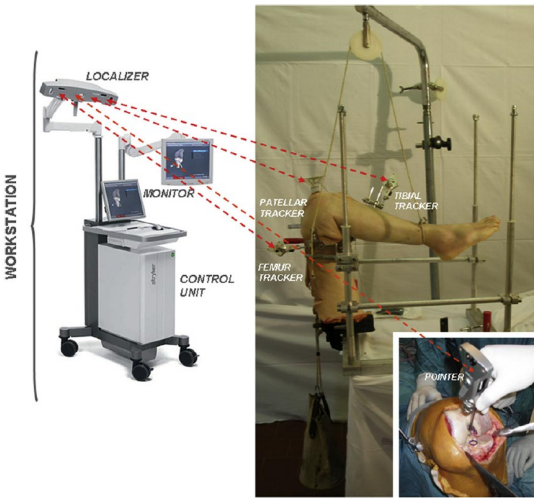

Figure 1.1: Experimental setup for the measurement of 3D knee movements in a cadaveric specimen. Figure extracted from [7].

Historically, *in vivo* experiments have been destinated to gait analysis, see Figure 1.2. In addition, it has to deal with stuck the reflective markers on the skin in correspondence with target anatomical landmarks, axes or planes, according to specific protocols and conventions [16, 17], and mainly with the interposition of soft tissue between the markers and the internal bones, which can be as large as a few centimeters [18].

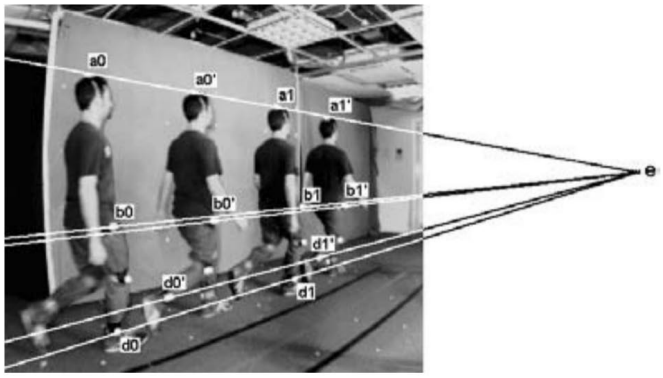

Figure 1.2: Image matching similar phase poses during a gait analysis. Figure extracted from [19].

Soft tissue motion results in deformation of the relevant cluster markers, as well as in its rigid displacement with respect to the underlying bones, these deformations and displacements are associated to muscle contraction and relaxation, to gravitational and inertial effects and also to skin sliding. Soft tissue artifact (STA) is particularly critical during active movement of the human body (external loads acting on the articulations of the body), as it happens in the gait. STA does affect final gait measurements more than the instrumental error derived from the photogrammetric systems [20] and more than the likely erroneous identification of the anatomical landmarks by the operator [21], making of STA the main error source in the motion analysis of the human body.

1.1.1 Reducing the STA

Many are the studies in the literature reporting attempts to reduce STA specially during gait analysis. These attempts range from the basic recommendations to optimization techniques via segmental or global approaches, using joint models. The latter is here referred to as multibody kinematic optimization (MKO). From another perspective, many studies have defined biomechanical models able to reproduce joint kinematics that have been applied to MKO approaches [22].

Here is a summary of the principal techniques to reduce STA through the last years. The basic recommendations are good practices carried out by most researchers when they perform a human motion analysis using photogrammetric techniques to reduce the STA, for instance, the use of elastic bands to rigidity the skin and place the markers on it [23–25] or place the markers far from the human joints where STA is greater [23]. Akbarshani et al. [26] made an experimental study with ten reflective markers placed on different positions of the thigh and shank, see Figure 1.3, in which they compared the STA magnitude of each marker during some motion tasks. In general, markers positioned in the first third of the thigh and the mid anterior aspect of the shank showed the less STA [26]. Moreover,

markers located on plates that were strapped to the body segments showed less undesirable movements than the skin mounted markers. [23, 26].

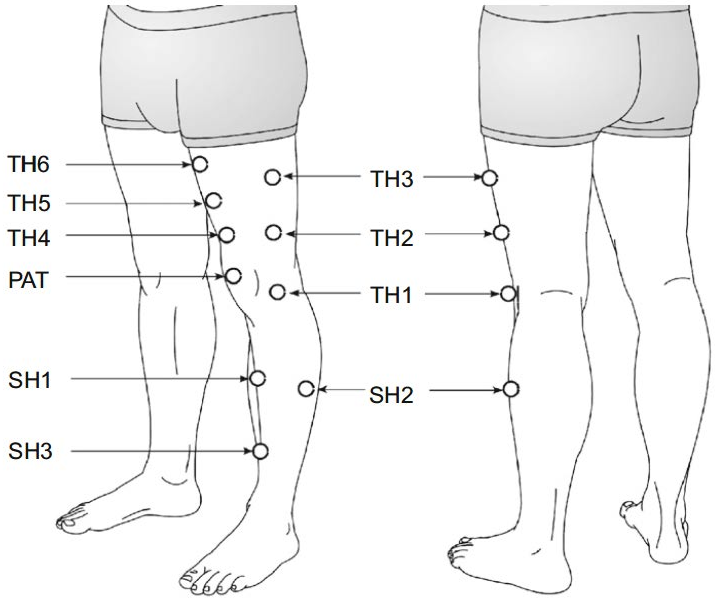

Figure 1.3: Schematic diagram showing the location of ten skin markers; TH1-TH6: thigh markers; SH1-SH3: shank markers; and PAT: patellar marker. Figure extracted from [26].

Other attempts based on invasive methods such as the use of intracortical and percutaneous pins, see Figure 1.4, have been shown important improvements in reducing the STA [27], unfortunately these devices can restrict the movements of the subject, and should also be avoided for ethical reasons.

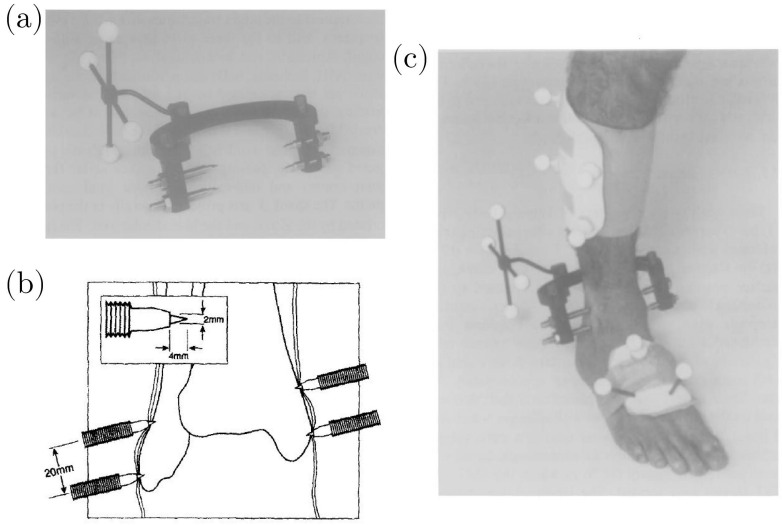

Figure 1.4: (a) Photograph of the percutaneous skeletal tracker (PST), (b) Diagram of the pin insertion through the skin and (c) Photograph of a subject standing with the PST device attached to his distal shank. Figure extracted from [27].

Most recently, mathematical optimization techniques via segmental or global approaches have appeared as mentioned above. The segmental approach works considering a single segment separately addressing marker cluster deformation and its displacement independently from other body segments. Least-squares algorithms [28], singular value decomposition (SVD) [29] and the so-called solidification [30] procedures were proposed to reduce STA on analytical bases and are some examples of the segmental optimization approach. Leardini et al. in [22] concluded that skin marker optimization, based on isolate segments, which can only minimize non-rigid motion components, is superfluos, and that procedures designed to account for cluster rigid translation and orientation are required to correctly represent body segments motion. The real foremost alternative is the MKO approach, which entails searching solutions for the best possible segment pose estimation by considering an entire multibody model, namely a kinematic chain made of rigid segments connected by articulating joints. In other words, the overall configuration of the limb model must be searched to minimize the distances between the model-determined and the measured marker trajectories.

The MKO approach, seemed to have great potential, as the overall kinematic estimation can take advantage of the joint constraints. On the other hand, from the beginning it was clear that the quality of the final results would have been strictly correlated with the general quality of the joint models. The first proposal of this type dates back to 1999 [31], although it addressed the three-dimensional problem of lower limb motion analysis only in analytical terms.

Recently new investigations were carried out from both the joint constraint and the algorithm efficiency point of view, and in the past few years, the effect of different models and constraints at the lower limb joints level have been assessed thoroughly [32–34] as well as the sensitivity to relevant parameters [35–37]. The most comprenhensive study developed by Duprey et al. [33] tested the performances of a number of different sets of models of the lower limb joints, and assessed their influence in the overall kinematics. The introduction of joint models, either by kinematic or anatomical constraints, showed the potential for considerable STA compensation.

1.2 Reporting kinematic data of the knee motion

Human motion analysis using photogrammetric systems and rigid body modeling requires the definition of coordinate systems associated with each bony segment incorporated in the model for the reliability of the kinematic data and its posterior analysis. Since 1990, the Standardization and Terminology Comittee of the International Society of Biomechanics has been working towards a recommendation for standardization in the reporting of kinematic data. It is not intented to restrict individual investigators in the manner in wich they collect or process their data. Rather, it could be viewed as an “output” filter applied to a variety of data formats to provide uniformity in the final product.

The first attempts of the ISB (International Society of Biomechanics) recommendations for standardization in the reporting of kinematic data were published by Wu and Cavanagh in 1995 [16], in which they report basic statements such as; (a) the need of a consistent global reference frame based on a right-handed orthogonal triad with one of its axis towards

and parallel with the field of gravity, (b) a coherent frame to describe segment pose with respect to the global frame which implies a series of right-handed orthogonal triads fixed at the segmental centers of mass, (c) specification of displacement of a segment with respect to the global reference frame, (d) specification of orientation of a segment with respect to the global reference frame, (e) a frame (or system) to express the relative orientation of the body segments with respect to each other and allows rotation about axes which can be anatomically meaningful on the effort to establish a reference frame with non-orthogonal axes. These statements are based on the joint coordinate system, first proposed by Grood and Suntay [38] for the knee joint in 1983 that has the advantage of reporting joint motions in clinically relevant terms. Time latter, Wu et al [17] published a series of papers with the purpose of present joint coordinate system recommendations and definitions that had been tested-used and subsequently revised.

Most recently, Cappozo et al. [15] presented a review of the human movement analysis and the reporting of the kinematic data according to the updated general recommentadions from the ISB such as:

Motor task frame: in human motion analysis orthogonal coordinate systems should have the X-axis pointing forward in most locomotor task coinciding with the direction of progression, Y-axis in the direction of the field of gravity, and Z-axis pointing to the right.

Marker cluster technical frame: this is the frame used to describe the movement of a segment and is reconstructed using the instantaneous position of at least three non-aligned superficial markers associated with the bony segment as is shown in Figure 1.5. These points must coincide with anatomical landmarks so that they be identifiable in repeatable fashion.

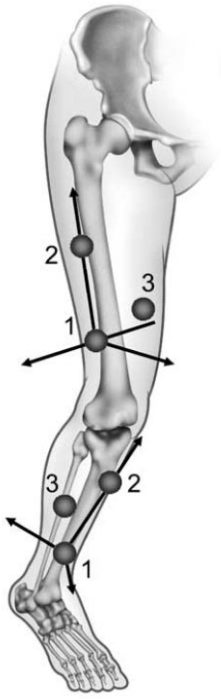

Figure 1.5: Three markers for each bony segment and their corresponding technical frames. Figure extracted from [15].

Joint kinematics: Joint kinematics is the description of the relative movement between two contiguous bony segment, the proximal (p) an the distal (d). Let us define $\mathbf{R}_j$ as the joint orientation matrix and $\boldsymbol{t}_j$ as the joint position vector, carry complete information about orientation and position (pose) of the distal segment relative to the proximal segment, see Figure 1.6. $\mathbf{R}_j$, by its own nature, describes the joint orientation, taking as reference the orientation when the two local frames involved are aligned ($\mathbf{R}_j = \mathbf{I}$; where $\mathbf{I}$ is the identity matrix). A possible alternative for the identification of appropriate proximal and distal anatomic frames is making reference to the so-called joint axes.

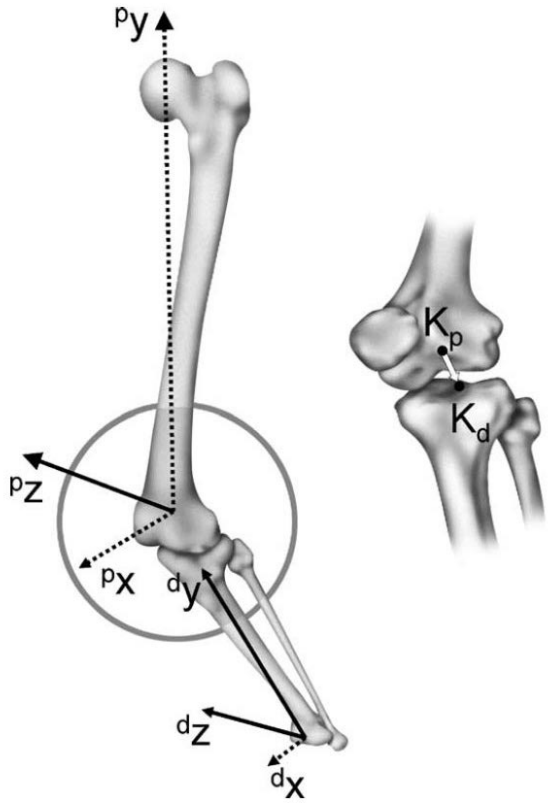

Figure 1.6: Proximal and distal anatomical frames used to describe joint kinematics. The points defined in the proximal (K_p) and in the distal frames (K_d) used to describe the joint translational degrees of freedom are also indicated. Figure extracted from [15].

With respect to the interpretability and consistency with the language of functional anatomy, it is desirable that the six independent scalar quantities inherent in $\mathbf{R}_j$ and $\boldsymbol{t}_j$ be three angles (three rotational degrees of freedom) and three lengths (three translational degrees of freedom) defined relative to the given axes. Mechanics provides several methods that allow the extraction of the latter quantities from the joint orientation matrix and position vector.

Translational degrees of freedom: the relative position between two adjacent bones is described by making reference to the vector ($\boldsymbol{t}_j^*$) joining a point defined in each of the proximal (K_p) and the distal local frames (K_d), see Figure 1.6. This is an issue that has not been sufficiently debated. The reason for this may be that the variations in magnitude of this vector during movement are normally too small.

Rotational degrees of freedom: assuming that, to start with, the two anatomical frames axes aligned, the distal anatomical frame can reach any orientation relative to the proximal frame by undergoing three successive rotations, each time about one of the three axes involved. The three angles thus obtained are used to describe the joint instantaneous orientation. If the anatomical frames are chosen so that the x axes are antero-posterior, the y axes are longitudinal, and the z axes are medio-lateral relative to the bony segments involved (Figure 1.6), then their corresponding angles may be effectively interpreted as the extent to which the joint is abducted or adducted, internally or externally rotated, and flexed or extended, respectively, relative to the reference aligned orientation.

A third approach may be proposed for the description of joint's rotational degrees of freedom. It is based on the projection of axes of an anatomical frame onto the planes of the other anatomical frame. In the instance of the knee joint, the following rotation angles can be defined:

- Flexion-extension angle: the angle formed by the y axis of the tibia and the projection of the y axis of the femur onto the xy plane of the tibia.
- Abduction-adduction: the angle formed by the y axis of the tibia and the projection of the y axis of the femur onto the yz plane of the tibia.
- Internal-external rotation angle: the angle formed by the x axis of the tibia and the projection of the x axis of the femur onto the xz plane of the tibia.

The reproducibility of the anatomical frames is a systematic process but it is highly dependant on the ability of the clinician to identify bony prominences by palpation, making the measuring process of the body segmental movements difficult for non-experts researchers without physiotherapy training.

1.2.1 Geometrical parameters of the knee joint

The knee center and rotation axes (joint parameters) are central to all branches of motion analysis and are fundamental elements of clinical motion analysis. In gait analysis, the standard protocol used to determine the knee joint parameters is prone to errors arising from palpation, anthropometric regression equations, and misplaced alignment devices. Several alternatives to these standard methods have been described in [39, 40]. Others determined these joint parameters making *in vitro* experiments e.g. Markolf et al [41], who determined the location of Flexion-Extension Axis (FEA) relative to the Transepicondular axis (TEA) located within the posterior femoral condyles defined by the most prominent point on the lateral epicondyle and directed to a location on the medial epicondyle, see Figure 1.7.

In 2005, Schwartz and Rozumalski proposed a new method for estimating joint parameters from motion data [42], which can be summarized as follows: (i) the motion of two adjacent segments spanning a single joint are tracked, (ii) the axis of rotation between every pair of observed segment configurations is computed, (iii) the most likely all axes intersection (effective joint center) and most likely axes orientation (effective joint axis) is found. This method was designed to produce precise and objective joint parameters

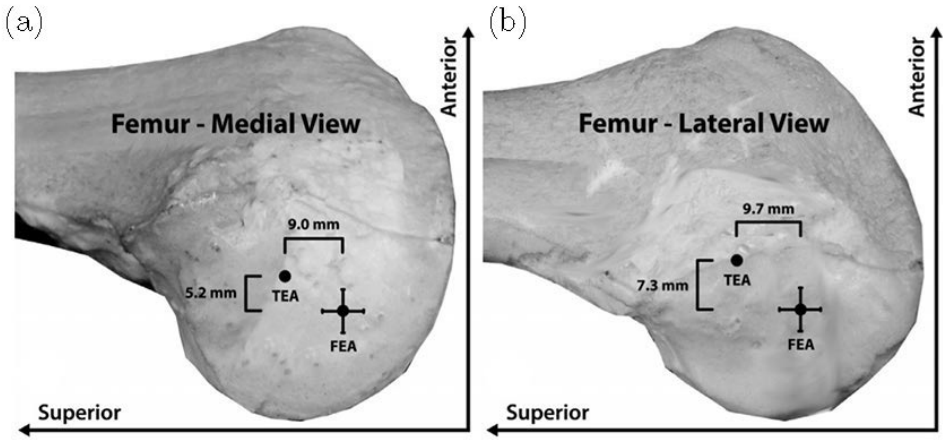

Figure 1.7: The mean location of the FEA with respect to the TEA on (a) the medial femoral condyle and (b) the lateral femoral condyle.

across trials and observers, and to be independent to marker placement. The present work is mainly based on this method for the joint parameters determination and the knee work-space (WS).

1.3 Review: kinematic knee models

Kinematic models are among powerful tools for the functional analysis of such a complicated biological structures, and represent helpful tools for the solution of important issues such as:

- definition of surgical and diagnostic procedures for joint conditions caused by injuries or diseases;
- design prosthesis devices [43, 44];
- assessment of the role of the joint biological structures in the joint characteristics in normal and pathological conditions [45].

Planar and spatial kinematic models of joints have been presented in the literature. Planar models proved to be of great usefulness. However, for many joints they cannot take into account some complicated and subtle phenomena involved in the joint motion since most of them have intrinsically three-dimensional motion.

Parenti-Castelli and Sancisi [46] clasified the models presented in the literature into two different approaches. The first one, models the biological structures of the joint connections such as ligaments, muscles, and articular surfaces by means of linear and non-linear elastic and dumping elements. The main bones are allowed to have up to six degrees of freedom (DoF) in their relative motion which finally depends on the external forces applied to the joint and on the elastic and dumping characteristics of the joint connecting structures. These models are computationally demanding but are also suitable to simulate the dynamic behaviour of the joint.

On the other hand, the second approach, models the joint as a linkage or an equivalent mechanism whose geometry is based, as much as possible, on the joint anatomical structures. These mechanisms are suitable to analyze the passive motion of the joint, that is, the motion of the joint under virtually unloaded conditions.

Parenti-Castelli et al. [47], also presented, a sequential approach for the kinematic, kinetostatic and dynamic modeling of diarthrodial joints. The approach relies upon some basic hypotheses and is based on three main steps from which, in order, three joint models of increasing complexity can be obtained. More precisely, the first step models the joint passive motion, the second step takes into account the kinetostatic behaviour of the joint under external loads, and the third step considers the dynamic influence of the active elements such as the muscles.

The present review focuses on the second approach for the kinematic models of the knee joint which along with the ankle are the mainly modeled joints.

One of the principal uses of the kinematic knee models is for MKO in gait analysis, which entails searching solutions for the best possible segment pose estimation by considering an entire lower limb multibody model, namely a kinematics chain made of rigid segments connected by articulating joints.

Anatomical significance is an important part of a kinematic model to ensure a close correlation with the real knee. In general, it is expected that most of the pathological conditions, are difficult to be replicated in joint models, particularly in case of simple non-anatomical joint constraints, [22].

It is expected that the more the joint model is anatomically realistic, the more accurate the final bone pose estimation will be. However, this higher accuracy would require more careful identification of the joint model parameters and therefore higher computational time.

The use of simple constraints imposed by lower pairs in the MKO was validated in Stagni et al. [18]. The study compared joint angles obtained at the knee during walking trials using two types of constraints spherical, revolute (S and R) and no constraints. The error of the pair R was the highest and authors suggested that no benefits are obtained for STA reduction if simplistic joint models are used.

1.3.1 The historical development of the kinematic knee models

The first attempts for modeling the human knee joint were planar models as 2-Dimensional four-bar mechanisms, as the O'Connor model [1] in which the two cruciate ligaments are the two links that guide the bone links (tibia and femur), shown in Figure 1.8. Some other examples of planar knee models are given in [48–51]. All modeling the knee motion in the sagittal plane.

Parallel mechanisms which are basically a generalization in the 3D space of previous planar mechanisms became of great interest since they allow: (i) high anatomical significance, (ii) model personalization on the specific patient, (iii) the capability to include ligament stiffness [52] for further kinetostatic and dynamic analysis and (iv) a better compensation of STA demonstrated in the study developed by Duprey et al. [33]. These authors also concluded that only parallel mechanisms can reproduce the known rollback at the knee and rolling at the ankle.

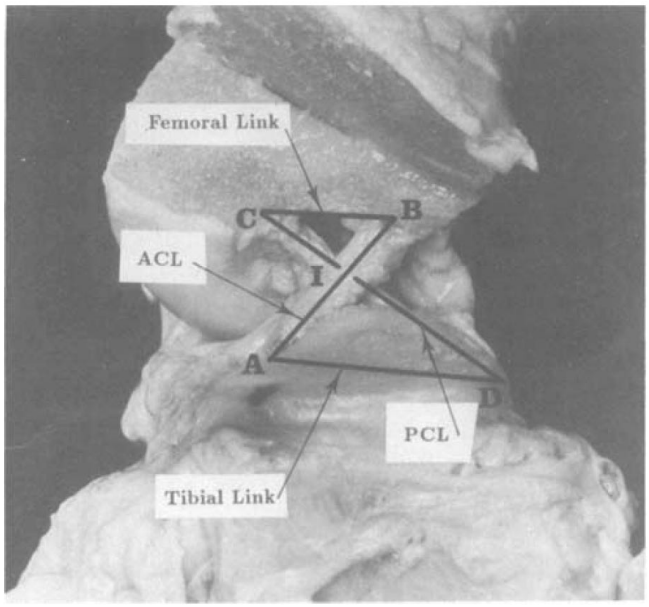

Figure 1.8: Knee model based on a planar four-bar mechanism proposed by O'Connor [1].

Most of the spatial parallel mechanisms (SPM) that model the knee joint are one-DoF mechanisms. This consideration is based on several studies [2, 44] which prove that the motion of the tibio-femoral joint during passive flexion is one DoF motion. The models feature a one-to-one representation of the joint anatomical constraints. These constraints are the articular surfaces and the assumption of isometric fibres of three ligaments, namely the cruciates, ACL and PCL, and the medial collateral ligament, MCL.

One of the first SPM (with one DoF) for the study of the knee passive motion was presented by Wilson and O'Connor [2] as a 3-US and two spheres on planes, parallel mechanism shown in Figure 1.9. This model combined a relative simplicity with the ability to take the tibia-femur spatial motion into account.

A few year later, Di Gregorio and Parenti-Castelli [3, 53, 54] proposed several SPM's as improvements of the Wilson and O'Connor SPM [2]. An example of these [3] is shown in Fgure 1.10. This proposal models both the femur and tibia as two ellipsoids on spheres and the isometric fibres of the ligaments as 3-US links into a complete SPM.

More recently, SPM were also proposed to model the whole knee joint, including the patella [4, 5]. These models are still a generalization of the first proposal by Wilson and O'Connor [2] with simplifications at the bone contacts and again assuming isometry in the ligaments. The proposal by Sancisi and Parenti-Castelli [4] shown in Figure 1.11, models the knee as a 5-SS+SSRSPS parallel mechanism for the tibio-femoral and the patello-femoral joints respectively. This mechanism allows good subject-specific optimization by changing the positions of the attachments of the five SS links within the parallel platforms, but loss anatomical significance specially in the modelling of the articular surfaces and bone contacts.

After that, Sancisi and Parenti-Castelli proposed a new model as a S, 2-SS+SSRSPS spherical parallel platform for the tibio-femoral and the patello-femoral joints respectively [5]. This model is less accurate than their previously presented model but provides a more

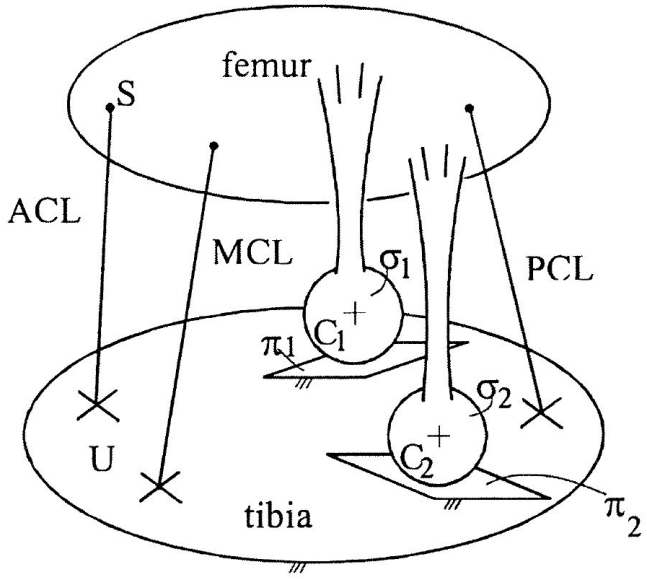

Figure 1.9: Knee model parallel mechanism proposed by Wilson and O'Connor [2].

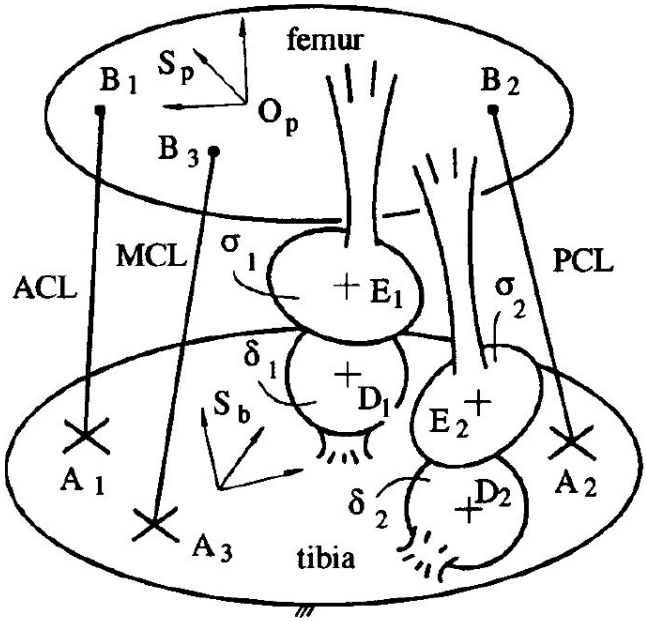

Figure 1.10: Knee model parallel mechanism proposed by Di Gregorio and Parenti-Castelli [3].

suitable tool for the design of knee prostheses. This new model is shown in Figure 1.12.

The geometric and kinematic observations that support these mechanisms are all similar. Experimental studies show that a bundle of fibres of the anterior cruciate (ACL), one of the posterior cruciate (PCL) an another one of the medial collateral (MCL) ligaments remain almost isometric during passive flexion. As a consequence, three isometric fibres and the two pairs of condyles are the anatomical structures which guide and affect the passive motion of the tibio-femoral joint [55].

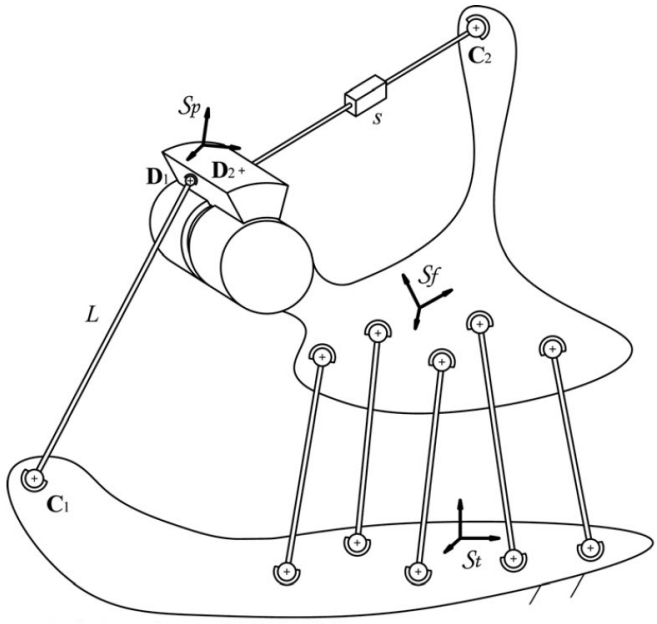

Figure 1.11: Knee model parallel mechanism proposed by Sancisi and Parenti-Castelli [4].

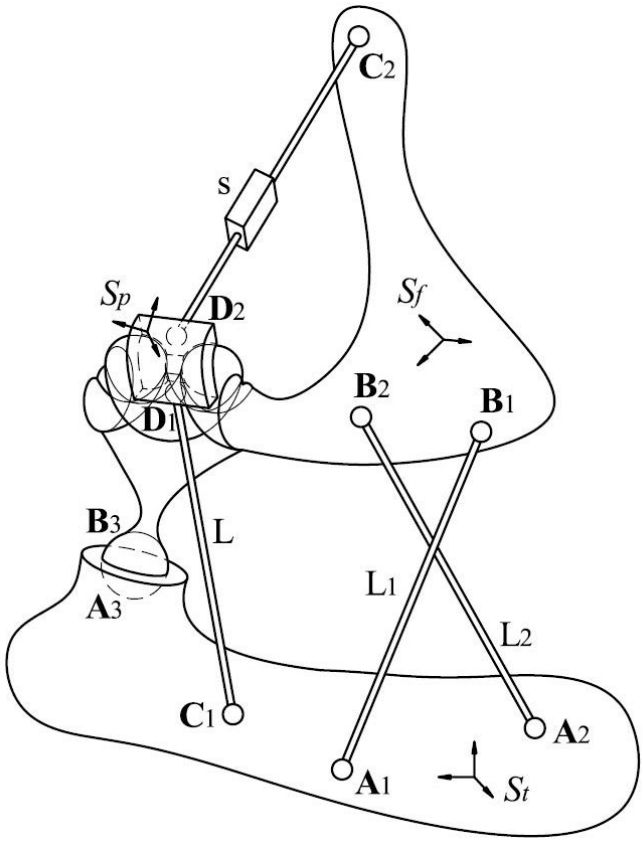

Figure 1.12: Knee model spherical parallel mechanism proposed by Sancisi and Parenti-Castelli [5].

Further insights in the modelling of knee mechanisms include deformable ligaments, ΔL. As a result, the SPM can be clasified into three categories [22]: (ΔL_0) [56], prescribed (ΔL_θ) [57] and minimized (ΔL_{min}) [58] ligament length variations. These SPM with deformable ligaments have taken importancy since the one-DoF models have large discrepancies to model the knee movement, in particular, for internal-external rotation and full flexion-extension.

Table 1.1. is presented as a summary of the principal proposed kinematic SPM. The table describes; the author, architecture of the tibio-femoral (TF) and patello-femoral (PF) joints, year, DoF, anatomical structures included and whether or not the model takes into account the deformability of the ligaments.

Table 1.1: Review: Spatial parallel mechanisms to modelling the knee joint. Non-Linear (NL).

Author	**Architecture TF / PF**	**Year**	**DoF**	**Anatomical structures**	**Deformable ligaments**
Wilson and O'Connor [2]	3-US, 2-Sphere on Plane / -	1997	1	Condyles, ACL, PCL and MCL	No
Parenti-Castelli and Di Gregorio [53].	3-US, 2-Sphere on Sphere / -	2000	1	Condyles, ACL, PCL and MCL	No
Di Gregorio and Parenti-Castelli [3].	3-US, 2-Ellipsoid on sphere / -	2003	1	Condyles, ACL, PCL and MCL	No
Parenti-Castelli et al. [54]	3-SS, 2-Surface on Surface / -	2004	1	Condyles, ACL, PCL and MCL	No
Ottoboni et al. [56]	3-SS, 2-Sphere on Surface / -	2010	1	Condyles, ACL, PCL and MCL	No
Sancisi and Parenti-Castelli [59]	5-SS / -	2007	1	Condyles, ACL, PCL and MCL	No
Sancisi and Parenti-Castelli [60]	S, 2-SS / -	2010	1	Condyles, ACL and PCL	No
Sancisi and Parenti-Castelli [4]	5-SS / SSRSPS	2011	1	Condyles, ACL, PCL, MCL and Patella	No
Sancisi and Parenti-Castelli [5]	S, 2-SS / SSRSPS	2011	1	Condyles, ACL, PCL and Patella	No
Bergamini et al. [57]	4-Springs /	2011	-	ACL, PCL, MCL and LCL	Yes
Gasparutto et al. [58]	2-Sphere on Plane, 4-NL-Springs /	2012	-	Condyles, ACL, PCL, MCL and LCL	Yes
Sintini et al. [61]	2-Sphere on Sphere, 4-NL-Springs/	2018	-	Condyles, ACL, PCL, MCL and LCL	Yes

Of course many other knee models can be found in the literature, in particular finite element and deformable multibody models [52, 62–65]. However, these find noteworthy applications in musculo-skeletal modeling with much more expensive computational resources to model only the knee kinematic motion analysis, and fall outside the scopes of the present review.

1.3.2 Conclusions

All kinematic mechanisms reported in the literature coerce one DoF and isometric fibres of the ACL, PCL and MCL ligaments, causing the mechanism to only work correctly during total passive motion. This is an important disadvantage spetially for MKO during gait analysis, since the gait is a completely active motion task of the knee, and the lower limb in general.

Another important disadvantage of the reported kinematic knee models induced by the one DoF constraint, is the complex task of subject-specific optimization of the mechanism. As we can see in the historical development of the kinematic knee models, the authors made great simplifications in the bone contacts in order to make it possible the subject-specific task. This simplifications yield to an important loss in anatomical significance.

Moreover, none of the complete kinematic mechanism take into account the LCL ligament as part of the model.

When deformable ligaments were introduced into the model, the analysis was no longer pure kinematic instead it was computational, making the analysis too expensive for only motion analysis, e. g. MKO during gait analisys.

A kinematic knee model with more than one DoF could deals with these problems remaining high anatomical significance, allowing modeling the deformability of the ligaments by means of only kinematic constraints and facilitating the subject specific optimization.

1.4 Objectives of the research work

The present thesis project has two general objectives corresponding to the topics addressed: **a) Determination of the geometrical parameters of the knee** and **b) nSynthesis of a kinematic knee model**.

1.4.1 General objectives

Develop a new easy to implement methodology using kinematic and mathematic tools, insensitive to marker placement based in photogrammetric techniques to obtain the knee work-space and to identify its joint parameters. In general search for the spatial motion of the healthy knee joint during passive and semi-active motion tasks.

Moreover, the synthesis of a new completely kinematic knee model with high anatomical significance and more than one DoF capable of reproducing the knee experimental work-space with great precision and at same time, model the movements of the internal structures of the knee such as the ligament length variations.

1.4.2 Especific objectives

- The use of an easy and cheap photogrammetric technique as a measuring instrument.
- Determine the knee work-space for each motion task.
- Obtain best fit spatial geometries to compute some geometrical parameters of the knee joint during a motion task.

- Harness to the kinematic concept of the screw line to search the variation of the main axis of the knee joint.
- Propose a new kinematic knee model as a spatial parallel mechanism with anatomical significance.
- Prove that the proposed mechanism is capable to reproduce the experimental WS.
- Include the four principal ligaments of the knee in the complete kinematic knee model.
- Perform a subject-specific optimization process to adjust the ligament length variations of the knee model to a prescribed ones.

Chapter 2

Knee joint fundamentals: anatomy and physiology

In this chapter, the anatomy and the physiology fundamentals of the knee joint is described, by means of the knee movements and the main passive elements of the knee, these are: bones, ligaments, menisci and the patellar tendon. The chapter begins with the knee anatomy introducing important terms for subsequent references in the knee physiology section. After this, the fundamentals of the knee physiology are presented mainly based the role of the passive elements during the knee motion.

Understanding the fundamentals of the knee anatomy and physiology is important to know the expected results and for the choice of the motion tasks that will be performed to obtain relevant results. Moreover, the role of the passive elements of the knee should be the basis for the synthesis of the kinematic knee model with anatomical significance.

2.1 Knee anatomy

This section deals with the passive elements anatomy of the knee, knowledge necessary to understand the physiology.

In the Figure 2.1, the passive elements of the knee are shown at a scheme taken from the Atlas of Human Anatomy ilustrated by Netter [66].

2.2 The axes of the knee joint

The first axis XX', Figure 2.2, is around which occur movements of flexion-extension in a sagittal plane. This axis passes horizontally through the femoral condyles.

The second rotation axis YY', Figure 2.2, is clearly defined with the knee flexed. The structure of the knee makes axial internal-external rotation impossible when the knee is fully extended: the axis of the thigh then coincides with the mechanical axis of the shank and axial rotation takes place not at the knee but at the hip joint.

In Figure 2.2 an axis ZZ' is shown running anteroposteriorly at right angle to the other two axes. This axis does not really represent a degree of freedom but, because of a measure of play in the joint due to relaxation of the collateral ligaments, it allows the accurrence

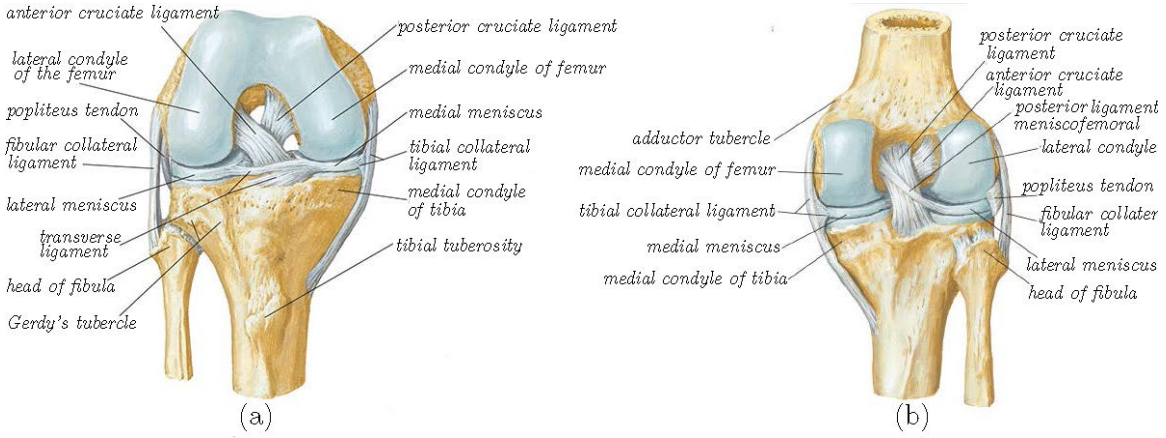

Figure 2.1: Anatomy of the knee joint (passive elements); (a) right knee during flexion: anterior view and (b) right knee during extension: posterior view. Fig. extracted from [66]

.

of small abduction-adduction movements of about 1-2 *cm* observed at the ankle; when the knee is fully extended, these movements disappear completely. If they still persist, they must be viewed as abnormal, i.e. an indication of collateral ligament injury.

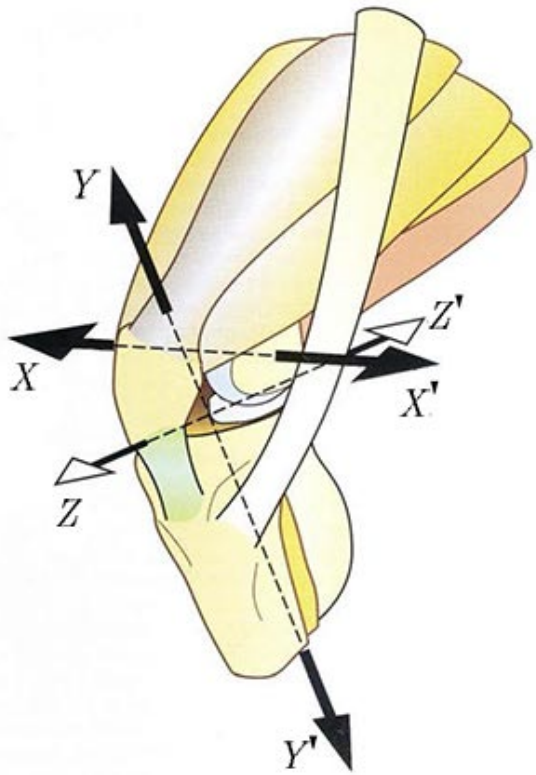

Figure 2.2: Main axes of the knee joint during semi-flexed position. Fig. extracted from [67].

2.3 Principal knee movements

The principal knee rotations (flexion-extension and internal-external) and their ranges of movement are described in this section.

2.3.1 Flexion-extension rotation

Flexion-extension is, by far, the main movement of the knee. Its range is measured from the reference position defined by the following criterion: the collinearly of the long axis of the thigh with that of the shank.

Extension is defined as the movement of the posterior surface of the shank away from the posterior surface of the thigh.

Flexion is the movement of the posterior surface of shank towards the posterior surface of the thigh. The range of the knee flexion varies according to the position of the hip.

Active flexion reaches 140° if the hip is already flexed, Figure 2.3(a), and only 120° if the hip is extended, Figure 2.3(b). This difference in amplitude is due to the fact that the hamstrings lose some of their efficiency with hip extension. **Passive flexion** of the knee has a range of 160°, Figure 2.3(c), and allows the heel to touch the buttock.

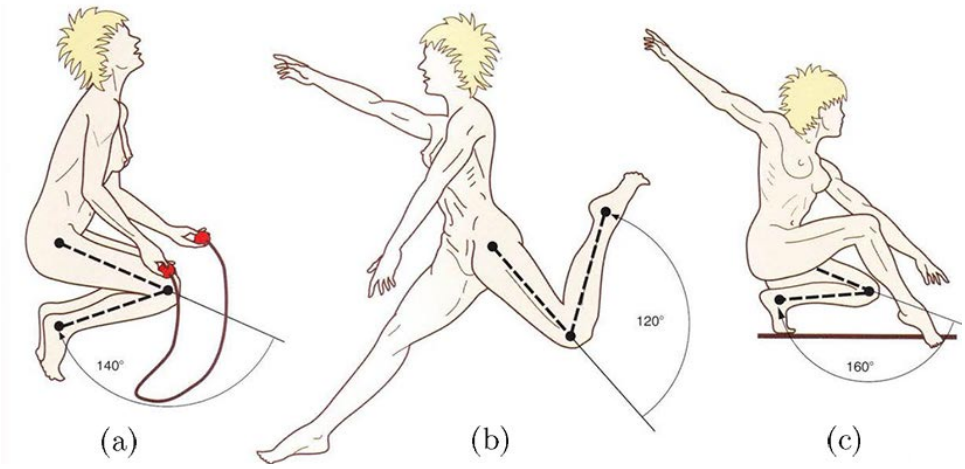

Figure 2.3: Active and passive flexion of the knee; (a) hip flexed, (b) hip extended and (c) passive flexion of the knee. Fig. modified from [67].

2.3.2 Internal-external rotation

The rotation movement of the knee around its long axis can only be performed with the knee flexed, since with the knee in extension and the interlocking of the joint, the tibia becomes one with the femur.

To measure **Active internal-external rotation**, the knee must first be flexed at right angle while the subject is sitting on a table with legs banging down over the edge, Figure 2.4(a). In the reference position the toes face slightly laterally.

Medial rotation, Figure 2.4(b), brings the toes to face medially and contributes significantly to adduction of the foot.

Lateral rotation, Figure 2.4(c), brings the toes to face laterally and also contributes to the abduction of the foot.

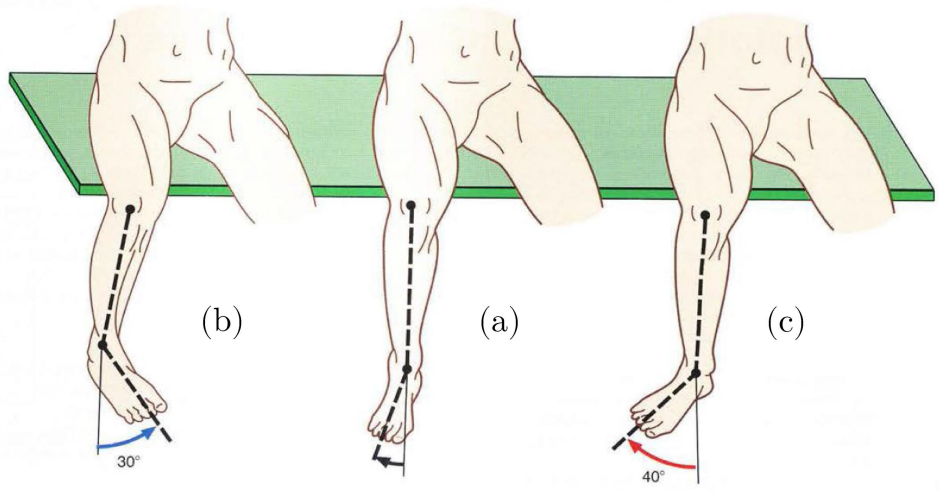

Figure 2.4: Active internal-external rotation of the knee; (a) reference position, (b) medial rotation and (c) lateral rotation. Fig. modified from [67].

Acoording to Fick [68] the range of lateral rotation is 40° and that of medial rotation 30°, and the range varies with the degree of knee flexion, since, according with the same author, it is 32° for lateral rotation when the knee is flexed at 30° and 40° when the knee is flexed at 90°. All of these angles are measured in the foot.

Passive internal-external rotation is measured with the subject lying prone with the knee flexed at 90°. The examiner grasps the foot with both hands and rotates it until the toes face laterally, Figure 2.5(a), and medially, Figure 2.5(b). As expected, this passive rotation has a greater range than active rotation.

Finally, there is also a type of axial rotation called "automatic" because it is inevitably and involuntarily linked to movements of flexion-extension. When the knee is extended the foot is laterally rotated. Conversely, when the knee is flexed the foot is medially rotated.

2.4 Femoral condyles and tibial articular surfaces

The articular surface of the distal end of the femur is shaped like a pulley. The **two femoral condyles**, convex in both planes, form the two cheeks of the pulley, Figure 2.6(a), with the two cheeks of the femoral pulley-shaped patellar surface or the trochlea. The neck of the pulley corresponds anteriorly to the central groove of the trochlea and posteriorly to the intercondylar fossa. The **tibial superior articular surfaces**, reciprocally modelled on those of the femur, consist of two curved; concave and convex parallel gutters separated by the blunt intercondylar eminence, Figure 2.6(b). As a result, the medial femoral condyle is relatively stable, while the lateral condyle is unstable, so that its stability during motion is essentially dependent on the intactness of the anterior cruciate ligament.

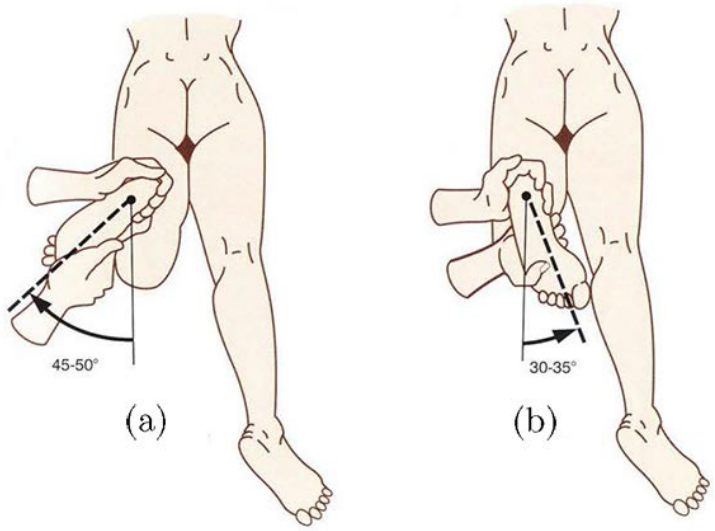

Figure 2.5: Passive internal-external rotation of the knee; (a) lateral rotation and (b) medial rotation. Fig. modified from [67].

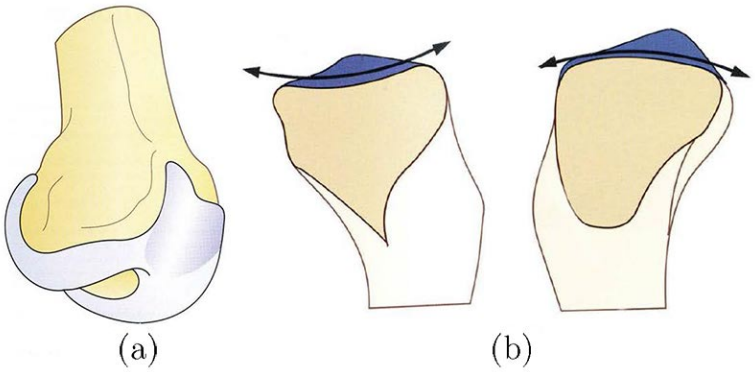

Figure 2.6: Articular surfaces of the tibiofemoral joint; (a) femoral condyles and (b) tibial articular surfaces. Fig. modified from [67].

Thus the tibial articular surfaces correspond to those of the femoral condyles, while the tibial intercondylar tubercles lodge inside the femoral intercondylar fossa; this aggregate of articular surfaces functionally constitutes the **tibiofemoral joint**. Anteriorly, the two facets of the patellar articular surface correspond to the cheeks of the femoral trochlea, and the patellar vertical ridge fits into the intercondylar fossa. These surfaces make up the second functional joint, the **femoropatellar joint**. These two joints are separated but are contained within a single anatomical joint, i.e. the **knee joint**.

2.4.1 Movements during flexion-extension rotation

The rounded shape of the condyles could suggest wrongly that they roll over the tibial plateau. If the condyle only rolled, Figure 2.7(a), after certain degree of flexion (position II), it would topple over behind the tibial plateau, which is equivalent to dislocation of the joint. The possibility of a pure rolling movement of the condyle is thus precluded by

the fact that the full length of its circumference is twice that of the tibial surface.

If such a pure sliding movement of the condyles on the tibial plateau were to occur, Figure 2.7(b), a single point on the tibial plateau would correspond to all the points on the condylar surface, but this occurrence would check flexion prematurely because of the impact of the condyle on the posterior margin of the tibial plateau (arrow).

In 1836 the Werber brothers [69] proved indisputably that the femoral condyle rolls and slides simultaneously over the tibial plateau, Figure 2.7(c). This is after all, the only way that posterior dislocation of the condyle can be avoided while permitting a greater range of flexion.

Following this, experiments (Strasser [70]) showed that the rolling to sliding ratio varies during the entire movement of flexion-extension. Starting from full extension **the condyle begins to roll without sliding**, and then sliding becomes progressively greater, so that **at the end of flexion the condyle slides without rolling**. Finally, the length over which pure rolling takes place varies with the condyle:

- for the medial condyle rolling occurs only during the first $10-15^{\circ}$ degrees of flexion,
- for the lateral condyle rolling continues up to 20° flexion.

Therefore, the lateral condyle rolls far more than the medial condyle. This important observation explains the automatic rotation of the knee during flexion-extension.

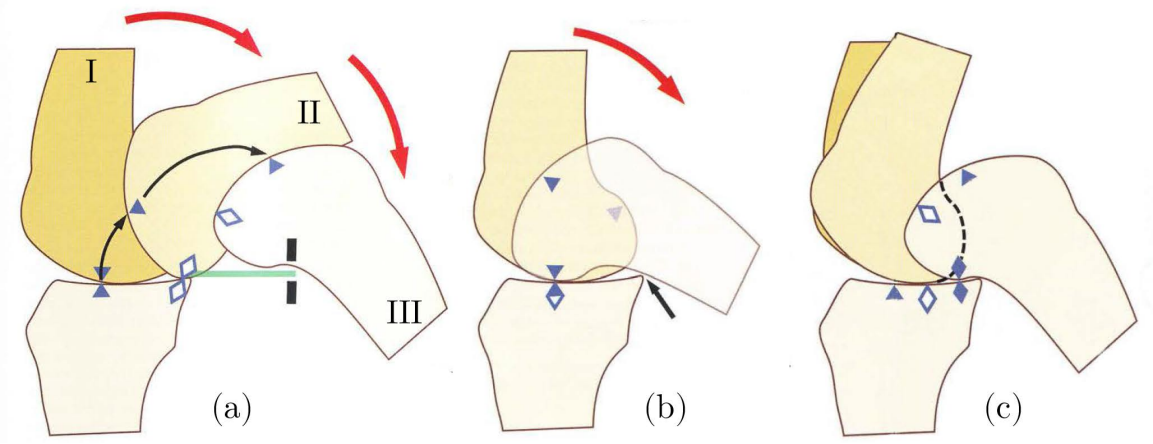

Figure 2.7: Movement of the femoral condyles on the tibial plateau during flexion; (a) pure rolling, (b) pure sliding (c) rolling and sliding. Fig. modified from [67].

2.4.2 Movements during internal-external rotation

Internal-external rotation can only take place when the knee is flexed, Figure 2.8(a). With the knee half-flexed, the posterior part of each femoral condyle is in contact with the middle of each tibial articular surface. Moreover, during flexion the tibial intercondylar eminence moves out of the femoral intercondylar fossa, where it is confined during extension. (this is one of the reasons why axial rotation is checked when the knee is extended).

During external rotation of the tibia, Figure 2.8(b), the lateral condyle moves forwards on the lateral tibial surface, while the medial condyle moves backwards on the medial surface.

During internal rotation of the tibia on the femur, Figure 2.8(c), the converse is true: the lateral condyle moves backwards and the medial condyle forwards on their corresponding tibial surfaces.

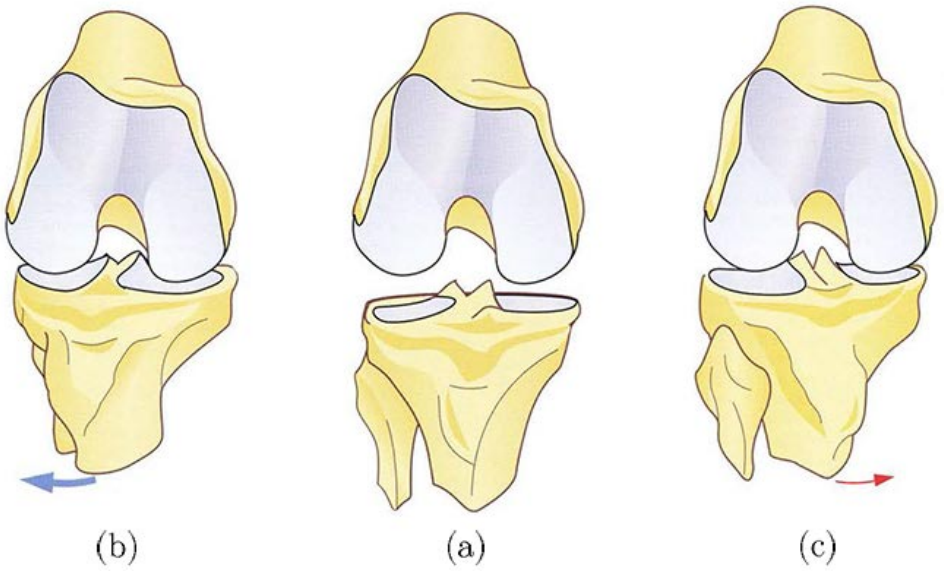

Figure 2.8: Movement of tibia under the femur during axial rotation; (a) neutral position, (b) external rotation (c) internal rotation. Fig. modified from [67].

In reality, the anteroposterior movements of the condyles on their corresponding tibial surfaces are not identical:

- the **medial condyle** moves relatively little inside the biconcave medial tibial articular surface,
- the **lateral condyle**, on the other hand, moves nearly twice as much over the convex lateral tibial surface.

As a result, the real axis of axial rotation runs not between the two interccondylar tubercles but through the articular surface of the medial tubercle, which is the central pivot of the joint.

2.5 The menisci

The radii of curvature of the condylar and of the tibial articular surfaces are not equal, leading to non-congruence of the articular surfaces. The knee is the prototype of non-congruent joints. Congruence is restored by the interposition of menisci or semilunar cartilages.

The menisci appear to have been lifted above the tibial articular surfaces, Figure 2.9(a), with the medial and lateral menisci lying in the same horizontal plane above the medial and lateral tibial articular surfaces, respectively.

The menisci have the shape of two rings, so that the lateral meniscus is almost a complete circle in the shape of an O, whereas the medial meniscus is semilunate in the shape of a C, Figure 2.9(b).

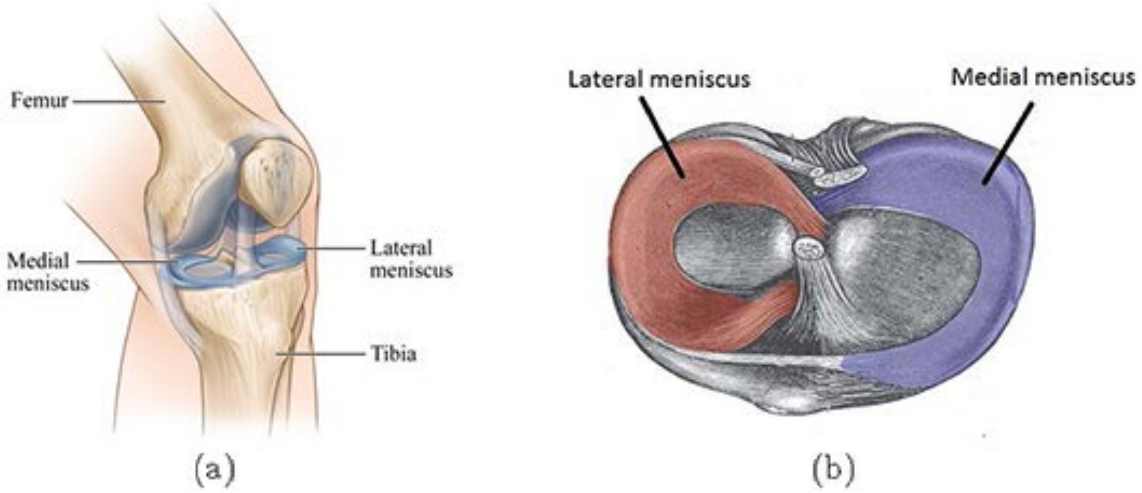

Figure 2.9: The inter-articular menisci; (a) menisci lying on the tibial articular surfaces and (b) menisci shapes. Fig. extracted from [71].

2.5.1 Meniscal displacements during flexion-extension

As shown in the Figure 2.10, the contact point between the femoral and tibial articular surfaces moves posteriorly during flexion and anteriorly during extension. The menisci follow these movements. Moreover the menisci undoubtedly play an important role as elastic couplings for the transmission of compressive forces between femur and tibia.

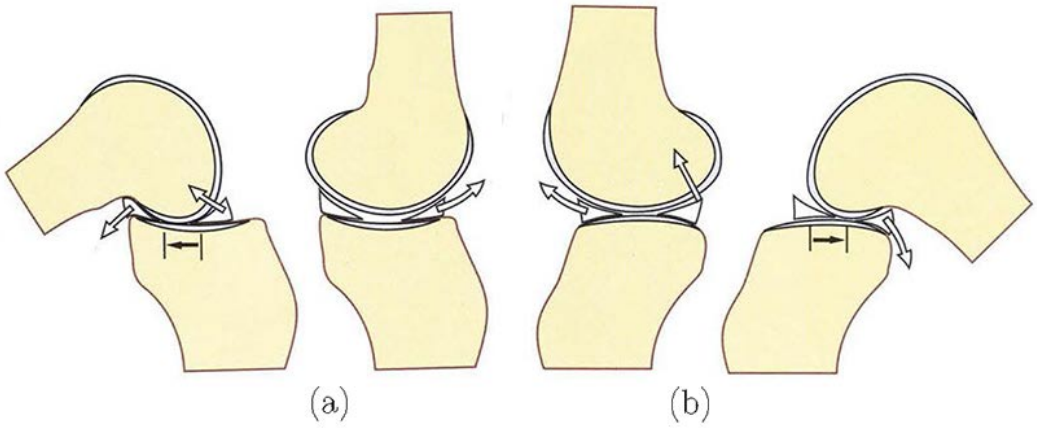

Figure 2.10: Meniscal displacements during flexion-extension; (a) medial view and (b) lateral view. Fig. modified from [67].

2.5.2 Meniscal displacements during internal-external rotation

During movements of internal-external rotation, the menisci follow exactly the movements of the condyles on the tibial plateau, Figure 2.11. In the neutral position of axial rotation, Figure 2.11(a), the lateral meniscus (LM) and the medial meniscus (MM) are well centered on their corresponding tibial articular surfaces. During lateral and medial rotations the menisci can be seen to move in opposite directions to the tibial plateau rotation.

- During external rotation, Figure 2.11(b): the LM is pulled anteriorly, while the MM is pulled posteriorly.
- During internal rotation, Figure 2.11(c): the MM advances, and the LM recedes.

.

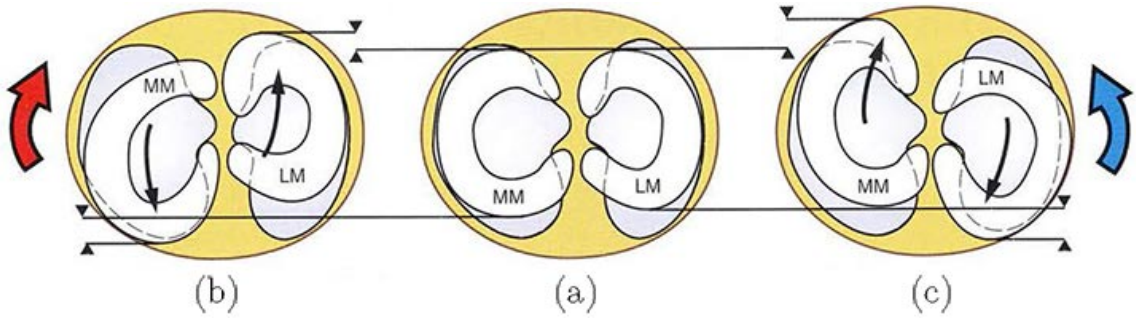

Figure 2.11: Meniscal displacements during internal-external rotation (graphic representation of the right tibial plateau); (a) neutral position, (b) external rotation and (c) internal rotation. Fig. modified from [67].

During knee movements, the menisci can be damaged when fail to follow the condylar movements on the tibial plateau.

2.6 The collateral ligaments of the knee

Knee joint stability depends on two sets of powerful ligaments, i.e. the cruciates and the collateral ligaments. The collateral ligaments reinforce the articular capsule medially and laterally and secure the transverse stability of the joint during extension.

The **medial collateral ligament**, Figure 2.12(a), runs from the subcutaneous aspect of the medial condyle to the upper end of the tibia (MCL). It runs an oblique course inferiorly and anteriorly.

The **lateral collateral ligament**, Figure 2.12(b) stretches from the lateral surface of the lateral condyle to the head of the fibula (LCL). It runs obliquely inferiorly and posteriorly.

Both diagrams of the Figure 2.12 also show the menisco patellar ligaments (1 and 2) and the patellar retinacula (3 and 4), which keep the patella pressed against the femoral trochlea.

The collateral ligaments are stretched during extension and slackened during flexion.

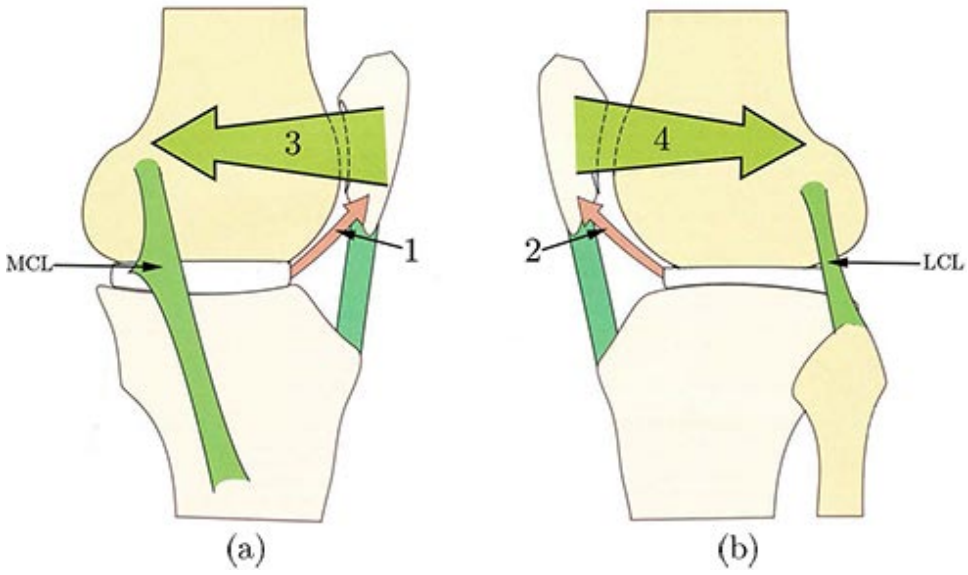

Figure 2.12: Collateral ligaments in a left knee; (a) medial collateral ligament and (b) lateral collateral ligament. Fig. modified from [67].

2.6.1 Transverse stability of the knee: collateral ligaments

A dislocation is normally prevented by the medial ligamentous system.

Traumatic injuries involving the medial and lateral aspects of the knee will cause fractures of the proximal end of the tibia. If the traumatic injury involves the medial aspect of the knee, it tends to straighten the physiological valgus and produces first an avulsion fracture of the medial tibial plateau and then, a rupture of the lateral collateral ligament.

When the traumatic injury involves the lateral aspect of the knee, the lateral femoral condyle is displaced slightly medially and then sinks into the lateral tibial plateau and eventually shatters its lateral cortex.

A severe sprain of the knee impairs the stability of the joint. In fact, when one collateral ligament is torn, the knee cannot resist the transverse stresses to which it is continually subjected.

When violent transverse stresses are applied during running and walking, the collateral ligaments are not the only structures able to stabilize the knee; they are assisted by the muscles. The collateral ligaments are therefore reinforced by thick tendons.

2.6.2 Rotational stability of the extended knee: collateral ligaments

With the knee in full extension, axial rotation is impossible, since it is inhibited by the taut collateral and cruciate ligaments.

The role of the collateral ligaments in securing the rotational stability of the knee can be explained by their symmetry.

In the null rotation, Figure 2.13(a), the obliquity of the lateral and the medial collateral

ligaments cause them to coil round the upper extremity of the tibia.

Internal rotation, Figure 2.13(b) prevents this coiling movement, and the obliquity of these ligaments decreases as they tend to become parallel. Thus, the play permitted by relaxation of the collateral ligaments is offset by the tension of the cruciates.

Conversely, external rotation, 2.13(c) increases the coiling, which brings the articular surfaces closer together and limits their movements while the cruciates are slackened.

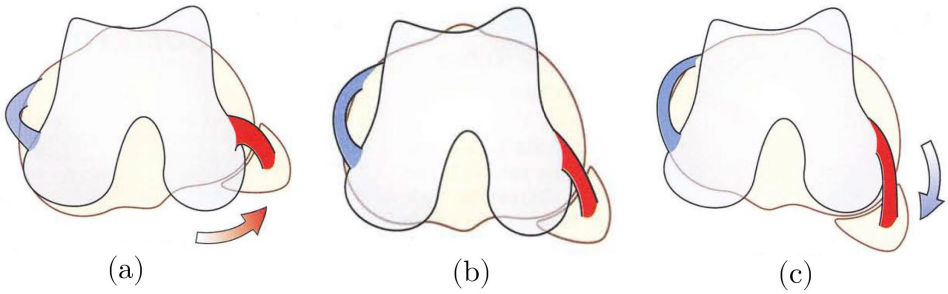

Figure 2.13: Superior view of the collateral ligaments during internal-external rotation of the extended knee; (a) neutral position, (b) medial rotation and (c) lateral rotation. Fig. modified from [67].

2.7 The cruciate ligaments of the knee

With the knee joint open ateriorly, Figure 2.14(a), the first to be seen is the **anterior cruciate ligament** (ACL), see Figure 2.14(b). It turns obliquely and laterally and is attached to the medial aspect of the lateral femoral condyle. It consists of three main bands:

- the anteromedial band: the largest, most superficial and most prone to injury,
- the posteromedial band: which is concealed by the former and remains intact when the ligament is partially torn,
- the intermediate band.

Its fibres are not all of the same length. Acoording to F. Bonnel [72], their mean lengths range from 1.85 to 3.25 *cm*, depending on their location.

The **posterior cruciate ligament** (PCL), see Figure 2.14(b), lies deep in the intercondylar fossa behind the anterior cruciate ligament. The ligament runs obliquely medially anteriorly and superiorly. It comprises three main bands:

- the posterolateral band, inserted at the most posteriorly into the tibia and the most laterally into the femur,
- the anteromedial band, inserted at the most anteriorly into the tibia and the most medially into the femur
- the menisco-femoral ligament, which is attached to the posterior horn of the lateral menisus.

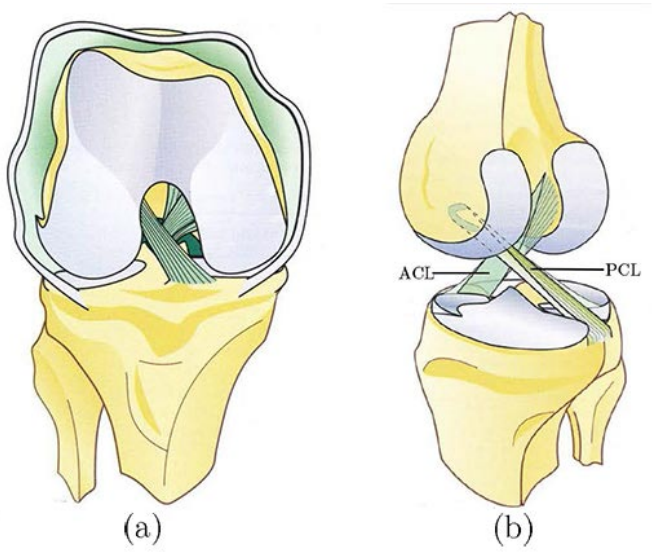

Figure 2.14: Cruciates ligaments of the knee; (a) flexed joint open anteriorly (b) extended joint in postero-lateral view. Fig. modified from [67].

The cruciates are in contact with each other sliding one against the other along their axial margins during knee movements.

The cruciates also have different inclinations: with the knee extended, Figure 2.15(a), the anterior ligament (ACL) is more vertical, while the posterior cruciate (PCL) is more horizontal.

As the knee is flexed, Figure 2.15(b), the posterior cruciate (PCL), which was horizontal in extension, rears itself up to the vertical position and sweeps a 60° angle relative to the tibia, while the anterior cruciate (ACL) is raised only very slightly.

The length ratio of the cruciates shows individual variations, it is typical of each knee.

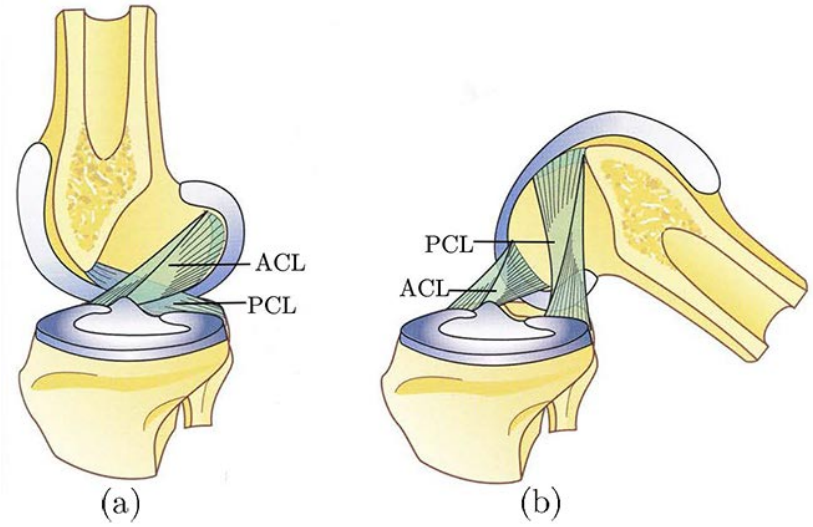

Figure 2.15: Cruciate ligaments of the knee in the sagittal plane; (a) knee extended and (b) knee flexed. Fig. modified from [67].

2.7.1 The mechanical role of the cruciate ligaments

It is customary to reduce the cruciates to linear cords during an analysis of the knee. This approximation has the advantage of revealing the general actions of ligaments but fails to bring out their functional subtleties. To achieve this, three factors need to be taken into account:

1. The thickness of the ligament: the thickness and volume of a ligament are directly proportional to its resistance and inversely proportional to its elasticity.

2. The structure of the ligament: the fibres of a ligament are not all of the same length, with the important consequence that the fibres are not all recruited at the same time, and the resistance and elasticity of the ligament are variable.

3. The size and direction of its insertions: the fibres are not all parallel to one another but are often arranged in planes that are twisted on themselves. Also the relative orientation of the insertions varies during movements, contributing to differential recruitment of the fibres and modifying the overall direction of action of the ligaments.

Globally, the cruciates ensure the anteroposterior stability of the knee and allow hinge-like movements to occur while keeping the articular surfaces in contact.

Different fibres of the cruciates are tensed or slackened during diferent phases of the knee movement. Some of the fibres of the cruciates are always under tension because of their unequal lengths.

Muscles play an active role: the extensors pull the tibia anteriorly under the femur during extension, and conversely the flexors cause the tibial plateau to slide posteriorly during flexion. However, when these movements are studied on a cadaver, passive factors, specially the cruciates, appear to predominate. It is the cruciates that pull back the femoral condyles and cause them to slide on the tibial plateau in a direction apposite to their rolling motion.

During flexion, the anterior cruciate is responsible for the forward sliding of the condyle. During extension, the posterior cruciate is responsible for the backward sliding of the condyle.

2.7.2 Rotational stability of the extended knee

As mentioned before, the cruciate ligaments help the rotational stability of the knee.

When the knee is in the neutral position for axial rotation, Figure 2.16(a), the ligaments clearly cross each other in space. In the horizontal plane, however, the two cruciates are parallel to and in contact with each other.

During internal rotation of the tibia under the femur, Figure 2.16(b), the ligaments are clearly more acutely crossed in the coronal plane, and their inner borders come to touch each other. Quickly check any medial rotation.

During external rotation of the tibia under the femur, Figure 2.16(c), the cruciates tend to become parallel in the coronal plane and their inner borders tend to lose contact. Thus, tightening of the cruciates plays no part in checking lateral rotation.

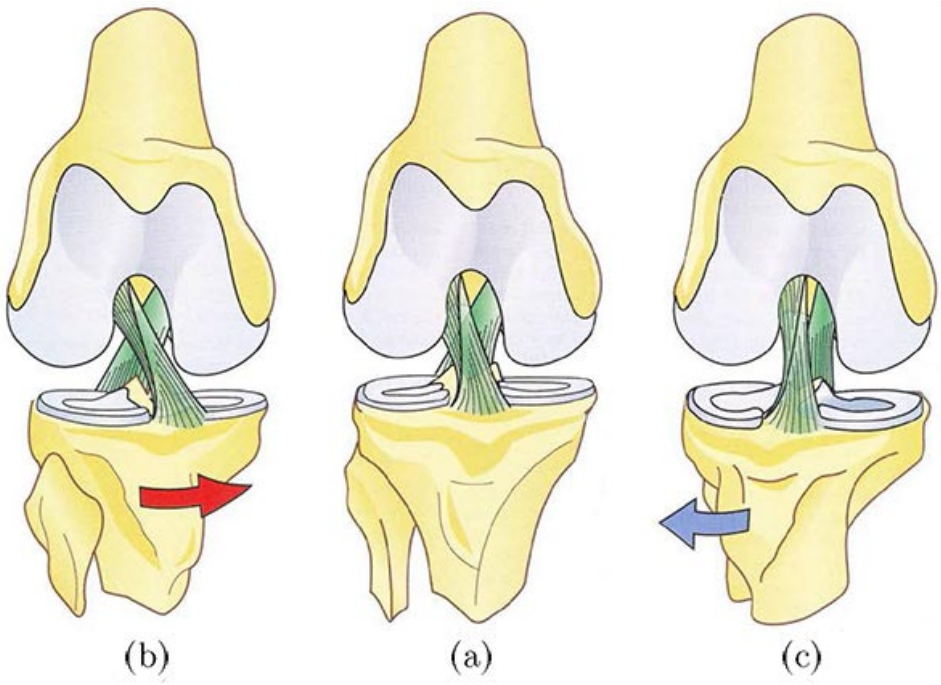

Figure 2.16: Cruciate ligaments during internal-external rotation of the extended knee; (a) neutral position, (b) internal rotation and (c) external rotation. Fig. modified from [67].

Therefore, the rotational stability of the extended knee is ensured by the collateral ligaments during external rotation and by the cruciates during internal rotation.

2.8 Patellar displacement

The extensor apparatus of the knee slides on the distal end of the femur like a cable on a pulley. Thus the force of the quadriceps, directed obliquely superiorly and slightly laterally, is changed into a strictly vertical force.

The normal movement of the patella on the femur during flexion is therefore a vertical translation along the central groove of the femoral trochlea down to the intercondylar fossa as is shown in Figure 2.17. Therefore the patella undergoes a circumferential translation.

There are two types of patellar movements relative to the tibia, one type during flexio-extension and other during internal-external rotation.

During flexion-extension, the patella moves in a sagittal plane, it recedes along the arc of a circle with its centre at the tibial tuberosity and its radius equal to the length of the patellar ligament.

During movements of internal-external rotation, Figure 2.18, the patellar displacements relative to the tibia occur in the coronal plane. In the neutral position of rotation, Figure 2.18(a), the patellar ligament runs a slightly oblique course inferiorly and laterally. During internal rotation, Figure 2.18(b), the femur is laterally rotated with respect to the tibia during external rotation, Figure 2.18(c), the opposite movement takes place.

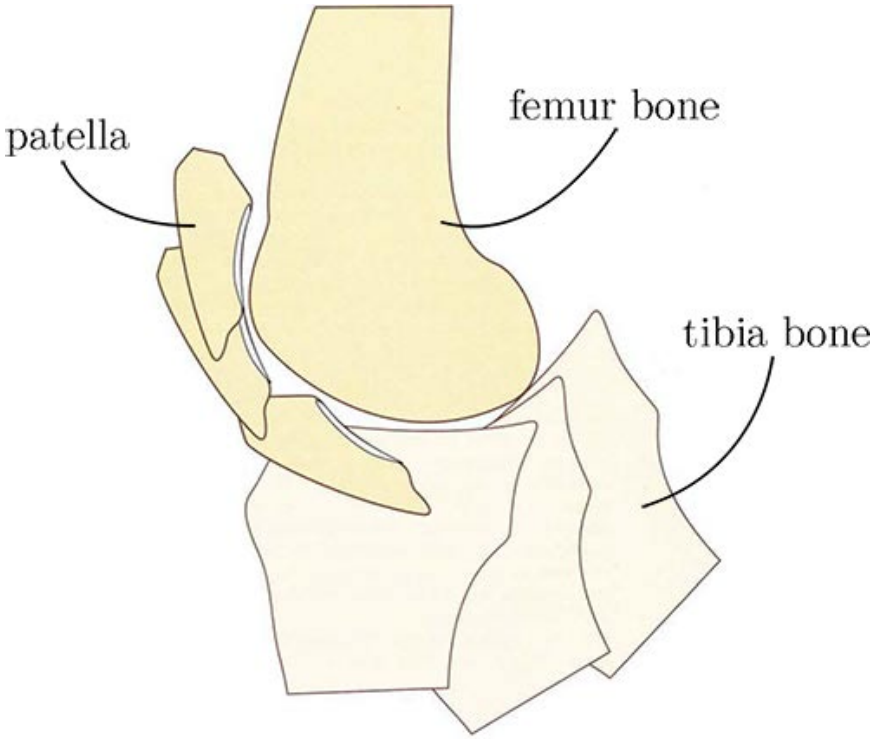

Figure 2.17: Movement of the patella during flexion. Fig. modified from [67].

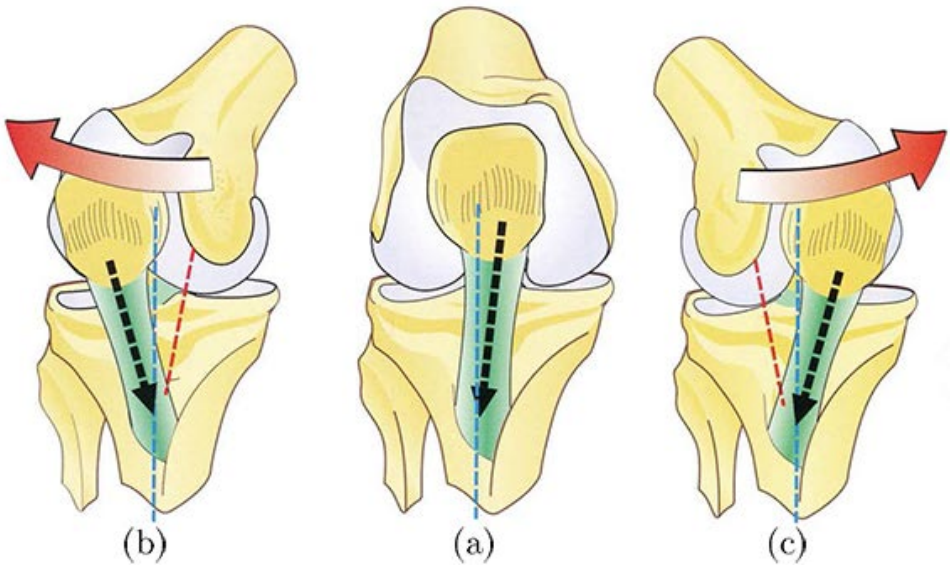

Figure 2.18: Movement of the patella during internal-external rotation; (a) neutral position, (b) internal rotation and (c) external rotation. Fig. modified from [67].

Chapter 3

Theoretical background

This chapter describes a serie of concepts in mathematics and kinematics necessary for experimental data processing and the further synthesis and analysis of the kinematic knee model.

3.1 Mathematical fundamentals

The mathematical approach for the determination of the joint parameters consists in reconstructing the geometries formed by the movement of the origin of a coordinate system B relative to A, for which mathematic concepts such as the least squares method and the description of the 3D geometries are required in order to find the geometry that best fits the set of points.

The fundamentals begin with the least squares method description and the Gauss-Newton algorithm to solve the non-linear least squares problem. After that, the description of each geometry is presented followed by its least squares description of the problem. Lastly, the problem of the projecting points onto a plane is addressed.

3.1.1 Least squares method

The method of least squares is a standard approach in regression analysis to approximate the solution of overdetermined systems, i.e. sets of equations in which there are more equations than unknowns. "Least squares" means that the overall solution minimizes the sum of the squares of the residuals.

The most important application is in data fitting. The best fit in the least squares sense minimizes the sum of the squared residuals (a residiual being: the difference between an observed value, and the fitted value provided by a model), [73]. The function to minimize can be written as:

$$E = \sum_{i=1}^{n} \left(f(C_1, C_2, ..., C_m,\ x_{1i}, x_{2i}, ..., x_{ki}) - f_i \right)^2, \tag{3.1}$$

where n is the number of data, f is the objective function for fitting the data, $C_1, C_2, ..., C_m$ are the best fitting variables to compute, $x_{1i}, x_{2i}, ...x_{k1}$ are the variables from the data and f_i is the function from the data.

The goal is to find the values of the variables, $C_1, C_2, ..., C_m$, for which the objective function, f, best fits the data. Then it is necessary to minimize the function E by setting the following partial derivatives to zero:

$$\frac{\partial E}{\partial C_j} = 0, \qquad j = 1, 2, ..., m. \tag{3.2}$$

Solving the set of equations (3.2) for $C_1, C_2, ..., C_m$. The function f that best fits the data is finally obtained.

Least-squares problem falls into two categories: **linear least squares** and **non-linear least squares**, depending on whether or not the residuals are linear in all unknowns.

Linear least-squares approach

When the residuals $(f(C_1, C_2, ..., C_m,\ x_{1i}, x_{2i}, ..., x_{ki}) - f_i)$ of the function E are linear in the unknown variables $C_1, C_2, ..., C_m$, the problem can be treated by simple algebra, solving the following system:

$$\mathbf{A}\boldsymbol{x} = \boldsymbol{b} \tag{3.3}$$

where:

$$\mathbf{A} = \begin{bmatrix} G_1^1(x_1, x_2, ..., x_k) & G_1^2(x_1, x_2, ..., x_k) & \dots & G_1^m(x_1, x_2, ..., x_k) \\ G_2^1(x_1, x_2, ..., x_k) & G_2^2(x_1, x_2, ..., x_k) & \dots & G_2^m(x_1, x_2, ..., x_k) \\ \vdots & \vdots & \ddots & \vdots \\ G_n^1(x_1, x_2, ..., x_k) & G_n^2(x_1, x_2, ..., x_k) & \dots & G_n^m(x_1, x_2, ..., x_k) \end{bmatrix} \boldsymbol{x} = \begin{bmatrix} C_1 \\ C_2 \\ \vdots \\ C_m \end{bmatrix} \boldsymbol{b} = \begin{bmatrix} f_1 \\ f_2 \\ \vdots \\ f_n \end{bmatrix}$$

Since there are more equations than unknowns the problem generally has no solution because the vector $\boldsymbol{b}$ is not in the column space of $\mathbf{A}$. The problem given in the equation (3.3) can be rewritten as:

$$\mathbf{A}\boldsymbol{x} = \boldsymbol{p}, \tag{3.4}$$

where $\boldsymbol{p}$ is the projection of $\boldsymbol{b}$ onto the column space of $\mathbf{A}$.

Without loss of generality let us address this problem with a 3D equivalent problem that can be visualized in the Figure 3.1.

The key fact of the problem is that the vector $\boldsymbol{e}$ is perpendicular to the plane, this means that $\boldsymbol{b} - \mathbf{A}\boldsymbol{x}$ is perpendicular to any vector on the plane, hence we can write the following two equations:

$$\boldsymbol{a}_1^{\mathrm{T}} (\boldsymbol{b} - \mathbf{A}\boldsymbol{x}) = 0, \qquad \boldsymbol{a}_2^{\mathrm{T}} (\boldsymbol{b} - \mathbf{A}\boldsymbol{x}) = 0,$$

writing these equations in a matrix form, leads to:

$$\begin{bmatrix} \boldsymbol{a}_1^{\mathrm{T}} \\ \boldsymbol{a}_2^{\mathrm{T}} \end{bmatrix} (\boldsymbol{b} - \mathbf{A}\boldsymbol{x}) = 0,$$

$$\mathbf{A}^{\mathrm{T}} (\boldsymbol{b} - \mathbf{A}\boldsymbol{x}) = 0,$$

and the new system to solve is:

$$\mathbf{A}^{\mathrm{T}}\mathbf{A}\boldsymbol{x} = \mathbf{A}^{\mathrm{T}}\boldsymbol{b}.$$

And, the vector $\boldsymbol{x}$ that contains the variables $C_1, C_2, ..., C_m$ can be computed by:

$$\boldsymbol{x} = \left(\mathbf{A}^{\mathrm{T}}\mathbf{A}\right)^{-1} \mathbf{A}^{\mathrm{T}}\boldsymbol{b}. \tag{3.5}$$

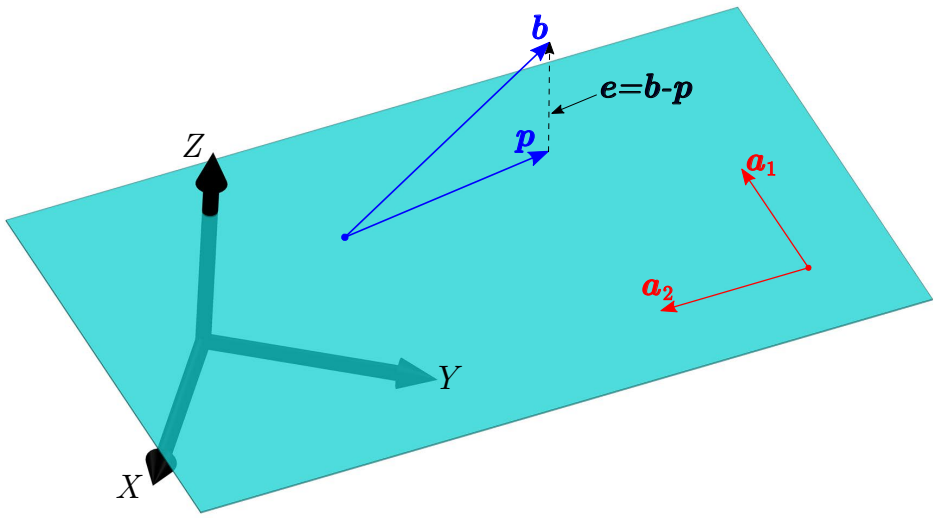

Figure 3.1: Projection $\boldsymbol{p}$ of the vector $\boldsymbol{b}$ onto the plane $\mathbf{A}$.

Non-linear least squares approach

When the residuals $(f(C_1, C_2, ..., C_m,\ x_{1i}, x_{2i}, ..., x_{ki}) - f_i)$ of the function E are non-linear in the unknown variables $C_1, C_2, ..., C_m$, it is necessary to solve the non-linear equations system (3.2) by some complex procedures such as the Sylvester dialytic elimitation or the Bezout method, to have solutions in a closed form [74]. For solutions with numerical methods there is a basic technique called the Gauss-Newton algorithm which is a modification of the Newton-Raphson method, used for solving the problem of non-linear least squares. This algorithm is explained in the following section.

3.1.2 Gauss-Newton algorithm

Let's rewrite the function E from (3.1) in following form:

$$E = \sum_{i=1}^{n} d_i(\boldsymbol{u})^2, \tag{3.6}$$

where $d_i(\boldsymbol{u}) = (f(C_1, C_2, ..., C_m,\ x_{1i}, x_{2i}, ..., x_{ki}) - f_i)$ and the vector $\boldsymbol{u}$ containts the variables to compute, $\boldsymbol{u} = [C_1, C_2, ..., C_m]^{\mathrm{T}}$.

The Gauss-Newton algorithm is an iterative procedure, this means that it requires starting with an initial guess of the solution, $\boldsymbol{u}_0$. The method proceeds by the iterations:

$$\boldsymbol{u}_{s+1} = \boldsymbol{u}_s - \left[\mathbf{J}(\boldsymbol{u}_s)^{\mathrm{T}}\mathbf{J}(\boldsymbol{u}_s)\right]^{-1}\mathbf{J}(\boldsymbol{u}_s)^{\mathrm{T}}\boldsymbol{d}(\boldsymbol{u}_s), \tag{3.7}$$

where $\mathbf{J}(\boldsymbol{u})$ is the Jacobian matrix defined by the partial derivatives of the function $d_i(\boldsymbol{u})$

with respect to each variabe $C_1, C_2, ..., C_m$, given by:

$$\mathbf{J}(\boldsymbol{u}) = \begin{bmatrix} \frac{\partial d_1(\boldsymbol{u})}{\partial C_1} & \frac{\partial d_1(\boldsymbol{u})}{\partial C_2} & \cdots & \frac{\partial d_1(\boldsymbol{u})}{\partial C_m} \\ \frac{\partial d_2(\boldsymbol{u})}{\partial C_1} & \frac{\partial d_2(\boldsymbol{u})}{\partial C_2} & \cdots & \frac{\partial d_2(\boldsymbol{u})}{\partial C_m} \\ \vdots & \vdots & \ddots & \vdots \\ \frac{\partial d_n(\boldsymbol{u})}{\partial C_1} & \frac{\partial d_n(\boldsymbol{u})}{\partial C_2} & \cdots & \frac{\partial d_n(\boldsymbol{u})}{\partial C_m} \end{bmatrix},$$

and the vector $\boldsymbol{d}(\boldsymbol{u})$ contains the function $d_i(\boldsymbol{u})$ evaluated by the data, given by:

$$\boldsymbol{d}(\boldsymbol{u}) = \begin{bmatrix} d_1(\boldsymbol{u}) \\ d_2(\boldsymbol{u}) \\ \vdots \\ d_n(\boldsymbol{u}) \end{bmatrix}.$$

There are two important things that we have to analyse from the Gauss-Newton algorithm given in the equation (3.7). The first is the close relationship of the matrix $\mathbf{J}(\boldsymbol{u})$ with the matrix $\mathbf{A}$, in equation (3.5), of the linear problem.

The second occurs when the number of equations is equal to the number of unknowns, $n = m$, then, the iteration simplifies to:

$$\boldsymbol{u}_{s+1} = \boldsymbol{u}_s - \left[\mathbf{J}(\boldsymbol{u}_s)\right]^{-1} \boldsymbol{d}(\boldsymbol{u}_s), \tag{3.8}$$

which is a direct generalization of the Newton-Raphson method.

3.1.3 Singular value decomposition (SVD)

Singular value decomposition (SVD) is a factorization of a matrix $\mathbf{A}$ into the product of three matrices $\mathbf{A} = \mathbf{U}\mathbf{D}\mathbf{V}^{\mathrm{T}}$ where the columns of $\mathbf{U}$ and $\mathbf{V}$ are orthonormal and the matrix $\mathbf{D}$ is diagonal with positive real entries, [73].

The SVD starts with the statement that the action of a matrix $\mathbf{A}$ on a unit vector $\hat{\boldsymbol{v}}$ is equals to a unit vector $\hat{\boldsymbol{u}}$ times a constant σ, as follows:

$$\mathbf{A}\hat{\boldsymbol{v}} = \sigma\hat{\boldsymbol{u}}, \tag{3.9}$$

extending the problem to a set of unit vectors $\hat{\boldsymbol{v}}_j$, $j = 1, 2, ..., n$ which could be an orthonormal basis. The previous equation can be written in matrix form as:

$$\begin{bmatrix}\mathbf{A}\end{bmatrix}\begin{bmatrix}\hat{\boldsymbol{v}}_1 & \hat{\boldsymbol{v}}_2 & \dots & \hat{\boldsymbol{v}}_n\end{bmatrix} = \begin{bmatrix}\hat{\boldsymbol{u}}_1 & \hat{\boldsymbol{u}}_2 & \dots & \hat{\boldsymbol{u}}_n\end{bmatrix}\begin{bmatrix} \sigma_1 & & & \\ & \sigma_2 & 0 & \\ & 0 & \ddots & \\ & & & \sigma_n \end{bmatrix}$$

$$\mathbf{A}\mathbf{V} = \mathbf{U}\mathbf{D}, \tag{3.10}$$

as the matrix $\mathbf{V}$ is composed by orthonormal vectors, the matrix itself is an orthonormal matrix and $\mathbf{V}^{-1} = \mathbf{V}^{\mathrm{T}}$. Multiplying both sides of the equation (3.10) by $\mathbf{V}^{\mathrm{T}}$ leads to:

$$\mathbf{A} = \mathbf{U}\mathbf{D}\mathbf{V}^{\mathrm{T}}. \tag{3.11}$$

The SVD problem can be solved by reducing it, to an eigenvalue problem, as follows:

$$\begin{aligned} \mathbf{A}^{\mathrm{T}}\mathbf{A} &= \left(\mathbf{U}\mathbf{D}\mathbf{V}^{\mathrm{T}}\right)^{\mathrm{T}}\left(\mathbf{U}\mathbf{D}\mathbf{V}^{\mathrm{T}}\right) \\ &= \mathbf{V}\mathbf{D}\mathbf{U}^{\mathrm{T}}\,\mathbf{U}\mathbf{D}\mathbf{V}^{\mathrm{T}} \\ &= \mathbf{V}\mathbf{D}^2\mathbf{V}^{\mathrm{T}}, \end{aligned} \tag{3.12}$$

thus, multiplying both sides by $\mathbf{V}$ leads to:

$$\begin{aligned} \mathbf{A}^{\mathrm{T}}\mathbf{A}\mathbf{V} &= \mathbf{V}\mathbf{D}^2\mathbf{V}^{\mathrm{T}}\mathbf{V} \\ \mathbf{A}^{\mathrm{T}}\mathbf{A}\mathbf{V} &= \mathbf{V}\mathbf{D}^2 \end{aligned} \tag{3.13}$$

Equation (3.13) is an eigenvalue problem with its eigenvalues $\lambda_j = \sigma_j^2$. By this way we can compute the matrices $\mathbf{V}$ and $\mathbf{D}$. It is easy to see that the matrix $\mathbf{U}$ can be computed in a similar way by the matrix multiplication $\mathbf{A}\mathbf{A}^{\mathrm{T}}$ instead, and then follow the same process.

3.1.4 Fitting a plane

Definition

A plane is a flat surface on which a straight line joining any two points on it would completely lie. Any point $P = (x, y, z)$ represented by vector $\boldsymbol{r}$ onto the plane can be described by the vectorial equation as:

$$\boldsymbol{n} \cdot (\boldsymbol{r} - \boldsymbol{r}_o) = 0 \tag{3.14}$$

where $\boldsymbol{n}$ is a vector orthogonal to the plane and $\boldsymbol{r}_o$ is a vector of an arbitrary point $P_o = (x_o, y_o, z_o)$ onto the plane, as shown in Figure 3.2.

If the normal vector is written as $\boldsymbol{n} = a\hat{\boldsymbol{i}} + b\hat{\boldsymbol{j}} + c\hat{\boldsymbol{k}}$, then, the equation (3.14) leads to the equation of a plane in the **normal form** as:

$$a(x - x_o) + b(y - y_o) + c(z - z_o) = 0 \tag{3.15}$$

Fitting procedure

There are different types of best fit planes. In the least squares sense, there is one type in which the x and y values are fixed and the measured error is in z alone. For this plane the minimized distance is only in the z direction. There is also an orthogonal distance regression, that minimizes the perpendicular distances to the plane. This is used when there is measurement error in all three coordinates.

In this work we are focused on the orthogonal distance regression planes, [75]. Starting with the perpendicular distance from a point to a plane, we wish to find a, b, c and d, such that we minimize the function:

$$E(a, b, c, d) = \sum_{i=1}^{n} \frac{|ax_i + by_i + cz_i + d|^2}{(a^2 + b^2 + c^2)}, \tag{3.16}$$

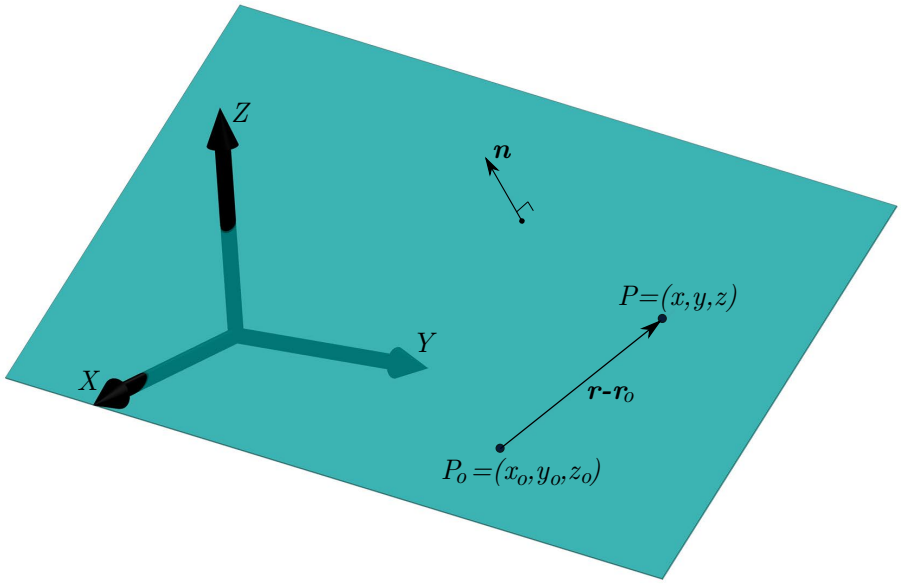

Figure 3.2: Plane in the 3D space with two points on it and the orthogonal vector.

setting the partial derivative with respect to d equal to zero:

$$\frac{\partial E}{\partial d} = 2\sum_{i=1}^{n} \frac{(ax_i + by_i + cz_i + d)}{(a^2 + b^2 + c^2)} = 0,$$

leads to:

$$\sum_{i=1}^{n} (ax_i + by_i + cz_i + d) = 0$$

$$a\sum_{i=1}^{n} x_i + b\sum_{i=1}^{n} y_i + c\sum_{i=1}^{n} z_i + nd = 0,$$

where n is the number of points. Now solving for d:

$$d = -\left[\frac{a}{n}\sum_{i=1}^{n} x_i + \frac{b}{n}\sum_{i=1}^{n} y_i + \frac{c}{n}\sum_{i=1}^{n} z_i\right],$$

or,

$$d = -\left(ax_0 + by_0 + cz_0\right), \tag{3.17}$$

where (x_0, y_0, z_0) is the centroid of the data. This means that the best fit plane contains the centroid. If we substitute it back into the equation (3.16) we can rewrite E as:

$$E(a, b, c) = \sum_{i=1}^{n} \frac{|a(x_i - x_0) + b(y_i - y_0) + c(z_i - z_0)|^2}{(a^2 + b^2 + c^2)}. \tag{3.18}$$

Switching to a matrix representation leads to:

$$f(\boldsymbol{v}) = \frac{\boldsymbol{v}^{\mathrm{T}}\mathbf{M}^{\mathrm{T}}\mathbf{M}\boldsymbol{v}}{\boldsymbol{v}^{\mathrm{T}}\boldsymbol{v}}, \tag{3.19}$$

where:

$$\boldsymbol{v} = \begin{bmatrix} a \\ b \\ c \end{bmatrix}, \qquad \mathbf{M} = \begin{bmatrix} x_1 - x_0 & y_1 - y_0 & z_1 - z_0 \\ x_2 - x_0 & y_2 - y_0 & z_2 - z_0 \\ \vdots & \vdots & \vdots \\ x_n - x_0 & y_n - y_0 & z_n - z_0 \end{bmatrix}.$$

Let's define $\mathbf{A} = \mathbf{M}^{\mathrm{T}}\mathbf{M}$, $f(\boldsymbol{v})$ is called a Rayleigh quotient, [75]. It is minimized by the eigenvector of $\mathbf{A}$ that corresponds to its smallest eigenvalue.

We could compute the eigenvectors of $\mathbf{A}$, but this is not necessary. The singular value decomposition of matrix $\mathbf{M}$ is:

$$\mathbf{M} = \mathbf{U}\mathbf{S}\mathbf{V}^{\mathrm{T}},$$

and:

$$\begin{aligned} \mathbf{A} &= \mathbf{M}^{\mathrm{T}}\mathbf{M} \\ &= \left(\mathbf{U}\mathbf{S}\mathbf{V}^{\mathrm{T}}\right)^{\mathrm{T}}\left(\mathbf{U}\mathbf{S}\mathbf{V}^{\mathrm{T}}\right) \\ &= \left(\mathbf{V}\mathbf{S}^{\mathrm{T}}\mathbf{U}^{\mathrm{T}}\right)\left(\mathbf{U}\mathbf{S}\mathbf{V}^{\mathrm{T}}\right) \\ &= \mathbf{V}\ \mathbf{S}^2\mathbf{V}^{\mathrm{T}} \end{aligned}$$

As seen in the previous section, this decomposition of $\mathbf{A}$ diagonalizes the matrix and provides an eigenvector decomposition. It means that the eigenvalues of $\mathbf{A}$ are the squares of the singular values of $\mathbf{M}$, and the eigenvectors of $\mathbf{A}$ are the singular vectors of $\mathbf{M}$.

To conclude, the orthogonal least squares 3D plane contains the centroid of the data, and its normal vector is the singular vector of $\mathbf{M}$ corresponding to its smallest singular value.

3.1.5 Projecting points onto a plane

Sometimes, a treatement of the data points in a 2-Dimensional space is necessary, then we need to poject the 3D points onto the plane that best fits those points. After this, a new 3D coordinate system with two of its axes lying on the plane (the plane coordinate system) will be required to rewrite the 3D points in terms of the plane system, see Figure 3.3. The problem is solved by means of a line perpendicular to the plane that passes through the objective point, see Figure 3.3, the intersection point between the line and the plane is the projecting point.

A line L is defined by the vectorial equation:

$$\boldsymbol{r} = \boldsymbol{r}_o + t\boldsymbol{l}, \tag{3.20}$$

if $\boldsymbol{r} = [x, y, z]$, $\boldsymbol{r}_o = [x_o, y_o, z_o]$ and $\boldsymbol{l} = [a, b, c]$, equation (3.20) can be written in parametric form as:

$$[x, y, z] = [x_o + at, y_o + bt, z_o + ct], \tag{3.21}$$

where t is called the parameter. When the line is perpendicular to the plane $\boldsymbol{l} = \boldsymbol{n}$, and for the line that passes through the objective point, $\boldsymbol{r}_o$ is the vector of the point P_n.

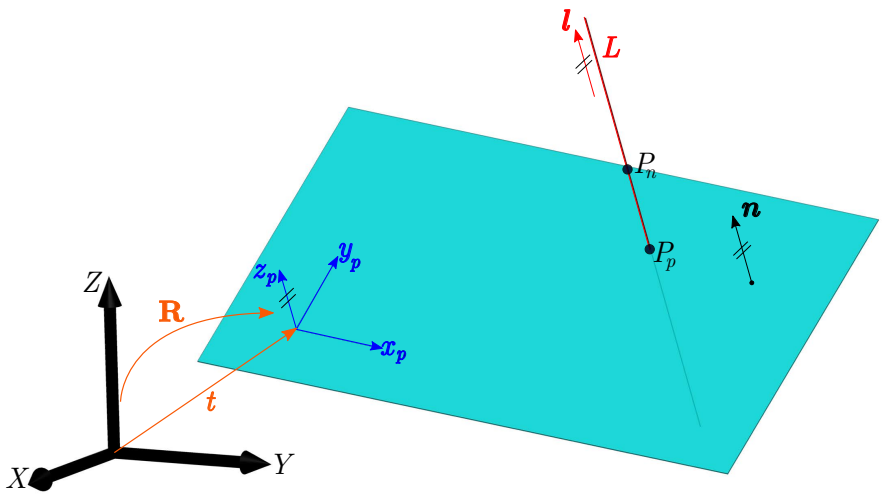

Figure 3.3: Plane with its coordinate system and a line through it in the direction of the orthogonal vector.

The intersection point P_p belongs to the plane and the line at the same time, this is:

$$ax_p + by_p + cz_p = d, \qquad \text{and} \qquad x_p = x_n + at_p, \quad y_p = y_n + bt_p, \quad z_p = z_n + ct_p.$$

Substituting the parametric equations of the line into the equation of the plane and solving for t_p, we obtain the parameter for the intersection point P_p. This parameter t_p can be used in equation (3.21) to find the point P_p.

The point P_p still belongs to the global system XYZ and it is necessary to transform it into the plane system $x_p y_p z_p$. The plane coordinate system can be defined by any two points onto the plane e.g. the centroid $\boldsymbol{r}_0$ and any projection point $\boldsymbol{r}_p$, and the vector $\boldsymbol{n}$, as follows:

$$\hat{\boldsymbol{i}}_p = \frac{\boldsymbol{r}_p - \boldsymbol{r}_0}{|\boldsymbol{r}_p - \boldsymbol{r}_0|}, \qquad \hat{\boldsymbol{k}}_p = \hat{\boldsymbol{n}}, \qquad \hat{\boldsymbol{j}}_p = \hat{\boldsymbol{n}} \times \hat{\boldsymbol{i}}_p. \tag{3.22}$$

The vector of the projected point $\boldsymbol{r}_p$ in coordinates of the plane system $x_p y_p z_p$, i.e. $\boldsymbol{r}_p^p$ is computed as[1]:

$$\boldsymbol{r}_p^p = \mathbf{R}^{\mathrm{T}} \left(\boldsymbol{r}_p - \boldsymbol{r}_0 \right), \tag{3.23}$$

where $\mathbf{R} = \left[\hat{\boldsymbol{i}}_p \;\; \hat{\boldsymbol{j}}_p \;\; \hat{\boldsymbol{k}}_p \right]$. Note that since the axes x_p and y_p lie on the plane, the coordinates of $\boldsymbol{r}_p^p$ have the z_p equal to zero.

3.1.6 Fitting a circle

Definition

A circle is a 2D geometry defined as the geometric place of a point that moves on a plane such that the distance to a fixed point is always constant. The fixed point is called the center of the circle and the constant distance is the radius.

[1]The equation (3.23) is explained in the section **3.2 Kinematical fundamentals**.

The circle with center in the point $C = (h, k)$ and radius r shown in the Figure 3.4, is described by the following equation:

$$(x - h)^2 + (y - k)^2 = r^2. \tag{3.24}$$

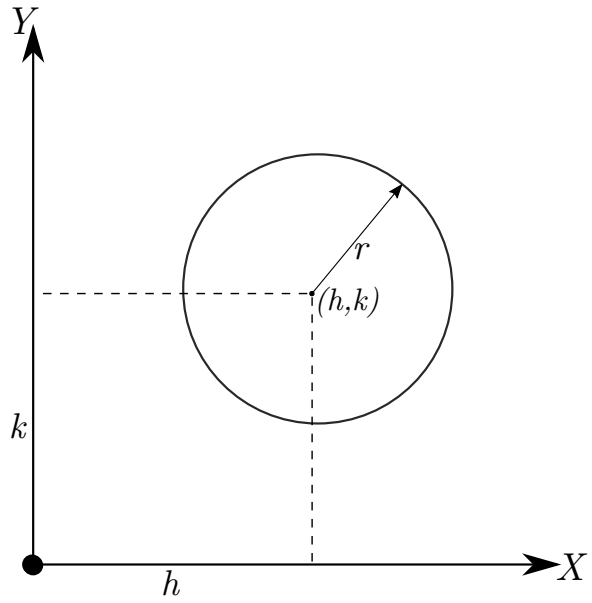

Figure 3.4: Circle with center in (h, k) and radius r.

Fitting procedure

The circle that best fits a set of points is computed by minimizing the diferences of the radii, $r_i - r$, thus $d_i(\boldsymbol{u}) = \sqrt{(x_i - h)^2 + (y_i - k)^2} - r$, this means that it is necessary to find the best center (h, k) and radius r for the circle that best fits the set of points.

The non-linear least squares problem can be written as:

$$E(h, k, r) = \sum_{i=1}^{n} d_i(\boldsymbol{u})^2, \tag{3.25}$$

where $\boldsymbol{u} = [h, k, r]^{\mathrm{T}}$. This problem is solved by the Gauss-Newton algorithm with the iterations given in the equation (3.7). The Jacobian matrix defined by the partial derivatives $\partial d_i(\boldsymbol{u}/\partial u_j)$ is given by:

$$\mathbf{J}(\boldsymbol{u}) = \begin{bmatrix} \frac{x_1 - h}{r_1} & \frac{y_1 - k}{r_1} & -1 \\ \frac{x_2 - h}{r_2} & \frac{y_2 - k}{r_2} & -1 \\ \vdots & \vdots & \vdots \\ \frac{x_n - h}{r_n} & \frac{y_n - k}{r_n} & -1 \end{bmatrix}, \tag{3.26}$$

where $r_i = \sqrt{(x_i - h)^2 + (y_i - k)^2}$, $i = 1, 2, ..., n$.

3.1.7 Fitting a sphere

Definition

A sphere is a 3D geometry defined as the geometric place of a point that moves such that the distance to a fixed point remains contant. The fixed point is called the center of the sphere and the constant distance is the radius. A sphere can be considered as the equivalent of the circle in the three-dimensional space.

The sphere with center in the point $C = (a, b, c)$ and radius r shown in the Figure 3.5, can be described by the following equation:

$$(x - a)^2 + (y - b)^2 + (z - c)^2 = r^2 \tag{3.27}$$

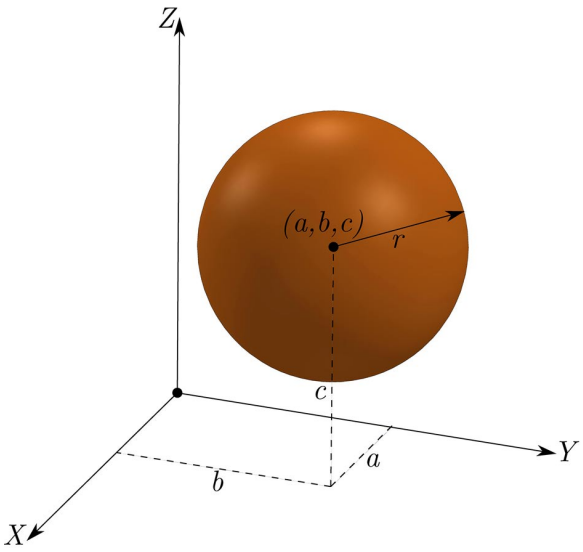

Figure 3.5: Sphere with center in (a, b, c) and radius r.

Fitting procedure

The procedure for fitting a sphere to a set of points is quite similar to the fitting a circle. It consist on minimizing the diferences between the radii, $r_i - r$, thus $d_i(\boldsymbol{u}) = \sqrt{(x_i - a)^2 + (y_i - b)^2 + (z_i - c)^2} - r$, this means that it is necessary to find the center (a, b, c) and the radius r for the sphere that best fits the set of points.

The non-linear least squares problem can be written as:

$$E(a, b, c, r) = \sum_{i=1}^{n} d_i(\boldsymbol{u}^2), \tag{3.28}$$

where $\boldsymbol{u} = [a, b, c, r]^{\mathrm{T}}$. This problem is solved by the Gauss-Newton algorithm with the iterations given in the equation (3.7). The Jacobian matrix defined by the partial

derivatives $\partial d_i(\boldsymbol{u}/\partial u_j)$ is given by:

$$\mathbf{J}(\boldsymbol{u}) = \begin{bmatrix} \frac{x_1-a}{r_1} & \frac{y_1-b}{r_1} & \frac{z_1-c}{r_1} & -1 \\ \frac{x_2-a}{r_2} & \frac{y_2-b}{r_2} & \frac{z_2-c}{r_2} & -1 \\ \vdots & \vdots & \vdots & \vdots \\ \frac{x_n-a}{r_n} & \frac{y_n-b}{r_n} & \frac{z_n-c}{r_n} & -1 \end{bmatrix}, \tag{3.29}$$

where $r_i = \sqrt{(x_i-a)^2+(y_i-b)^2+(z_i-c)^2}$, $i = 1, 2, ..., n$.

3.2 Kinematical fundamentals

In this section, the geometry of spatial displacements defined by coordinate transformations consisting of spatial rotations and translations is developed. The invariants of these transformations are considered and an invariant line is found, called the screw axis. Thus, the geometry of lines becomes important to this study of spatial kinematics.

A convenient set of coordinates for lines, known as Plücker coordinates, are introduced, then generalized to yield screws. This description is used to find the principal joint parameters of the knee. Lastly, the fundamentals of the Denavit-Hartenberg procedure are introduced to make the position analysis of a kinematic chain.

3.2.1 Spatial displacements

A spatial displacement is the composition of a spatial rotation followed by a spatial translation. This transformation takes the coordinates ${}^M\boldsymbol{r} = [x, y, z]^T$ of a point in the moving frame T^M and computes its coordinates ${}^F\boldsymbol{r} = [X, Y, Z]^T$ in the fixed frame T^F as is shown in the Figure 3.6, by the equation:

$${}^F\boldsymbol{r} = \left[{}^F\mathbf{R}^M\right] {}^M\boldsymbol{r} + {}^F\boldsymbol{t}^M \tag{3.30}$$

where ${}^F\mathbf{R}^M$ is a 3×3 rotation matrix of the system T^M relative to the system T^F, and ${}^F\boldsymbol{t}^M$ is a 3×1 translation vector of the origin of the system T^M relative to the system T^F. A spatial displacement preserves the distances between points measured in both T^M and T^F.

From (3.30) we can write the vector ${}^M\boldsymbol{r}$ as:

$${}^M\boldsymbol{r} = \left[{}^F\mathbf{R}^M\right]^{-1} \left({}^F\boldsymbol{r} - {}^F\boldsymbol{t}^M\right),$$

but considering that the rotation matrix is an orthonormal matrix, $\mathbf{R}^{-1} = \mathbf{R}^{\mathrm{T}}$, then:

$${}^M\boldsymbol{r} = \left[{}^F\mathbf{R}^M\right]^T \left({}^F\boldsymbol{r} - {}^F\boldsymbol{t}^M\right). \tag{3.31}$$

Homogeneous transforms

The transformation that defines a spatial displacement is not a linear operation. This can be attributed to the inhomogeneous translation. A standard strategy to adjust for this

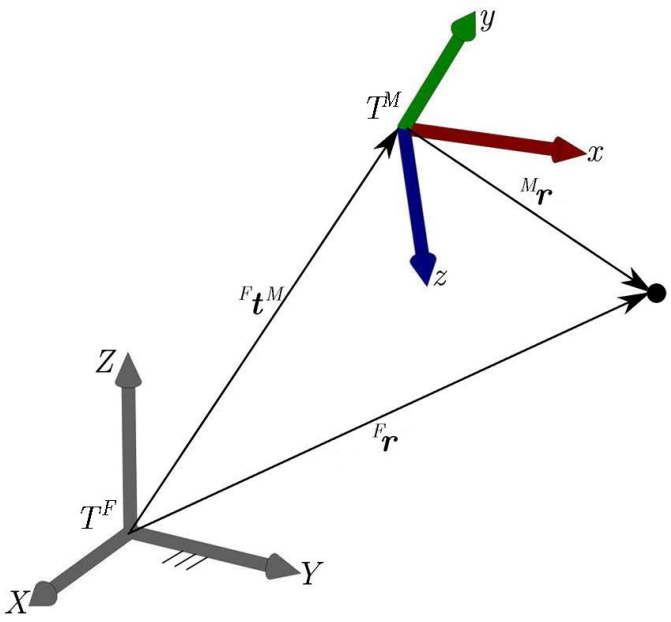

Figure 3.6: Spatial displacement of the frame T^M relative to frame T^F.

inhomogeneity is to add a fourth component to our position vectors that will always equal 1. Therefore we have the 4×4 homogeneous transform:

$$\begin{Bmatrix} {}^F\boldsymbol{r} \\ 1 \end{Bmatrix} = \begin{bmatrix} {}^F\mathbf{R}^M & {}^F\boldsymbol{t}^M \\ \mathbf{0} & 1 \end{bmatrix} \begin{Bmatrix} {}^M\boldsymbol{r} \\ 1 \end{Bmatrix}, \tag{3.32}$$

which we write as:

$${}^F\boldsymbol{r} = \left[{}^F\mathbf{T}^M\right] \, {}^M\boldsymbol{r}, \tag{3.33}$$

where $\mathbf{0}$ is a 1×3 zero vector. Notice that the coordinate vectors that have 1 as their fourth component have not been distinguished by this work. In general, these vectors will have three components. Readers have to assume the addition of the fourth component, when it is appropriate for the use of these 4×4 transforms.

Composition of displacements

The set of matrices that have the structure shown in (3.32) form a matrix group, denoted by $SE(3)$, with matrix multiplicaction as its operation. The matrix product of $\mathbf{T}_1$ and $\mathbf{T}_2$ yields:

$$\mathbf{T}_3 = \begin{bmatrix} \mathbf{R}_1 & \boldsymbol{t}_1 \\ \mathbf{0} & 1 \end{bmatrix} \begin{bmatrix} \mathbf{R}_2 & \boldsymbol{t}_2 \\ \mathbf{0} & 1 \end{bmatrix} = \begin{bmatrix} \mathbf{R}_1\mathbf{R}_2 & \boldsymbol{t}_1 + \mathbf{R}_1\boldsymbol{t}_2 \\ \mathbf{0} & 1 \end{bmatrix}. \tag{3.34}$$

It is easy to see that the 4×4 transform $\mathbf{T}_3$ has the same structure as (3.32) with $\mathbf{R}_3 = \mathbf{R}_1\mathbf{R}_2$ as its rotation matrix and $\boldsymbol{t}_3 = \boldsymbol{t}_1 + \mathbf{R}_1\boldsymbol{t}_2$ as its translation vector.

The composition of displacements $\left[{}^F\mathbf{T}^{M'}\right]$ and $\left[{}^{M'}\mathbf{T}^M\right]$ can be interpreted as follows. Let $\left[{}^F\mathbf{T}^{M'}\right]$ define the position of a frame $T^{M'}$ relative to T^F. Then the position of T^M

relative to $T^{M'}$ is defined by $\left[{}^{M'}\mathbf{T}^{M}\right]$, see Figure 3.7. Thus, the position of the vector ${}^{M}\boldsymbol{r}$ given in the system T^M in terms of the system T^F, ${}^{F}\boldsymbol{r}$ is given by:

$$ {}^{F}\boldsymbol{r} = \left[{}^{F}\mathbf{R}^{M'}{}^{M'}\mathbf{R}^{M}\right] {}^{M}\boldsymbol{r} + {}^{F}\boldsymbol{t}^{M'} + \left[{}^{F}\mathbf{R}^{M'}\right] {}^{M'}\boldsymbol{t}^{M} \tag{3.35} $$

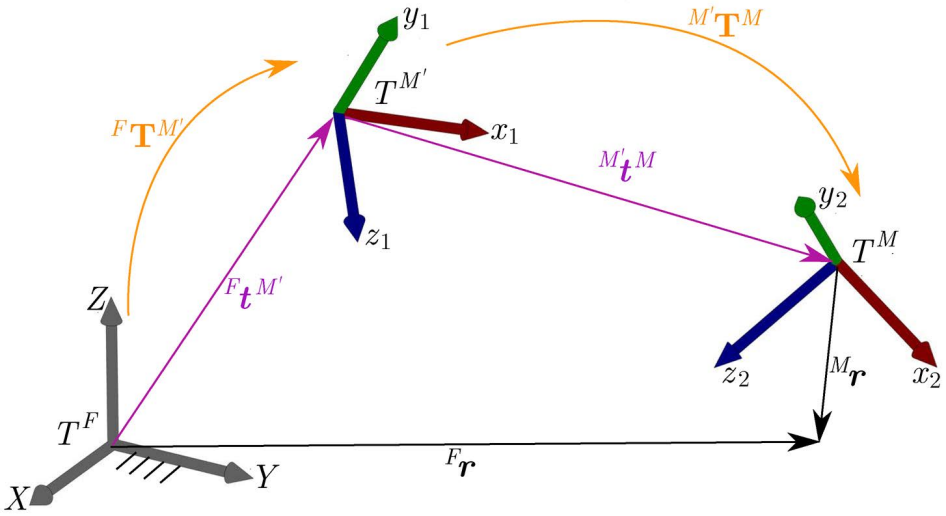

Figure 3.7: Composition of displacements of the frame M relative to frame M' and M' relative to F.

Similarly, the matrix inverse $\mathbf{T}^{-1}$ defines the inverse displacement as:

$$ \mathbf{T}^{-1} = \begin{bmatrix} \mathbf{R}^{T} & -\mathbf{R}^{T}\boldsymbol{t} \\ \mathbf{0} & 1 \end{bmatrix}. \tag{3.36} $$

It is easy to check that $[\mathbf{T}]\,[\mathbf{T}]^{-1} = \mathbf{I}$.

Relative displacements

For a set of displacements $\mathbf{T}_i$, $i = 1, 2, ..., n$, the relative displacement between any two is given by:

$$ \mathbf{T}_{ij} = [\mathbf{T}_j]\,[\mathbf{T}_i]^{-1}. \tag{3.37} $$

This relative displacement is measured in the fixed reference frame T^F as is shown in Figure 3.8.

Screw Displacements

We now consider the invariants of spatial displacements. If a vector $\boldsymbol{r}$ has the same coordinates before and after a spatial displacement $\mathbf{T}$, then it satisfies the following equation:

$$ \boldsymbol{r} = [\mathbf{T}]\,\boldsymbol{r}, \qquad \text{or} \qquad [\mathbf{I} - \mathbf{T}]\,\boldsymbol{r} = 0 \tag{3.38} $$

which simplifies to

$$ [\mathbf{I} - \mathbf{R}]\,\boldsymbol{r} = \boldsymbol{t} \tag{3.39} $$

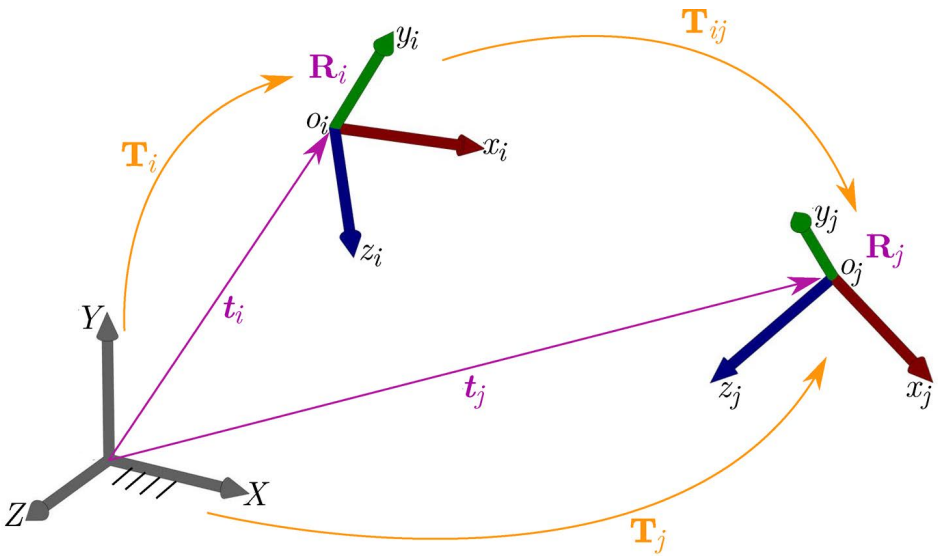

Figure 3.8: Coordinate systems, $x_iy_iz_i$ and $x_jy_jz_j$, and their relative displacement.

Sience all the rotation matrices have 1 as an eigenvalue. Therefore, the 3×3 matrix $[\mathbf{I} - \mathbf{R}]$ is a singular matrix. Thus, a spatial displacement has no fixed points.

While there are no fixed points, there is a line, called the screw axis, that remains fixed during a spatial displacement. To determine this line, we descompose the translation component of the displacement $\mathbf{T}$ into vectors parallel and perpendicular to the rotation axis $\hat{\boldsymbol{s}}$ of $\mathbf{R}$ determined by the eigenvector relates with the eigenvalue 1 of $\mathbf{R}$, that is:

$$\boldsymbol{t} = \boldsymbol{t}^* + k\hat{\boldsymbol{s}} \qquad \text{where} \qquad k = \boldsymbol{r} \cdot \hat{\boldsymbol{s}}. \tag{3.40}$$

From the spherical displacements it is known that a rotational displacement $\mathbf{R}$ has a fixed point, see reference [76], given by:

$$\boldsymbol{p} = \frac{\boldsymbol{b} \times (\boldsymbol{t}^* - \boldsymbol{b} \times \boldsymbol{t}^*)}{2\boldsymbol{b} \cdot \boldsymbol{b}}, \tag{3.41}$$

where $\boldsymbol{b} = \sin(\theta/2)\,\hat{\boldsymbol{s}}$ is the Rodrigues's vector of the rotation matrix $\mathbf{R}$. Now consider the line S through this point in the direction of the rotation axis of $\mathbf{R}$, defined by:

$$S: \quad \boldsymbol{r} = \boldsymbol{p} + \lambda\hat{\boldsymbol{s}}. \tag{3.42}$$

Points on this line remain fixed during the rotational displacement $\mathbf{R}$. Furthermore, the translation $k\hat{\boldsymbol{s}}$ slides points along this line by the distance k. This line remains fixed during the spatial displacement.

Thus, a general spatial displacement consists on a rotation by θ about this line and the sliding distance k along it.

3.2.2 The vector $\hat{s}$ and the angle θ of a rotation matrix

From the Figure 3.9, it can be obtained the following equation, see reference [77]:

$$\boldsymbol{r}' = \cos\theta\boldsymbol{r} + (1 - \cos\theta)(\hat{\boldsymbol{s}} \cdot \boldsymbol{r})\hat{\boldsymbol{s}} + \sin\theta\hat{\boldsymbol{s}} \times \boldsymbol{r}, \tag{3.43}$$

where the position vector $\boldsymbol{r}'$ is computed after a rotational displacement of $\boldsymbol{r}$ by means of the direction $\hat{\boldsymbol{s}}$ and the angle of rotation θ.

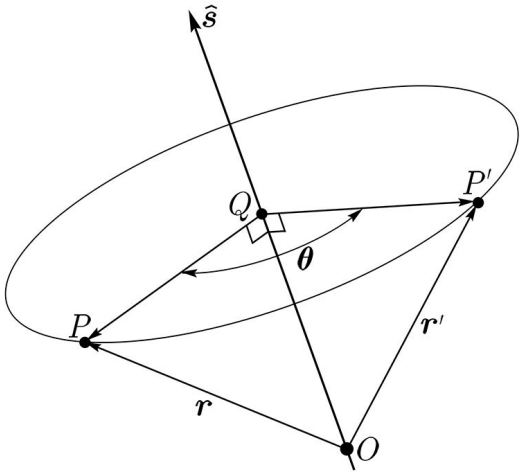

Figure 3.9: Image $\boldsymbol{r}'$ of $\boldsymbol{r}$ under a rotation of θ around $\hat{\boldsymbol{s}}$.

The equation (3.43) can be written in matrix form as:

$$\boldsymbol{r}' = \mathbf{R}\boldsymbol{r}, \tag{3.44}$$

where [77]:

$$\mathbf{R} = \begin{bmatrix} \mathrm{C}\theta + (1-\mathrm{C}\theta)\, s_x^2 & (1-\mathrm{C}\theta)\, s_x s_y - \mathrm{S}\theta s_z & (1-\mathrm{C}\theta)\, s_x s_z + \mathrm{S}\theta s_y \\ (1-\mathrm{C}\theta)\, s_x s_y - \mathrm{S}\theta s_z & \mathrm{C}\theta + (1-\mathrm{C}\theta)\, s_y^2 & (1-\mathrm{C}\theta)\, s_y s_z - \mathrm{S}\theta s_x \\ (1-\mathrm{C}\theta)\, s_x s_z + \mathrm{S}\theta s_y & (1-\mathrm{C}\theta)\, s_y s_z - \mathrm{S}\theta s_x & \mathrm{C}\theta + (1-\mathrm{C}\theta)\, s_z^2 \end{bmatrix}. \tag{3.45}$$

Therefore, from this matrix we can compute the vector $\hat{\boldsymbol{s}}$ along the rotation axis, as:

$$\hat{\boldsymbol{s}} = \frac{1}{2\sin\theta} \begin{bmatrix} \left(\mathbf{R} - \mathbf{R}^{\mathrm{T}}\right)_{32} \\ \left(\mathbf{R} - \mathbf{R}^{\mathrm{T}}\right)_{13} \\ \left(\mathbf{R} - \mathbf{R}^{\mathrm{T}}\right)_{21} \end{bmatrix}, \tag{3.46}$$

where $\left(\mathbf{R} - \mathbf{R}^{\mathrm{T}}\right)_{ij}$ is the i, j element of the matrix into the parenthesis.

Since $\hat{\boldsymbol{s}}$ is a unit vector, it is easy to see that:

$$\sin\theta = \frac{1}{2}\sqrt{(\mathbf{R} - \mathbf{R}^{\mathrm{T}})_{32}^2 + (\mathbf{R} - \mathbf{R}^{\mathrm{T}})_{13}^2 + (\mathbf{R} - \mathbf{R}^{\mathrm{T}})_{21}^2}, \tag{3.47}$$

and from (3.45):

$$\cos\theta = \frac{1}{2}\left[\mathrm{Tr}\left(\mathbf{R}\right) - 1\right], \tag{3.48}$$

where $\mathrm{Tr}\left(\mathbf{R}\right)$ is the trace of the matrix $\mathbf{R}$.

Therefore, the rotation angle is given by:

$$\theta = \tan^{-1}\frac{\sin\theta}{\cos\theta}. \tag{3.49}$$

3.2.3 Lines and screws

The geometry of the screw axis of a spatial displacement is best studied using Plücker's coordinates that define the line directly. Plücker coordinates of a line is a six-dimensional vector assembled with the direction vector of the line and its moment about the origin of the reference frame.

Plücker coordinates of a line

Consider the line S through two points $\boldsymbol{r}_C$ and $\boldsymbol{r}_Q$ in space, given by the parameterized equation:

$$S : \boldsymbol{r} = \boldsymbol{r}_C + \lambda \hat{\boldsymbol{s}} \qquad \lambda \in \mathrm{R}, \tag{3.50}$$

where $\boldsymbol{r}_C$ has been selected as reference point on the line, and $\hat{\boldsymbol{s}}$ is the unit vector along $\boldsymbol{r}_Q - \boldsymbol{r}_C$. To eliminate the free parameter λ in the definition of S, we introduce the Plücker coordinates of the line, [76]:

$$S = \begin{Bmatrix} \hat{\boldsymbol{s}} \\ \boldsymbol{r}_C \times \hat{\boldsymbol{s}} \end{Bmatrix} = \begin{Bmatrix} \hat{\boldsymbol{s}} \\ \boldsymbol{s}_O \end{Bmatrix}. \tag{3.51}$$

The vector $\boldsymbol{s}_O$ is the moment of the line about the origin of the reference frame, see Figure 3.10.

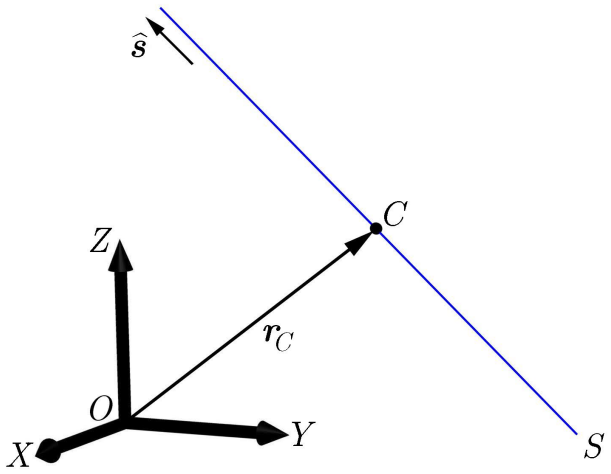

Figure 3.10: The direction $\hat{\boldsymbol{s}}$ and the vector $\boldsymbol{r}_C$ of the point C onto the line S.

Notice that these coordinates do not depend on the choice of the reference point $\boldsymbol{r}_C$.

A general pair of vectors $W = (\boldsymbol{w}, \boldsymbol{v})^T$ can be the Plücker coordinates of a line only if $\boldsymbol{w} \cdot \boldsymbol{v} = 0$. This is equivalent to saying that there must be a vector $\boldsymbol{r}_C$ such that:

$$\boldsymbol{r}_C \times \boldsymbol{w} = \boldsymbol{v}. \tag{3.52}$$

Solve this equation by computing the vector product of both sides by $\boldsymbol{w}$ to obtain:

$$\boldsymbol{r}_C = \frac{\boldsymbol{w} \times \boldsymbol{v}}{\boldsymbol{w} \cdot \boldsymbol{w}}. \tag{3.53}$$

This formula defines the coordinates for the reference point directly in terms of the Plücker coordinates of the line.

Plücker coordinates are homogeneous, which means that λS represents the same line as S.

Screws

A general pair of vectors $(\boldsymbol{w}, \boldsymbol{v})^T$ for which $\boldsymbol{w} \cdot \boldsymbol{v} \neq 0$ and $|\boldsymbol{w}| \neq 1$ is called a screw \$. It is possible to associate with any screw \$, a line S, called the axis of the screw. To do this, decompose the second vector $\boldsymbol{v}$ into parallel and perpendicular components to $\boldsymbol{w}$, so we have $\boldsymbol{v} = p_w \boldsymbol{w} + \boldsymbol{v}^*$. Since $\boldsymbol{w} \cdot \boldsymbol{v}^* = 0$, we can determine a point $\boldsymbol{r}_C$ such that, $\boldsymbol{r}_C \times \boldsymbol{w} = \boldsymbol{v}^*$ by the equation (3.53).

The line $S = (\boldsymbol{w}, \boldsymbol{r}_C \times \boldsymbol{w})^T$ is the axis of the screw \$. Let $\boldsymbol{w} = w\hat{\boldsymbol{s}}$, then, the components of this screw can be written in the form:

$$\$ = \begin{Bmatrix} w\hat{\boldsymbol{s}} \\ w\boldsymbol{r}_C \times \hat{\boldsymbol{s}} + wp_w\hat{\boldsymbol{s}} \end{Bmatrix}. \tag{3.54}$$

The parameter $w = ||\boldsymbol{w}||$ is called the magnitude of the screw, and:

$$p_w = \frac{\boldsymbol{w} \cdot \boldsymbol{v}}{\boldsymbol{w} \cdot \boldsymbol{w}}, \tag{3.55}$$

is its pitch.

Lines are often called zero-pitch screws.

3.3 Denavit-Hartenberg notation

The Denavit-Hartenberg notation models chains of bodies connected by joints. Originally they were applied to single-loop chains but are now almost universally applied to open-loop serial chains such as robotic manipulators. Unfortunately there are several popular variations of the notation: the original, the distal variant, and the proximal variant.

It has been some sixty years since Jacques Denavit and Richard S. Hartenberg introduced the ubiquitous and celebrated kinematic notation bearing their names [78].

Unfortunately there are several popular variations of the notation: the original, the distal variant popularized by the Paul's textbook [79], and the proximal variant popularized by Craig's textbook [80].

In this section the fundamentals of the DH notation are explained and the three cases are compared for their application to serial robots.

3.3.1 Denavit-Hartenberg parameters

Both the original DH notation and their variants use four parameters (θ_i, d_i, α_i, a_i) denominated the DH parameters. These parameters define angles and distances between two consecutive coordinate system's axes and specify the relative pose between them. This way, the subscript i is related with one of the two involved systems. In this work, each of the parameters is referred to as:

- θ_i: rotation angle of the kinematic joint,
- d_i: translation along the direction of the kinematic pair,
- α_i: rotation angle of the link,
- a_i: link length.

This notation was taken from [81], but it should be clarified that these parameters were not used by Denavit and Hartenberg in the original notation except for a_i.

In the most general case, six parameters are necessary to locate a coordinate system relative to other. However, there are two additional conditions imposed over the z_i and x_i axes of a coordinate system: i) they intersect, and ii) they are perpendicular. That is the reason, that only four independent parameters are needed to locate a coordinate system with respect to another.

The DH parameters describe the dimentions of the kinematic chains connected by joints of 1-DoF (revolute joints, prismatic joints and screw joints). The kinematic joints of more than 1-DoF could be replaced by combinations of 1-DoF joints.

Finally, the pose of the coordinate system attached to the end effector link, t, of the kinematic chain relative to the coordinate system of the fixed link, f, defined by ${}^f\mathbf{T}^t$ is given by a composition of translations and rotations along and around the axes, x_i and z_i. These displacements can be written as homogeneous transforms by:

$$\mathbf{X}_i(a_i, \alpha_i) \qquad \text{and} \qquad \mathbf{Z}_i(d_i, \theta_i), \tag{3.56}$$

3.3.2 Comparison between DH conventions

Conventions differ in the way to define the DH parameters. Harvey Lipkin [81] presented a detailed comparison between the three popular variations: the original, the distal variant and the proximal variant. Figure 3.11 illustrates the way that the three conventions set coordinate systems to a kinematic chain, and Tables 3.1, 3.2 and 3.3 are a summary of the ways to define the DH parameters for each convention.

Table 3.1: DH parameters for the original convention.

Original convention		
Measuring axis	z_i	x_{i+1}
DH parameters	θ_i, d_i	α_i, a_i
Axes to measure the parameters	$x_i \rightarrow x_{i+1}$	$z_i \rightarrow z_{i+1}$

Table 3.2: DH parameters for the distal variant.

Distal variant		
Measuring axis	z_{i-1}	x_i
DH parameters	θ_i, d_i	α_i, a_i
Axes to measure the parameters	$x_{i-1} \rightarrow x_i$	$z_{i-1} \rightarrow z_i$

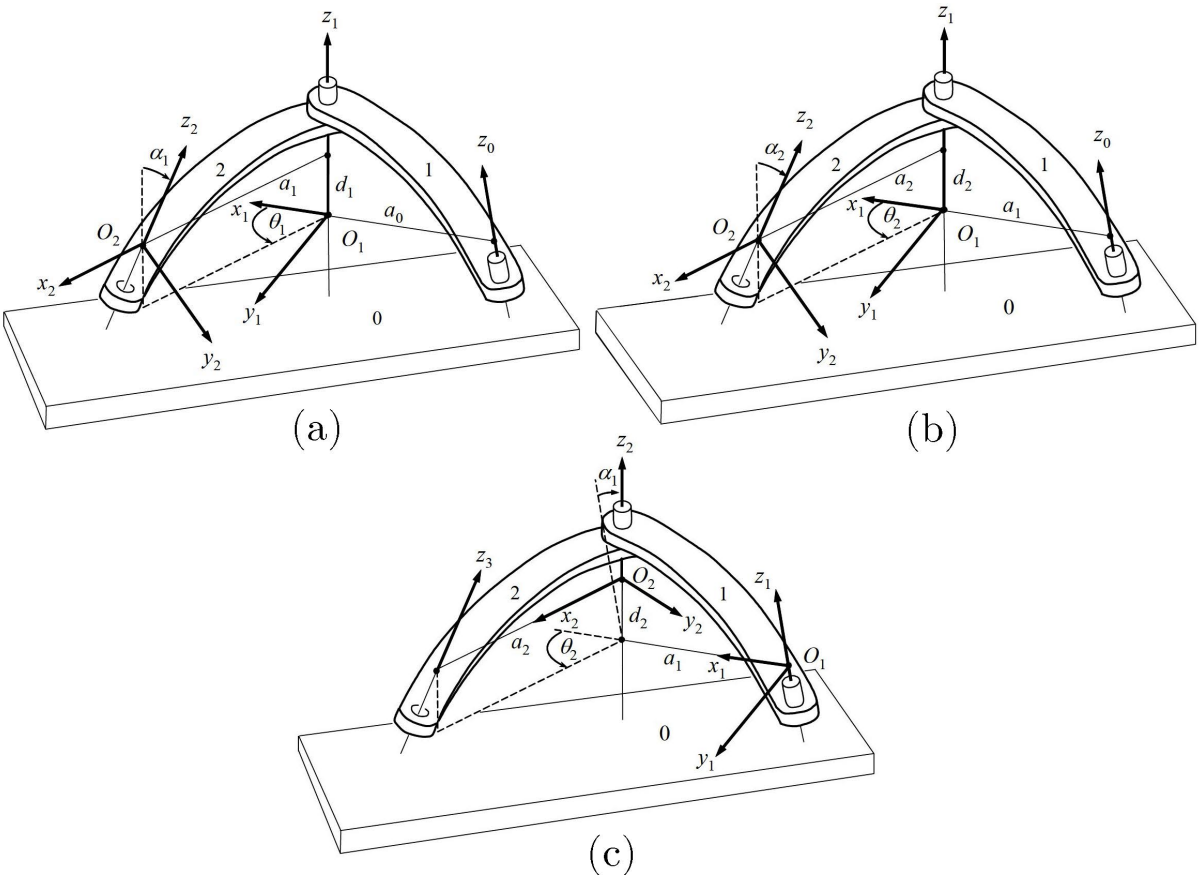

Figure 3.11: (a) original Denavit-Hartenberg convention, (b) distal variant of Denavit-Hartenberg notation and (c) proximal variant of Denavit-Hartenberg notation. Fig. extracted from [81].

Table 3.3: DH parameters for the proximal variant.

Proximal variant		
Measuring axis	z_i	x_i
DH parameters	θ_i, d_i	α_i, a_i
Axes to measure the parameters	$x_{i-1} \rightarrow x_i$	$z_i \rightarrow z_{i+1}$

A successful notation balances clarity against conciseness. Lipkin proposed in [81], five subjective criteria to evaluate Denavit-Hartenberg notation and its variants for serial robot analyses. In order of importance the criteria are deemed as:

1. Frame i is rigidly attached to link i.
2. Displacements θ_i and d_i are measured about z_i.
3. Displacements α_i and a_i are measured about x_i.
4. The first joint displacement is θ_1 or d_1.
5. The ground is link 0.

Table 3.4 compares the properties of the three notational conventions, where the proximal variant is the only one that satisfies all the criteria. Therefore the proximal variant is advanced as the most notationally transparent for the mechanical analysis of serial manipulators.

Table 3.4: Comparison of properties for the three notational conventions. ✓ denotes satisfied property, × denotes unsatisfied property and ⊕ denotes mutually exclusive properties.

No.	**Criteria**	**Original**	**Distal**	**Proximal**
1	Frame i on link i	✓	✓	✓
2	θ_i, d_i along z_i	✓	×	✓
3	α_i, a_i along x_i	×	✓	✓
4	α_i, a_i along joint 1	⊕	✓	✓
5	Link 0 is ground	⊕	✓	✓

Chapter 4

Measurement system

Obtaining the knee work-space is based on a simple statement: "the measurement of 3D coordinate systems and their relative displacements". To do this, a measurement system based on photogrammetric techniques is implemented. Through this chapter, the measurement system is described and the mathematical background of the technique is explained. Moreover, an accuracy study is developed to prove the reliability of the system.

4.1 Description

The measurement system for the obtention of the knee work-space is a photogrammetric system based on a single camera and simple planar patterns, see Figure 4.1.

(a) (b)

Figure 4.1: Measurement system; (a) Camera and (b) planar patterns.

The camera used in this project is a Genie Nano C2020 by Teledyne [82] (the little one in the Figure 4.1), and the planar patterns were printed on a laser printer using special thin paper attached to rectangular pieces of flat glass. Patterns with squares of 5 mm and 10 mm of length were printed.

The technique consists on extracting a 3D coordinate frame from each image pattern from each image captured by the camera, as is shown in Figure 4.2. The pose information of these patterns is relative to the camara coordinate frame however, making use of the equation (3.37) the relative displacement, $\mathbf{T}_{ij}$, between coordinate frames can be computed.

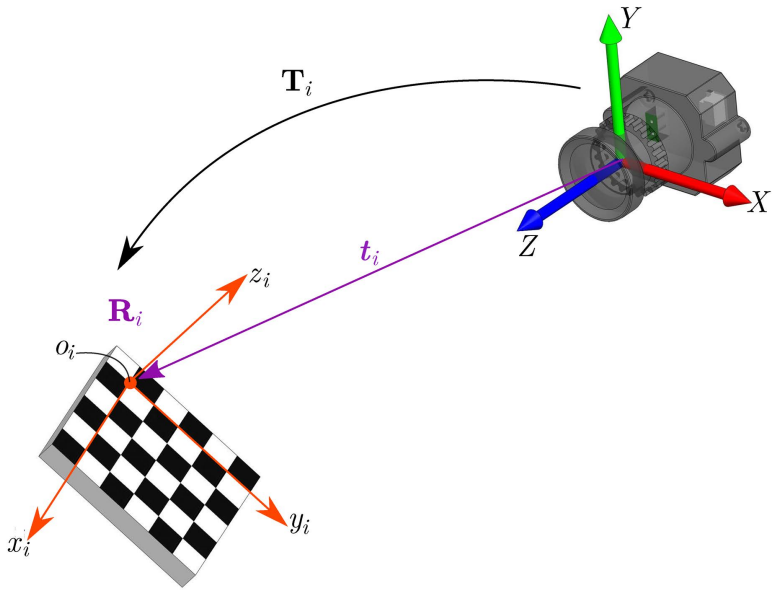

Figure 4.2: Transformation between the coordinate systems of pattern and camera.

The capability to exctract reliable 3D coordinate systems from 2D images of the planar patterns is thoroughly related with the camera calibration procedure, explained below.

4.2 Camera calibration procedure

Camera calibration is a necessary step in 3D computer vision in order to extract metric information from 2D images. It consists in computing the geometric and optic characteristics of the camera known as the extrinsic and intrinsic parameters.

It is possible to classify the techniques of camera calibration into two principal categories:

- **Photogrammetric calibration:** calibration is performed by observing a calibration object whose geometry in 3D space is known with good precision. A calibration object usually consists of two or three planes orthogonal to each other. These approaches require an expensive calibration apparatus, and an elaborate setup.

- **Self-calibration:** techniques in this category do not use any calibration object. Just by moving a camera in a static scene, the rigidity of the scene provides in general two constraints [83] on the cameras internal parameters from one camera displacement by using image information alone. Therefore, correspondences between three images are sufficient to recover both internal and external parameters. While this approach is very flexible, there are many parameters to stimate, reliable results are not always obtained.

The camera calibration procedure in the current research is focused on a desktop vision system (DVS) since the potential for using DVSs is large. Cameras are becoming cheap and ubiquitous. A DVS aims at the general public, who are not experts in computer

vision and will not be willing to invest big amounts of money for expensive equipment. Therefore, flexibility, robustness and low cost are important.

The technique has the advantage that it only requires the camera to observe a planar pattern shown at a few (at least two) different poses (position and orientation). The pattern can be printed on a laser printer and attached to a "reasonable" planar surface. The motion need not be known. This approach lies between the photogrammetric calibration and self-calibration, because 2D metric information is used, rather than 3D or purely implicit one.

The procedure starts with a closed form solution based on the homography or projection matrix, followed by a non-linear refining based on the maximum likelihood criterion and the distortion coefficients are also estimated.

The calibration technique described above is implemented in the open access **Camera Calibration Toolbox** for Matlab® by Jean-Yves Bouguet [84] and it is mainly based in Zhang's proposal [6] with the minor difference that it uses the intrinsic model presented by Heikkila and Silven [85] including two extra distortion coefficients corresponding to tangential distortion.

4.2.1 Camera parameters

Figure 4.3 displays the principal elements in the geometric model of the camera necessary to stablish the relationship between a 3D point in the global frame, $\boldsymbol{M} = [x, y, z]^T$, and its corresponding 2D point, $\boldsymbol{m} = [u, v]^T$, in the image frame. Let us keep the same notation to denote the augmented vector by adding 1 as the last element: $\boldsymbol{m} = [u, v, 1]^T$ and $\boldsymbol{M} = [x, y, z, 1]^T$.

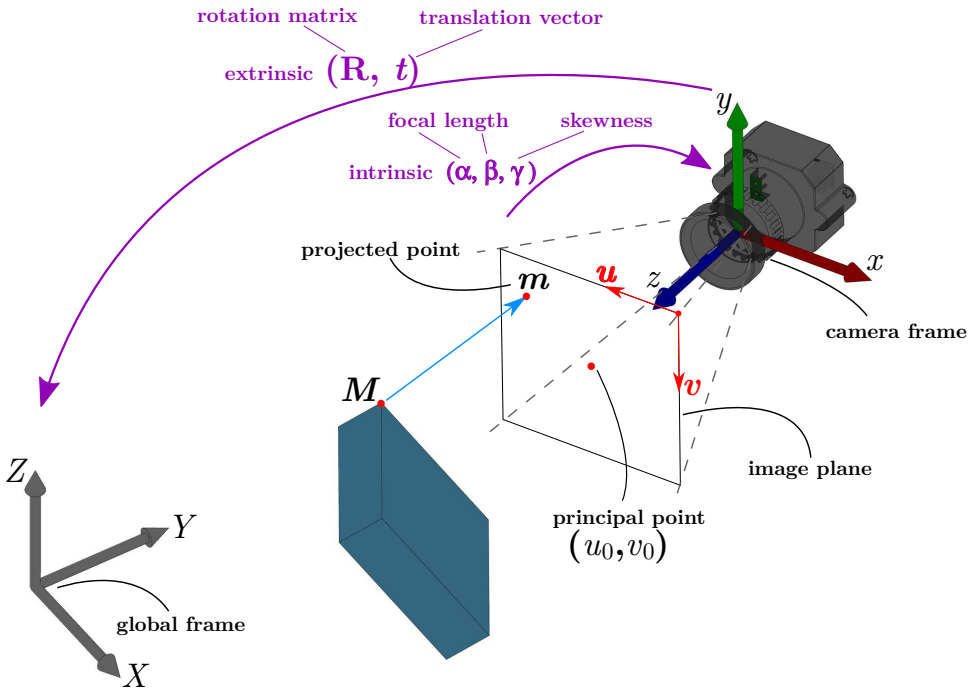

Figure 4.3: Camera intrinsic and extrinsic parameters. Fig. based on [6]

The relationship between a 3D point $\boldsymbol{M}$ and its image projection $\boldsymbol{m}$ is given by:

$$s\boldsymbol{m} = \mathbf{A}\begin{bmatrix}\mathbf{R} & \boldsymbol{t}\end{bmatrix}\boldsymbol{M}, \qquad \text{where} \quad \mathbf{A} = \begin{bmatrix}\alpha & \gamma & u_0 \\ 0 & \beta & v_0 \\ 0 & 0 & 1\end{bmatrix}, \tag{4.1}$$

where s is an arbitrary scale factor; $\mathbf{R}$ and $\boldsymbol{t}$, called the extrinsic parameters, are the rotation and translation of the camera reference frame with respect to a real world reference; $\mathbf{A}$ is called the camera intrinsic matrix which contains the intrinsic parameters: the coordinates of **the principal point**, (u_0, v_0); **the focal length** in scale factors, α and β; and **the skew coefficient** of the two image axes, γ.

Matrix $\mathbf{A}$ relates the pixel image coordinate system with the camera metric coordinate system, while the matrix $\begin{bmatrix}\mathbf{R} & \boldsymbol{t}\end{bmatrix}$ relates the global coordinate system to the camera coordinate system.

4.2.2 Zhang's algorithm

The Zhang's algorithm [6] is based on computing the homography or projection matrix between the model plane, which consists of an arrangement of coplanar points, and its corresponding camera image for n number of images, as is shown in Figure 4.4, with information about the dimensions of those planar patterns.

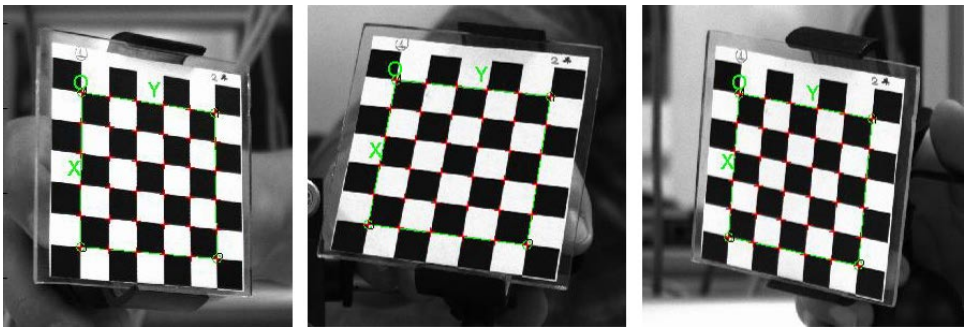

Figure 4.4: Arrangement of coplanar points in three diferent poses.

Without loss of generality, we assume that the model plane is on the $Z = 0$ of the global coordinate system. Therefore, a model point $\boldsymbol{M}$ and its image $\boldsymbol{m}$ is related by an homography matrix $\mathbf{H}$ as follows:

$$s\boldsymbol{m} = \mathbf{H}\boldsymbol{M} \qquad \text{with} \quad \mathbf{H} = \mathbf{A}\begin{bmatrix}\boldsymbol{r}_1 & \boldsymbol{r}_2 & \boldsymbol{t}\end{bmatrix}. \tag{4.2}$$

Given an image of the model plane, a homography can be estimated [6]. It can be denoted by $\mathbf{H} = [\boldsymbol{h}_1 \quad \boldsymbol{h}_2 \quad \boldsymbol{h}_3]$. From (4.2), we have:

$$[\boldsymbol{h}_1 \quad \boldsymbol{h}_2 \quad \boldsymbol{h}_3] = \lambda\mathbf{A}\begin{bmatrix}\boldsymbol{r}_1 & \boldsymbol{r}_2 & \boldsymbol{t}\end{bmatrix},$$

where λ is an arbitrary scalar. The algorithm also takes advantage of the orthonormal property of the rotation matrix to obtain two fundamental constraints:

$$\boldsymbol{h}_1^T\mathbf{A}^{-T}\mathbf{A}^{-1}\boldsymbol{h}_2 = 0 \tag{4.3}$$

$$\boldsymbol{h}_1^T\mathbf{A}^{-T}\mathbf{A}^{-1}\boldsymbol{h}_1 = \boldsymbol{h}_2^T\mathbf{A}^{-T}\mathbf{A}^{-1}\boldsymbol{h}_2\,. \tag{4.4}$$

Closed-form solution

Let:

$$\mathbf{B} = \mathbf{A}^{-T}\mathbf{A}^{-1} \equiv \begin{bmatrix} B_{11} & B_{12} & B_{13} \\ B_{12} & B_{22} & B_{23} \\ B_{13} & B_{23} & B_{33} \end{bmatrix}. \tag{4.5}$$

Note that $\mathbf{B}$ is symmetric, defined by a 6D vector as follows:

$$\boldsymbol{b} = [B_{11}, B_{12}, B_{22}, B_{13}, B_{23}, B_{33}]^T. \tag{4.6}$$

Let the i-th column vector of $\mathbf{H}$ be $\boldsymbol{h}_i = [h_{i1}, h_{i2}, h_{i3}]^T$. As a result, we have:

$$\boldsymbol{h}_i^T \mathbf{B} \boldsymbol{h}_j = \boldsymbol{v}_{ij}^T \boldsymbol{b}, \tag{4.7}$$

with $\boldsymbol{v}_{ij} = [h_{i1}h_{j1}, h_{i1}h_{j2} + h_{i2}h_{j1}, h_{i2}h_{j2}, h_{i3}h_{j1} + h_{i1}h_{j3}, h_{i3}h_{j2} + h_{i2}h_{j3}, h_{i3}h_{j3}]^T$. Therefore, the two fundamental constraints (4.3) and (4.4), from a given homography, can be rewritten as two homogeneous equations in $\boldsymbol{b}$:

$$\begin{bmatrix} \boldsymbol{v}_{12}^T \\ (\boldsymbol{v}_{11} - \boldsymbol{v}_{22})^T \end{bmatrix} \boldsymbol{b} = \mathbf{0}, \tag{4.8}$$

which can be solved for $\boldsymbol{b}$ with n images in order to obtain an estimation of the matrix $\mathbf{A}$ as follows:

$$\begin{aligned} v_0 &= (B_{12}B_{13} - B_{11}B_{23}) / (B_{11}B_{22} - B_{12}^2) \\ \lambda &= B_{33} - \left[B_{13}^2 + v_0 (B_{12}B_{13} - B_{11}B_{23})\right] / B_{11} \\ \alpha &= \sqrt{\lambda / B_{11}} \\ \beta &= \sqrt{\lambda B_{11} (B_{11}B_{22} - B_{12}^2)} \\ \gamma &= -B_{12}\alpha^2\beta\lambda \\ u_0 &= \gamma v_0 / \alpha - B_{13}\alpha^3 / \lambda \,. \end{aligned}$$

Once $\mathbf{A}$ is known, the extrinsic parameters for each image is readily computed. From (4.2), we have:

$$\boldsymbol{r}_1 = \lambda \mathbf{A}^{-1}\boldsymbol{h}_1, \quad \boldsymbol{r}_2 = \lambda \mathbf{A}^{-1}\boldsymbol{h}_2, \quad \boldsymbol{r}_3 = \boldsymbol{r}_1 \times \boldsymbol{r}_2, \quad \boldsymbol{t} = \lambda \mathbf{A}^{-1}\boldsymbol{h}_3 \,.$$

Maximum likelihood estimation

The final solution is obtained through minimizing the algebraic distance between the projection point, $\boldsymbol{m}$, and its reprojection point, $\check{\boldsymbol{m}}$.

We have n images of a model plane and there are m points on the model plane. The maximum likelihood estimation can be obtained by minimizing the following function:

$$\sum_{i=1}^{n} \sum_{j=1}^{m} ||\boldsymbol{m}_{ij} - \check{\boldsymbol{m}}(\mathbf{A}, \mathbf{R}_i, \boldsymbol{t}_i, \boldsymbol{M}_j)||^2, \tag{4.9}$$

where $\check{\boldsymbol{m}}\left(\mathbf{A}, \mathbf{R}_i, \boldsymbol{t}_i, \boldsymbol{M}_j\right)$ is the reprojection of point $\boldsymbol{M}_j$ in image i. This non-linear minimization problem is solved with the Levenberg-Marquardt algorithm [86].

After this, five distortion coefficients (radial and tangential) [85], k_i, $i = 1, 2, ..., 5$ are calculated. These will modify the reprojection point $\check{\boldsymbol{m}}$ which will need to be recalculated taking into account these coefficients. Finally, the complete maximum likelihood estimation is given by:

$$\sum_{i=1}^{n}\sum_{j=1}^{m} ||\boldsymbol{m}_{ij} - \check{\boldsymbol{m}}\left(\mathbf{A}, k_1, k_2, k_3, k_4, k_5, \mathbf{R}_i, \boldsymbol{t}_i, \boldsymbol{M}_j\right)||^2. \tag{4.10}$$

4.2.3 Degenerate configurations and the error performance

Since (4.3) and (4.4) are derived from the properties of the rotation matrix, if $\mathbf{R}_2$ is not independent of $\mathbf{R}_1$, then image 2 does not provide additional constraints. In particular, if a plane undergoes a pure translation, then $\mathbf{R}_2 = \mathbf{R}_1$ and image 2 is not helpful for camera calibration.

Zhang [6] also provides an experimental study of the error performance of the intrinsic parameters depending on: a) noise level, b) number of planes and c) orientation of the model plane. Average results are shown in Figure 4.5.

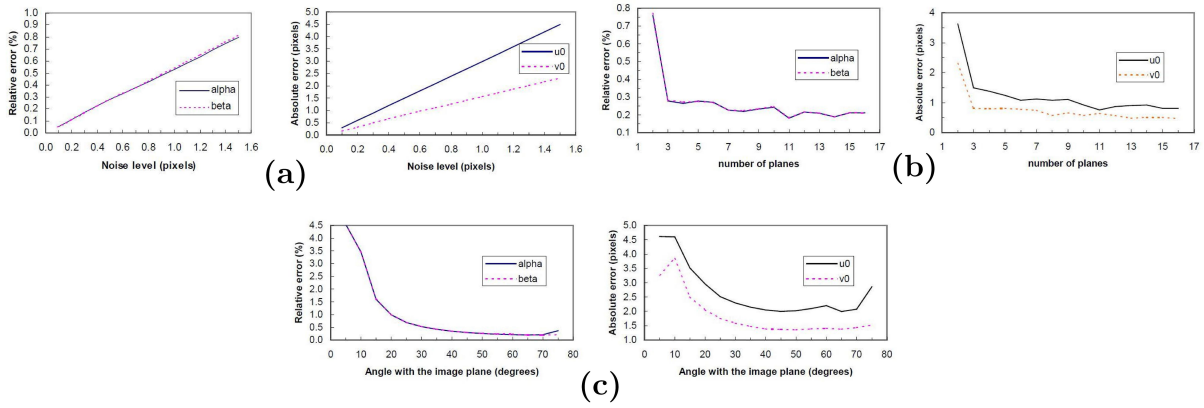

Figure 4.5: Error performance vs: (a) noise level, (b) number of planes and (c) angle with the image plane. Fig. extracted from [6].

In general, errors increase linearly with noise level, and decrease when more images are used, best performance seems to achieved with an angle around 45°, since with small angles close to being paralell to the camera plane the algorithm fails and with high angles close to being orthogonal to the camera plane, foreshortening makes the corner detection less precise.

4.3 Accuracy study (trueness and precision)

In order to implement a measurement system, it is necessary for it to have enough accuracy for the application. For this reason, it is necessary to perform an accuracy study of the

photogrammetric system (camera and planar patterns) in order to demonstrate that it is suitable for the current aplication.

The standard ISO 5725 [87] uses two terms "trueness" and "precision" to describe the accuracy of a measurement system. **Trueness** refers to the closeness of agreement between the arithmetic mean of a large number of test results and the true or accepted reference value. **Precision** refers to the closeness of agreement between test results.

The need to consider "accuracy" arises because tests performed on presumably identical materials and presumably identical circumstances do not, in general, yield to identical results. Many different factors may contribute to the variability of results of a measurement system, including:

- operator,
- equipment used,
- equipment calibration,
- environment (temperature, humidity, air pollution, etc.),
- time elapsed between measurements.

The variability between measurements performed by different operators and/or with different equipment will usually be greater than the variability between measurements carried out by a single operator using the same equipment.

4.3.1 Trueness

The "trueness" of a measurement system is of interest when it is possible to obtain a true value for the property being measured. The trueness of the measurement method can be investigated by comparing the accepted reference value with the resulting data given by the measurement system. Trueness is usually expressed in terms of bias or systematic error.

The experimental setup for the accuracy study was composed of the planar pattern under 3D known movements of 0.2 mm and 0.5 mm at a distance of 65 cm from the camera with controlled lighting, see Figure 4.6.

The movements were performed by a 3-axis microblock stage MBT16D, as shown in the Figure 4.7, with 1 μ of resolution. The experiment covered a 3-dimensional space of 0.6 mm and 1.5 mm in each axis for the displacements of 0.2 mm and 0.5 mm respectively.

The bias of the experimental results were calculated as the absolute error by:

$$E = |x_e - x_r|, \tag{4.11}$$

where E is the absolute error, x_e is the measurement obtained experimentally and x_r is the reference value. In this study, the experimetal measurement is the one obtained by the

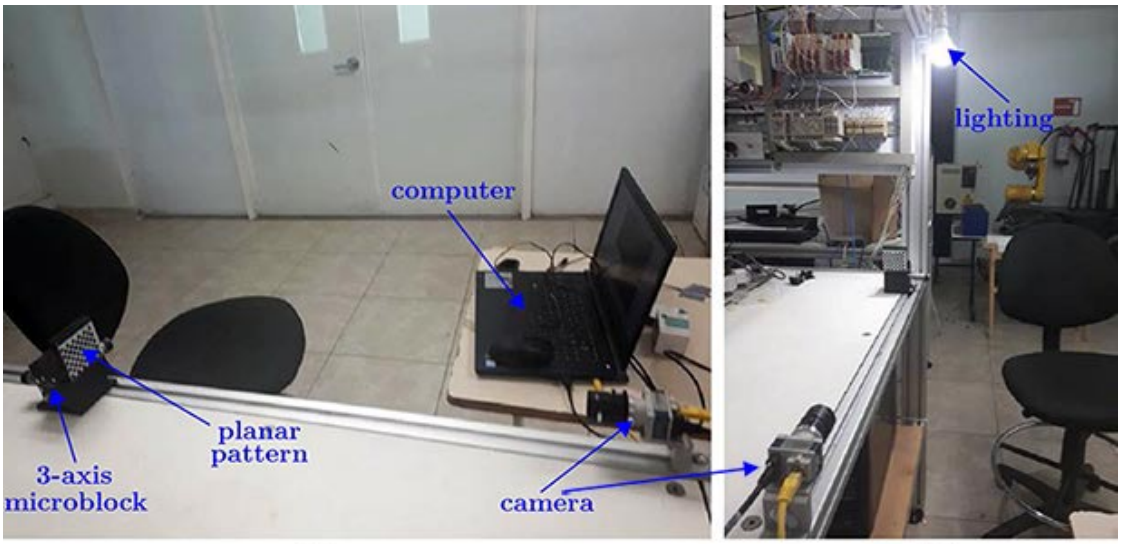

Figure 4.6: Experimental setup for the accuracy study; (a) first view (basic elements) and (b) second view (lighting).

Figure 4.7: 3-axis microblock stage MBT16D.

camera's images and the reference value is the one given by the microblock. In addition, the standard deviation of the error was also calculated as follows:

$$s = \sqrt{\frac{1}{(n-1)} \sum_{i=1}^{n} \left(E_i - \bar{E}\right)^2}, \tag{4.12}$$

where n is the number of test results, E_i is the absolute error of each result and $\bar{E}$ is the average error of the experiment.

The minimum and maximum errors are listed in the Table 4.1. Note that the minimum error occurs when the planar pattern is displaced on a plane paralell to the camera plane, and the maximum error when the planar pattern is displaced perpendicular to the camera

plane.

Table 4.1: Minimum and maximum errors at 65 cm.

Direction	Displacement	Error (mm)	s (mm)
Paralell	0.2 mm	0.0053466	0.0018208
	0.5 mm	0.0037446	0.0019758
Perpendicular	0.2 mm	0.0236775	0.0216883
	0.5 mm	0.0163387	0.0157000

The same experiment was performed at distances from 50 cm to 80 cm every 10 cm obtaining no significant changes in the error performance. For more details see **appendix A**.

4.3.2 Precision (repeatability and reproducibility)

In a perfect world, if the same material is repeatedly tested using the same test method, whether by the same operator in the same laboratory using the same apparatus or by different laboratories and operators using different apparatus meeting the specified requirements, all measurements generated will be numerically identical. However, we do not live in a perfect world. Repeated execution of the same method will not always yield to numerically identical results. Minor differences will exist between test results due to variations in factors that are inherent of the test method.

The general term for variability between repeated measurements is precision. Two conditions of precision, termed repeatability and reproducibility, have been found necessary and, for many practical cases, useful for describing the variability of a measurement system. The repeatability and reproducibility are standardized terms adopted by ASTM [88] and other standardization organizations. These are usually given in terms of standard deviations.

A nonstatistical interpretation of these values is that these are the maximum differences between two results obtained under specified conditions that can be attributed to the test method precision.

Repeatability concerns the variability between independent test results obtained by a single operator in the shortest practical period of time. **Reproducibility** deals with the variability between test results obtained by different operators.

The precision study consisted in the same experiment explained in the previous section executed by three different operators three times each.

The standard deviations of the repeatability, s_r, and reproducibility, s_R, were computed based in the norm ASTM 691 [89], as follows:

$$s_r = \sqrt{\frac{1}{p}\sum_{i=1}^{p} {s_i}^2}, \tag{4.13}$$

and

$$s_R = \sqrt{(s_{\bar{x}})^2 + \frac{1}{n}(s_r)^2(n-1)}, \tag{4.14}$$

where:

$$\begin{aligned} p &= \text{number of operators,} \\ s_i &= \text{standard deviation of the test performed by each operator,} \\ s_{\bar{x}} &= \text{standard deviation of the three test averages,} \\ n &= \text{number of results in each test.} \end{aligned}$$

The final standard deviations of the repeatability and reproducibility computed by (4.13) and (4.14) are listed in the Table 4.2.

Table 4.2: Standard deviations of the repeatability and reproducibility.

Repeatability	Reproducibility
0.00867326	0.00833351

4.3.3 Discussion

Reviewing the results of the accuracy study listed in Tables 4.1, A.1 and 4.2, it is possible to conclude that the proposed measurement system has the accuracy necessary to be used for the determination of the knee workspace. In addition, three basic recommendations are listed below in order to improve the experimental results:

- Avoid important displacements in the perpendicular direction to the camera plane.
- Make a robust camera calibration procedure with a high number of images and orientations of the planar pattern.
- Perform the experiment in the same conditions for a short period of time.

Chapter 5

Experimental procedure

In this chapter, the experimental procedure through materials and methods is described and presented in great detail with the purpose that other persons will be able to reproduce the experiment. After that, the knee work-spaces and the joint parameters are determined for each subject during specific motion tasks in a deep kinematic approach and comparisons between them and the reported in the literature were made.

5.1 Data acquisition system

The camera used and the description of the measurement system for taking 3D coordinates from an image camera is given in **Chapter 4**. This chapter focused in the general description of the data adquisition system for the experimental procedure.

The process consists on taking a series of images of the knee under specific motion tasks. Two planar patterns have to be attached to the thigh and shank respectively and the camera needs to see both patterns during the complete motion tasks as is shown in Figure 5.1.

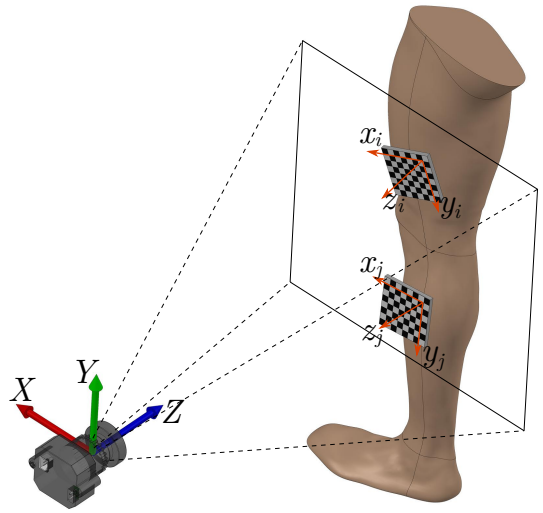

Figure 5.1: Image plane and attachement of the planar patterns on the leg.

The process of taking images has been implemented in Matlab® with a graphical user interface GUI described below.

5.1.1 Graphical user interface (GUI)

The graphical user interface developed for the automation of the data acquisition procedure is shown in Figure 5.2.

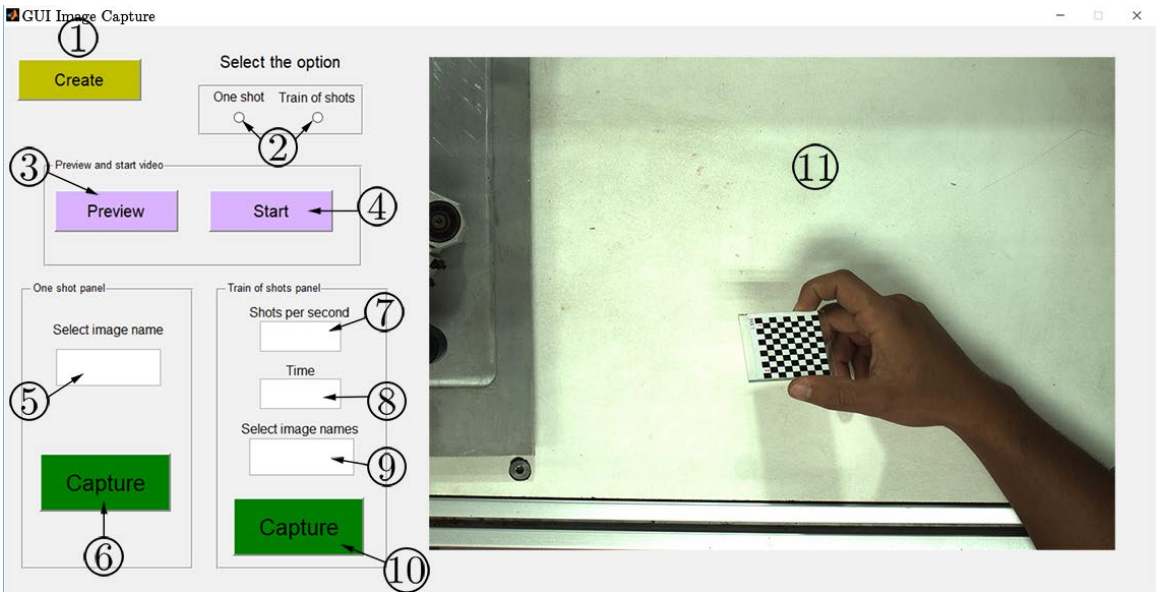

Figure 5.2: Elements of the graphical user interface "Image Capture".

Hereafter the description of the GUI elements is presented:

1. **Create Button**: create a video object and set the camera configurations needed, such as; trigger, packet size and exposure time.

2. **Radio buttons for One shot and Train of shots**: select one of the two options of the GUI: take one shot or a train of shots (One shot is used for the calibration procedure and train of shots for the experiment).

3. **Preview Button**: before starting the recording, the preview can be selected where it is shown the camera image to make the necessary adjustments as focus or gain.

4. **Start Button**: starts the video recording.

5. **Edit text Image name**: in one shot mode it is necessary to write the complete name of each image.

6. **Capture Button**: button to capture an image in one shot mode.

7. **Edit text Shots per second**: the frecuency of capturing images in train of shots mode is given in shots per second. It is necessary to write the number of shots per second.

8. **Edit text Time**: it is the time lapse of the capturing process in train of shots mode.
9. **Edit text Image names**: in train of shots mode it is necessary to write the base name of the images. The addition to this base name will be set by the program with the corresponding number using an incremental counter.
10. **Capture Button**: button to start the train in train of shots mode.
11. **Axes**: an axes element for displaying the captured images.

5.1.2 Camera calibration

The process for camera calibration by the camera calibration toolbox for Matlab® is described in detail in **Appendix B**. The results of the intrinsic parameters after the calibration procedure are shown in Table 5.1.

Table 5.1: Intrinsic parameters of the camera.

Parameter	**Results**
Focal length	[3551.16357 3558.82589] ±[26.69099 31.58028]
Principal point	[1162.69165 760.75329] ±[50.75213 39.01203]
Skew	90.0000 + 0000
Distortion	[-0.14252 0.41300 0.00852 0.01239] ± [0.02843 0.35874 0.00336 0.00357]
Pixel error	[0.08896 0.06552]

5.2 Tracking system

The tracking system is composed by the planar patterns but these must be attached to the thigh and shank by some kind of mechanical system that avoids the relative movement of the pattern with respect to the body segment. The description of this mechanical system is presented below.

From section **1.1.1**, one of the basic recommendations given in the literature was the use of elastic bands to rigidity the skin. Moreover, place the markers in the first third of the thigh and in the mid of the shank.

The planar patterns are placed on rigid elements made in a 3D printer, designed specifically for the current application. These elements were based on the subject specific thigh and shank dimentions. The CAD model and the final rigid element are shown in Figure 5.3.

The rigid elements have openings to hold them by straps and attach them to the thigh and shank on the surfaces covered by the elastic bands. The final tracking system (elastic bands, straps with rigid elements and planar patterns) is shown in Figure 5.4.

The straps are placed to about 12 *cm* from the lateral femoral condyle for the thigh and about 15 *cm* from the lateral femoral condyle for the shank, with the patterns parallel to the lateral face of the left leg.

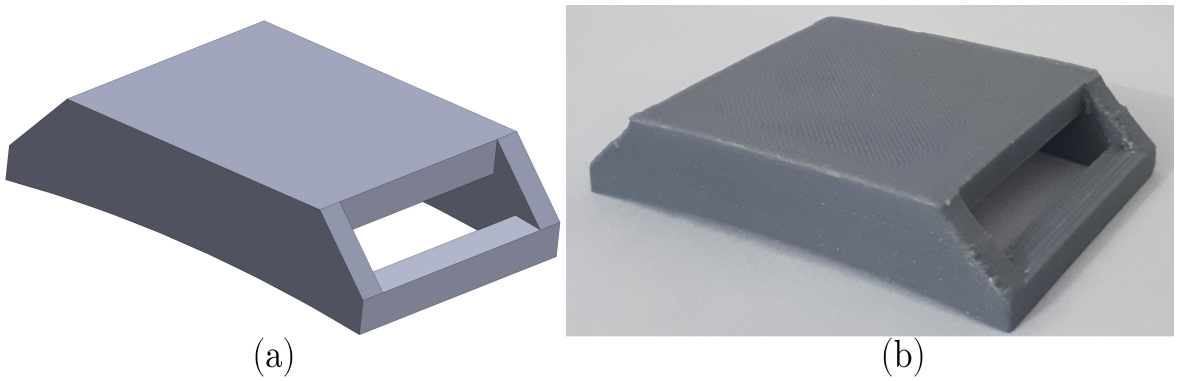

Figure 5.3: Rigid elements of the tracking system; (a) CAD model and (b) 3D printed element.

Figure 5.4: Final tracking system on the left leg of a volunteer.

5.3 Experimental setup

The experiment was performed at a distance of about 65 *cm* to the camera from the patterns with an image taking frequency of 10 shots per second in a time lapse of 6 seconds for each motion task.

The complete experimental setup is shown in Figure 5.5.

5.3.1 Volunteers

The experiment was performed in three volunters able-bodies young males with no history of knee musculoskeletal injury on their left legs. The personal data of these volunteers is presented in the Table 5.2.

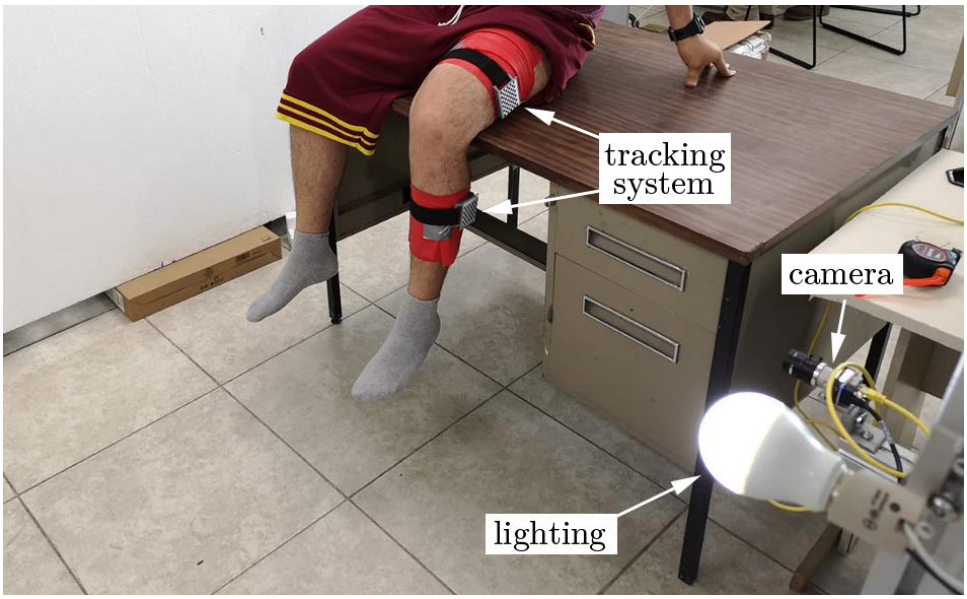

Figure 5.5: Experimental setup of the experiment.

Table 5.2: Personal data of the Volunteers.

	Volunteer 1	**Volunteer 2**	**Volunteer 3**
Age (years)	25	26	27
height (cm)	176	178	174
weight (kg)	91	81	77

5.3.2 Motion tasks

A total of three motion tasks (MT) were performed in the left leg of each volunteer, two of them assisted ensuring total passive movement and the other carried out by the volunteer himself in semi-active fashion. Images of the MT are shown in Figure 5.6. The description of these MT all from the physiological fundamentals of the chapter, are given below.

Assisted passive MT1, Figure 5.6(a), is based in flexion-extension rotation. The MT starts with the volunteer sitting with the knee close to a right angle then the examiner takes the ankle and carries it up until the full extension.

Assisted passive MT2, Figure 5.6(b), is based in internal-external rotation. This MT is performed with the volunteer standing with the knee flexed at a right angle. The examiner grasps the foot with both hands and rotates it until the toes face laterally and medially.

Semi-active MT3, Figure 5.6(c), is based in flexion-extension rotation. The volunteer is standing with the knee in full extension he then flexes the knee maintaining the thigh at the initial position during all the MT.

5.4 Results

For all the experiments lets call T^A to the 3D coordinate system given by the pattern in the thigh and the system T^B to the coordinate system in the shank. Then all the results

(a) (b) (c)

Figure 5.6: Motion tasks; (a) MT1, (b) MT2 (passive), and (c) MT3 (semi-active).

are based on the movements of the system T^B with respect to the system T^A. Lets name the work-space to all the poses of T^B relative to T^A for each MT.

The work-spaces have the representation in the 3D space as the given in the Figure 5.7.

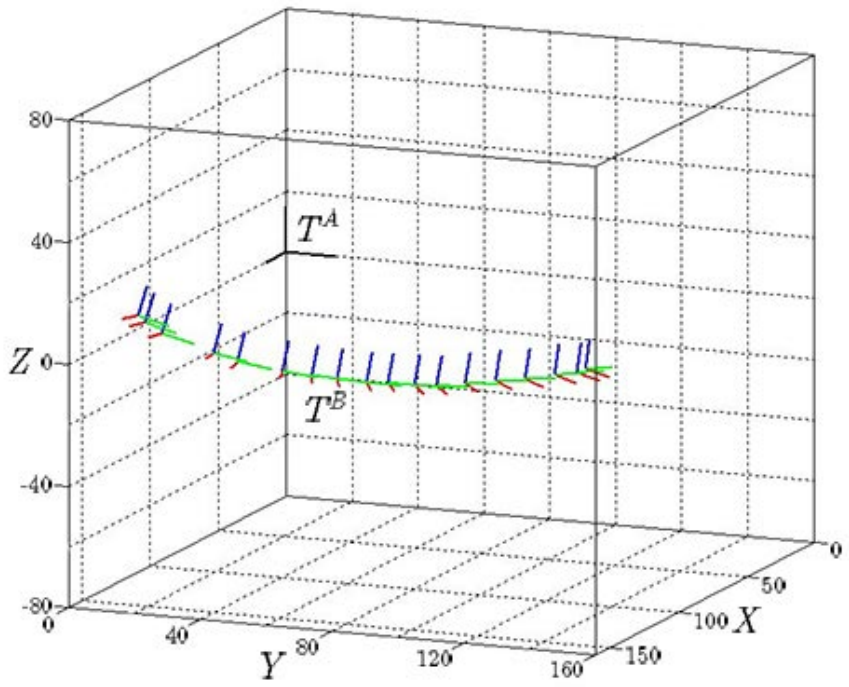

Figure 5.7: Work-space of the system T^B relative to T^A. Lines of the system T^B have the meanings: red (x axis), green (y axis) and blue (z axis).

With these 3D work-spaces we can make different types of analysis depending on the motion task, using the mathematic and kinematic tools viewed in **Chapter 3**.

5.4.1 Motion task 1

Since this is a passive motion task based in flexion-extension rotation, it allows us to examinate the displacements, rotations and the general behavior of the knee in the sagittal plane.

The process to analyze this MT is shown in Figure 5.8. First, the equivalent sagittal plane which is the best fit plane to the origins of the systems T^B is obtained, see Figure 5.8(b). After this, the origins are projected on this plane and a new coordinate system is defined with two of its axes lying on this plane, see Figure 5.8(c).

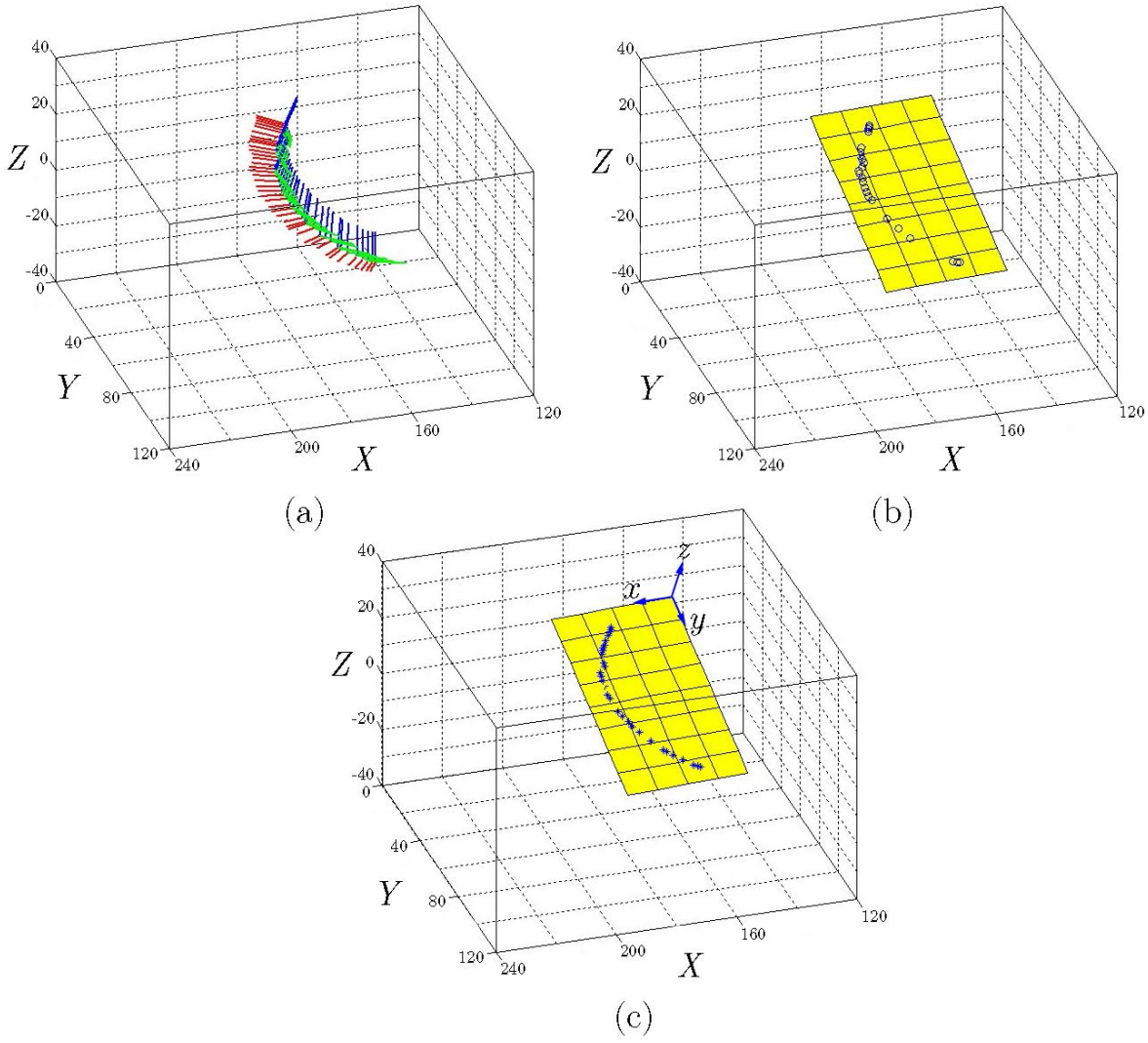

Figure 5.8: Process to analyze the MT1; (a) 3D work-space, (b) plane that best fit the origins of T^B and (c) projected points on the plane and the new coordinate system.

The curves obtained by the projected origins of the three volunteers during the analysis of the MT1 are plottled in the Figure 5.9, in (a), (b) and (c) respectively. In these plots the difference between phases during the MT can be observed, separated by different colors.

The blue part of the curve corresponds to the first 20° of the flexion from full extension

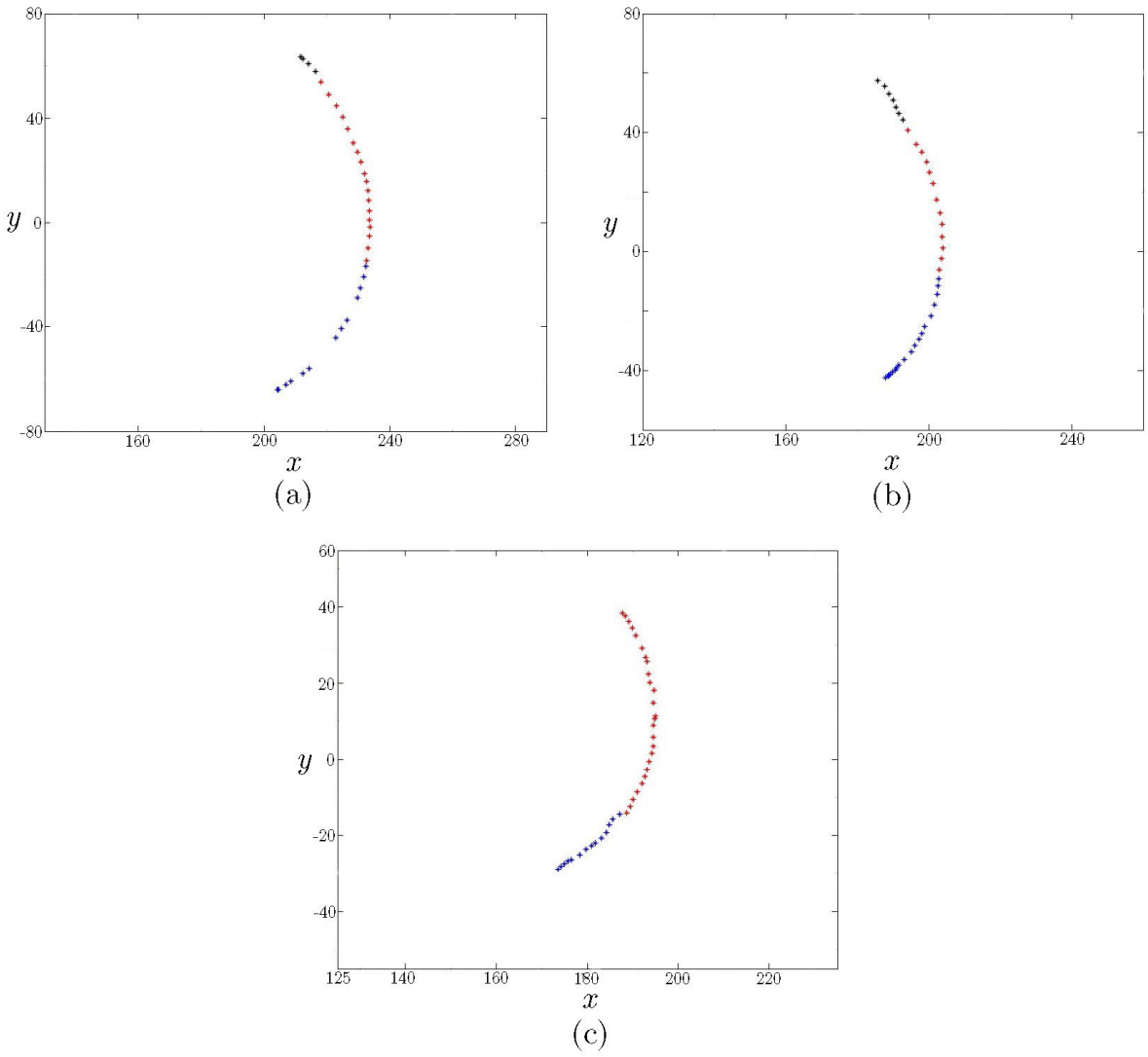

Figure 5.9: Curves given by the origins in the sagittal plane during MT1; (a) volunteer 1, (b) volunteer 2 and (c) volunteer 3.

position is the phase where only rolling takes place. The red part of the curve corresponds to the rolling and sliding phase that occurs during the next 30°. Aditionally, in the curves of the volunteers 1 and 2, a little black part can be observed which can be attributed to the predominance of the sliding over the rolling. For more details about the rolling-sliding process of the knee joint during the flexion, see **Chapter 2** and [67].

To measure only the sliding of the tibia relative to the femur during the blue and red phases, the circle that best fits all the data must remain constant during the analysis. The circle that best fits blue and red curves at the same time is shown in Figure 5.10(a). The circle obtained previously by fitting the blue and the red parts of the curve separately are shown in Figure 5.10(b). The distance between the centers can be related directly with the sliding of the knee joint during the first 50° of flexion. The computed distances between the centers of the three volunteers are presented in the Table 5.3.

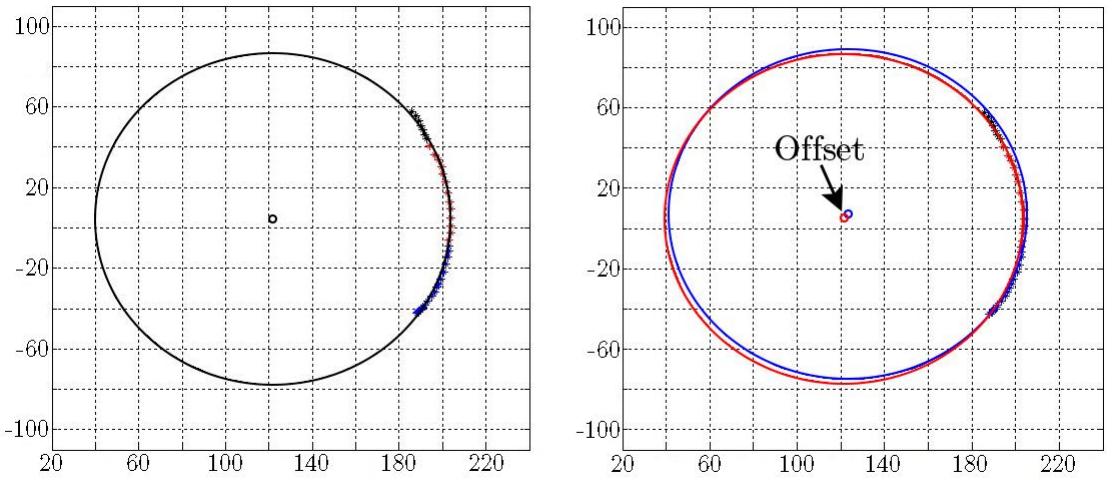

Figure 5.10: (a) Circle that best fits the blue and red parts of the curve at the same time and (b) the same circle with constant radius fitting the blue and red parts of the curve separately.

Table 5.3: Distance between the centers for the three volunteers during MT1.

	Volunteer 1	**Volunteer 2**	**Volunteer 3**
Distance (mm)	2.7948	2.6681	2.3159

These results agree with the reported in the literature [90] in which the authors reported displacements between 1 and 4 mm during the first 55° of flexion-extension rotation.

5.4.2 Motion task 2

This motion task allows to measure the internal-external rotation which occur in the transverse plane of the knee. The data of this MT is separated in two rotations: internal and external rotations both starting from the neutral position with the toes in line perpendicular to the floor.

The process to analyze this MT is shown in Figure 5.11. First, the Rodrigues's vector of each rotation matrix of T^B relative to T^A is obtained, see Figure 5.11(b). Therefore, the angle of the Rodrigues's vector $i+1$, with respect to i is computed by means of the dot product.

The graphics of the angle variation during the external and internal rotations for each volunteer are shown in Figure 5.12. The maximum angles reached for internal-external rotations of the three volunteers are presented in the table 5.4.

These results agree with the reported in the literature [91] which reports a range of passive external-internal rotation with the knee flexed at 90° of about $25 - 35°$.

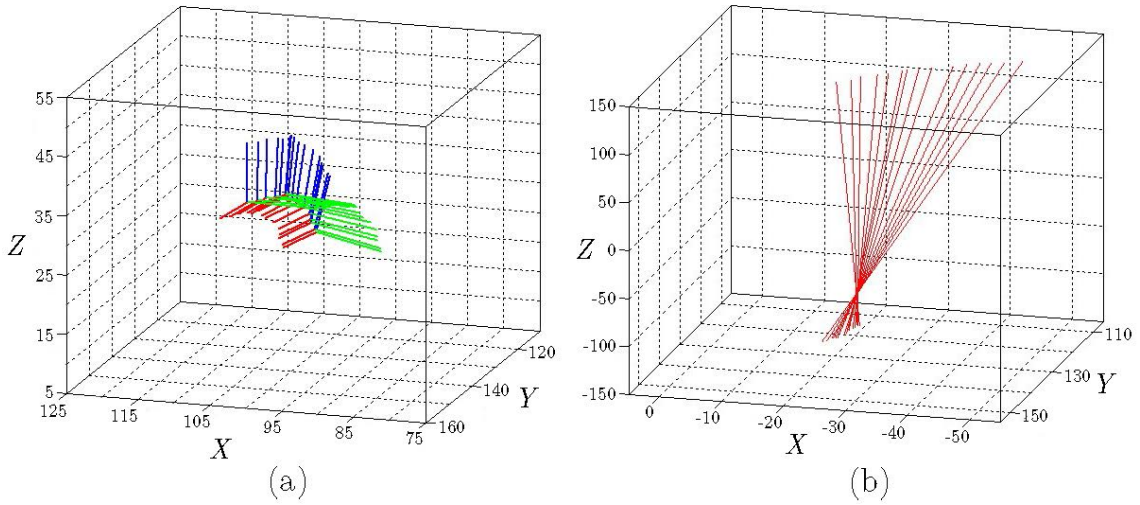

Figure 5.11: Process to analyze the MT2; (a) 3D work-space and (b) the Rodrigues's vectors of the rotation matrices of each coordinate system T^B relative to T^A.

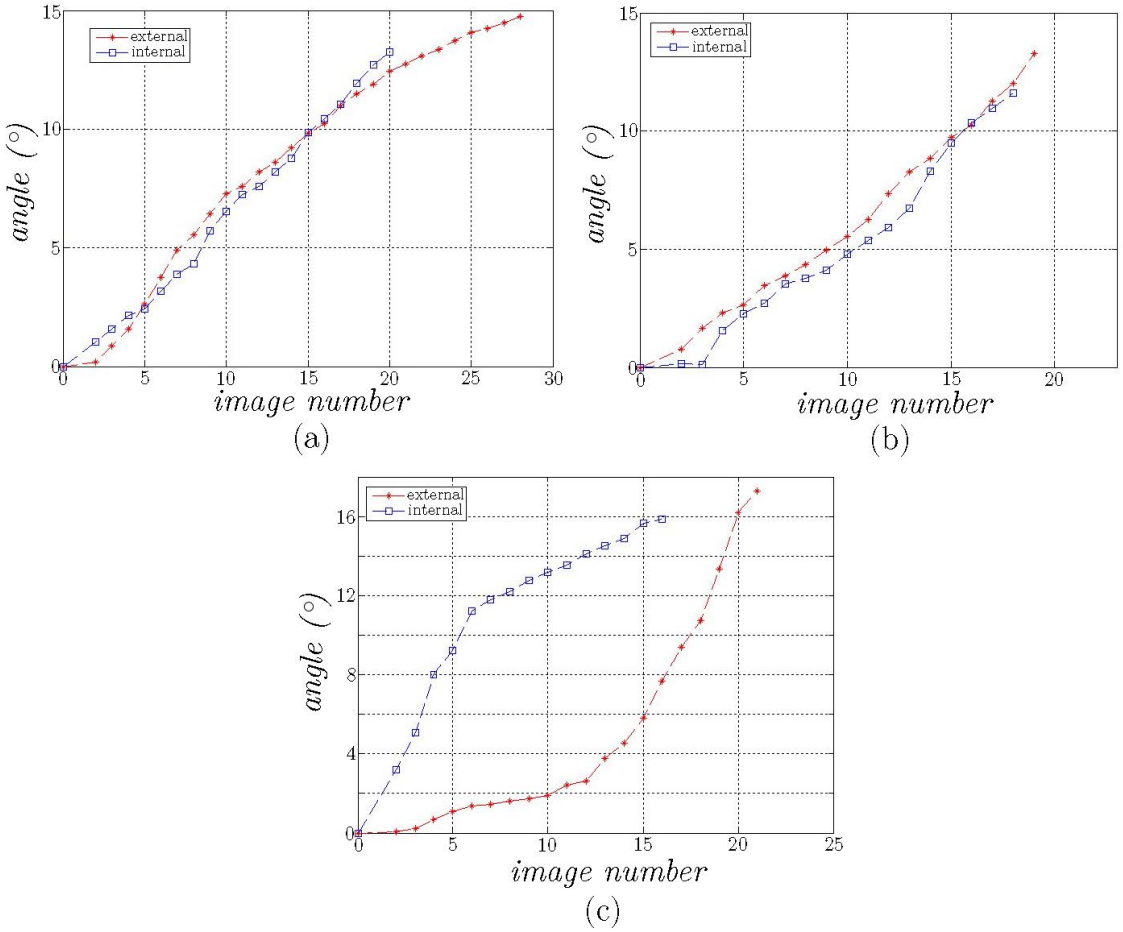

Figure 5.12: Angle variation during the external-internal rotation of the knee; (a) volunteer 1 (b) volunteer 2 and (c) volunteer 3.

Table 5.4: Maximum angle during internal-external rotation and the complete rotation angle for the three volunteers.

	Volunteer 1	**Volunteer 2**	**Volunteer 3**
External (°)	14.7427	13.2678	17.2955
Internal (°)	13.2460	11.5991	15.8582
Complete rotation (°)	27.9887	24.8669	33.1537

5.4.3 Motion task 3

The MT3 is a semi-active flexion rotation that allows the analysis of the automatic internal-external rotation of the knee during the flexion-extension rotation. Moreover, as the midpoint between the passive and the active motions, this MT enables a good evaluation of the knee models to reach the work-space.

The process to analyze this MT is shown in Figure 5.13. First, let's compute the best fit sphere to the origins, see Figure 5.13(b), of the coordinate systems T^B relative to T^A as shown in Figure 5.13(c).

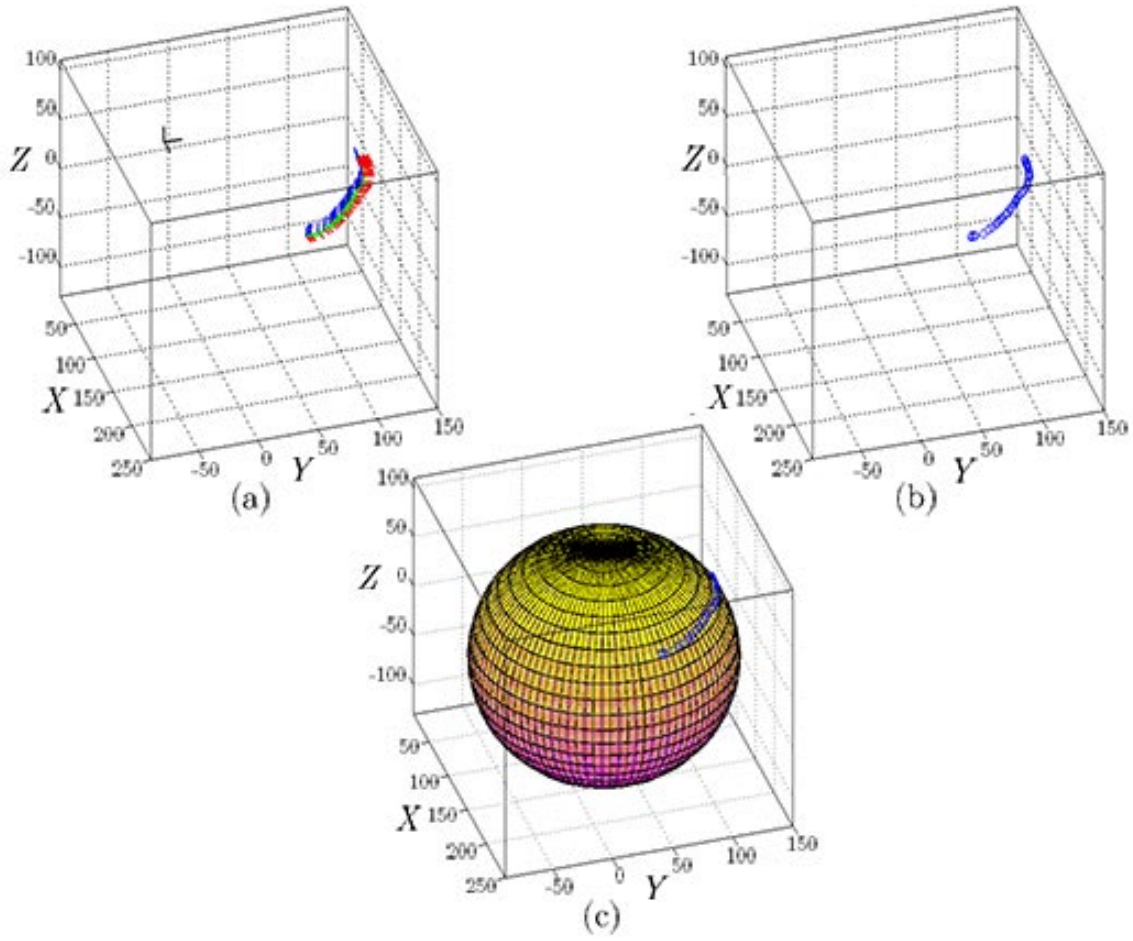

Figure 5.13: Process to compute best fit sphere during MT3; (a) 3D work-space (b) set of origins of the coordinate system T^B relative to T^A and (c) best fit sphere to the data points.

After this, the error can be observed by comparing the difference between the sphere radius and the distance from the center of the sphere and the data point, the error performance for the three volunteers is shown in Figure 5.14.

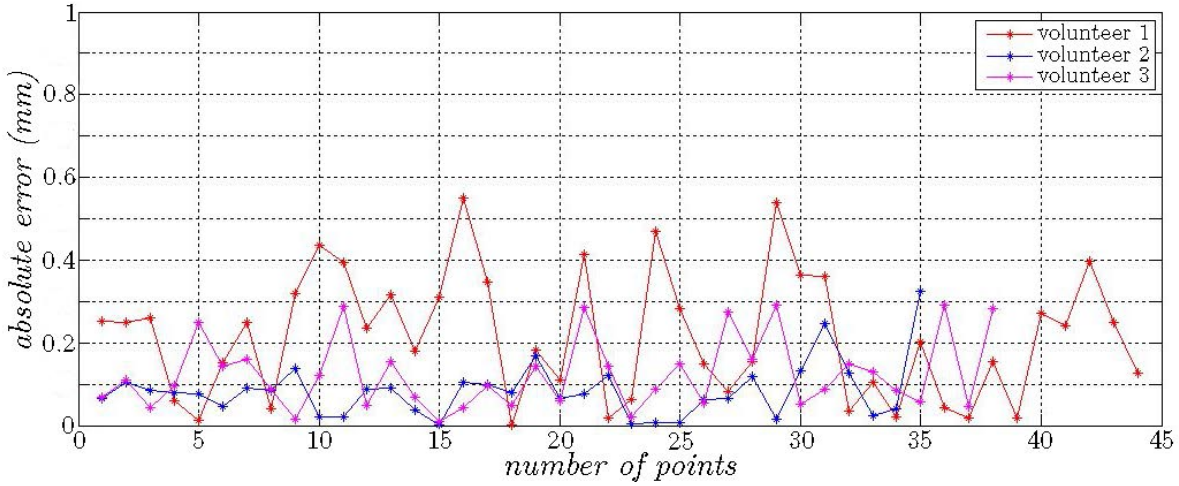

Figure 5.14: absolute error performance between the radius of the best fit sphere and the distance from the sphere center and the data point, for the three volunteers.

As it can be seen, the mean error is in most cases les than 0.4 mm which is the reason that the spherical pair is the most commonly used for MKO in gait analysis as is reported in [32–34]. The parameters of the computed sphere in the MT3 for each volunteer are presented in the table 5.5.

Table 5.5: Parameters (coordinates of the center and length of the radius) of the best fit spheres to the data points of each volunteer during MT3.

	Volunteer 1	**Volunteer 2**	**Volunteer 3**
Center (mm)	$x = 111.2118$ $y = 35.8569$ $z = -28.4148$	$x = 139.8033$ $y = 34.5991$ $z = -42.4219$	$x = 113.7497$ $y = 46.0845$ $z = 67.6065$
Radius (mm)	108.4853	141.0031	77.5915

Now, lets analyze the automatic rotation of the knee by means of the screw lines. First, the screw line of each displacement of the coordinate system T^B relative to T^A is computed, ${}^A\mathbf{T}^B$ from the position i to $i+1$ with the equations (3.46) and (3.41). The work-space of the MT3 of the volunteer 2 is shown in Figure 5.15(a), and the screw lines of each relative displacement are shown in Figure 5.15(b).

The screw lines have the advantage that they are independent of the configuration of the coordinate systems, instead, they depend on the displacements only. Other important statement is that the screw lines are not the flexion-extension axes but they are the axes of the entire knee motion, rotations and translations together. Since the principal movement of the knee is the flexion-extension rotation, these screw lines have axes that are quite similar to the flexion-extension axis. It is possible to examine these variations

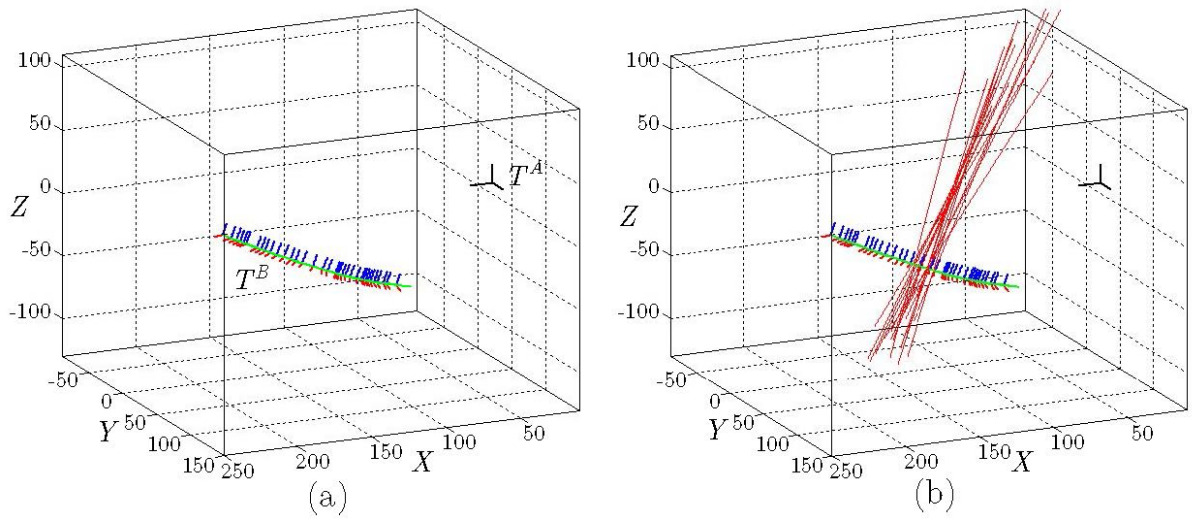

Figure 5.15: Process to compute the screw lines during the MT3; (a) 3D work-space and (b) screw lines of the relative displacements of coordinate system T^B relative to T^A, ${}^A\mathbf{T}^B$.

by computing the angle between the screw axes and the flexion-extension axis obtained by the process described in Figure 5.16. The work-space of the MT3 for the volunteer 2 is shown in the Figure 5.16(a). The flexion-extension axis is the orthogonal vector to the plane that best fits the set of origins as is shown in the Figures 5.16(b) and (c).

In Figure 5.17 the projection of the screw axes onto the flexion-extension axis by means of the dot product during the MT3 is shown, for each volunteer. The closer the projection is to 1 the more parallel are the screw axis and the flexion-extension axis. This graphic shows the influence of the automatic internal-external rotation during the flexio-extension rotation in a semi-active MT and could be considered as a parameter of the behavior of a healthy knee.

As a summary of this chapter, the parameters obtained during the experimental procedure shown agreement with the reported in the literature. Moreover, the experimental procedure is independent of the pattern placement and the measurement system is easy to implement, which suggest that it can be used as an assistant tool for diagnostic of pathologies.

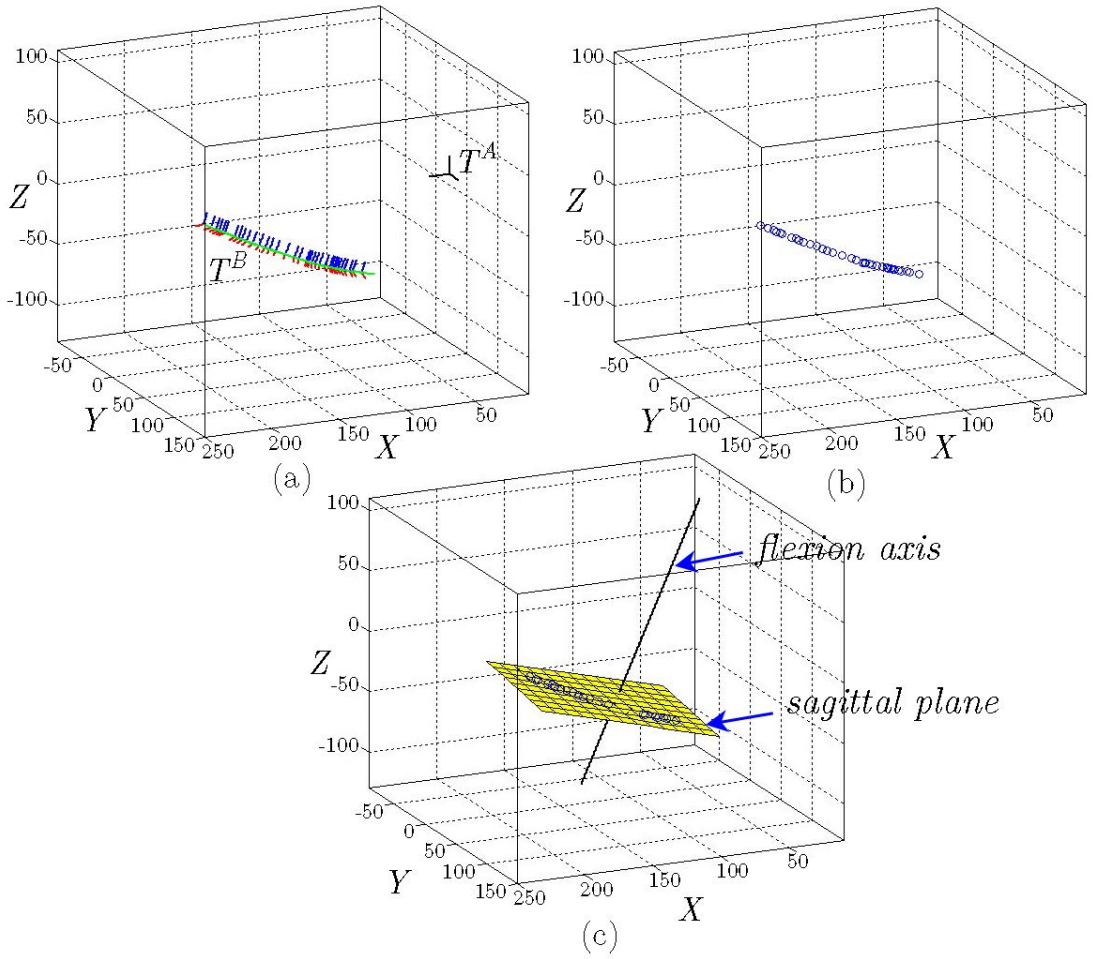

Figure 5.16: Process to compute the flexion-extension axis during MT3; (a) 3D work-space, (b) set of origins of the coordinate system T^B relative to T^A and (c) line whose axis is orthogonal to the plane that best fits the set of points, passing through it.

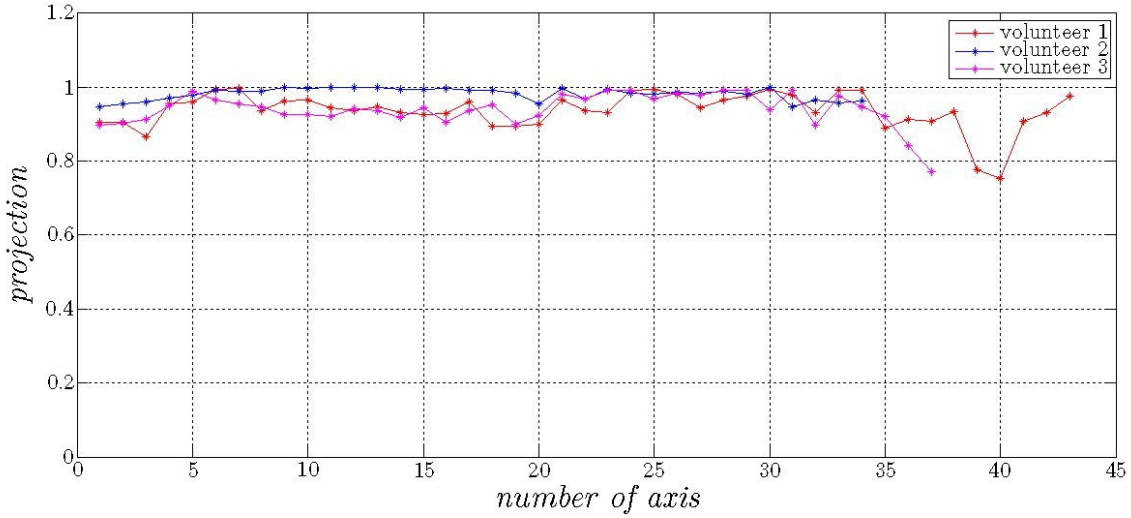

Figure 5.17: Projection of the screw axes onto the flexion-extension axis of the three volunteer during the MT3.

Chapter 6

Synthesis of the kinematic knee model

In this chapter, the synthesis of the kinematic knee model of a left knee proposed through its anatomical, physiological and kinematical bases is presented, as well as a validation of the model by reaching a subject specific knee work-space during flexion task, experimentally obtained and presented in the **chapter 5**. In addition, an adjustment process of the length variations of the equivalent kinematic ligament chains with some ligament length variation curves from the literature is presented as proof that the proposed kinematic knee model is capable to simulate prescribed ligament length variations while it is reaching a flexion work-space.

Along this chapter we will call kinematic knee model to the obtained mechanism by the synthesis of the tibio-femoral joint, since the patella is not taken into account in the present study.

6.1 Kinematic knee model: anatomical and physiological approach

The kinematic knee model must have the highest possible anatomical significance while maintaining its simple kinematical approach, and modeling the anatomical passive structures; condyles, cruciate ligaments and colateral ligaments, at the same time.

6.1.1 Tibia and femur condyles

In [3] it was demostrated that the substitution of lower-order surfaces with more complex ones did not produce particular benefits; on the contrary, the use of b-splines brought computational and optimization instabilities that resulted in worse results than those of simple models. The approximation of the femur articular surfaces with spheres proved to be very efficient for the tibio-femoral passive motion.

After this, the femur condyles are modeled as spheres with equal radii, see Figure 6.1(a), based on the study developed by Sintini et al. [61] in which the authors studied 20

cadaveric specimens, and differences of less than 1 mm between the radii of the equivalent medial and lateral spheres were found.

The condyles of the tibia are modeled as a simple plane, see Figure 6.1(b), in order to facilitate further kinematic analysis and provide a simple way to measure the sliding of the femur on the tibia.

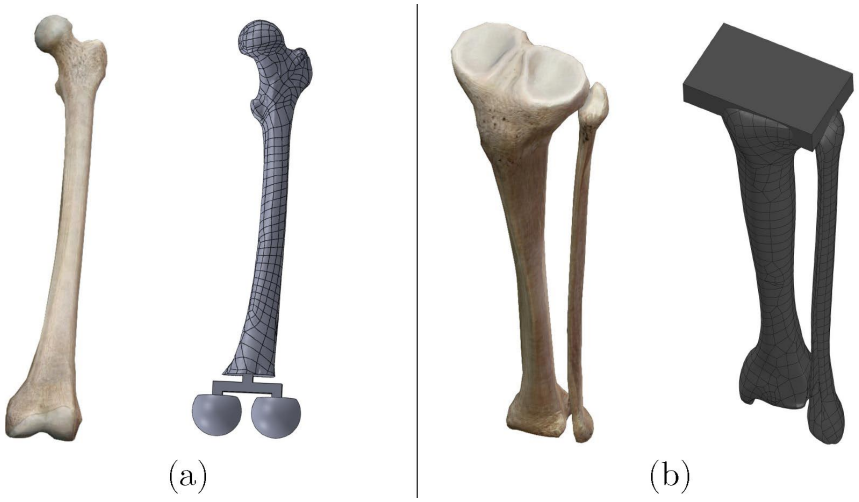

Figure 6.1: Digital bones and kinematical models of the condyles; (a) femur and (b) tibia.

The spheres's radii and the separation between the spheres's centers were based in the literature [61, 66, 92], the radius is $r = 25\ mm$ and the separation has a length of 60 mm.

Lets define the two coordinate systems attached to the femur and tibia as T^f and T^t, respectively as is shown in Figure 6.2. The origin of the femur coordinate system (FCS), o^f is located between the spheres on a plane paralell to the tibia-plane at a distance of the spheres diameter, see Figure 6.2. The orientation of the FCS is based on the recomendations given by Grood and Suntay [38]. The x^f axis is in perpendicular direction to the coronal plane, y^f axis is parallel to the gravity field direction in a standing leg during full extension and the z^f axis is defined perpendicular to both x^f and y^f axes. The origin of the tibia coordinate system (TCS), o^t is located on the tibia plane just below the origin of the FCS. The axes of the TCS have the same direction as the FCS axes when the knee model is in full extension, see Figure 6.2.

The coordinates of the origins o^t and o^f relative to FCS and TFS, as well as the coordinates of the sphere centers, C_M C_L, and the contacts sphere-plane, D_M D_L, when the kinematic knee model is in full extension, are described in the Table 6.1.

Further experimental evidence proved that the tibio-femoral pose is not influenced by the patello-femoral joint during the knee motion, and the complete pose of the tibia relative to the femur can be completely described by the tibio-femoral joint, then: a tibio-femoral mechanism can be synthesized at first, that excludes the patella; the patello-femoral mechanism can be defined subsequently [4, 5, 59].

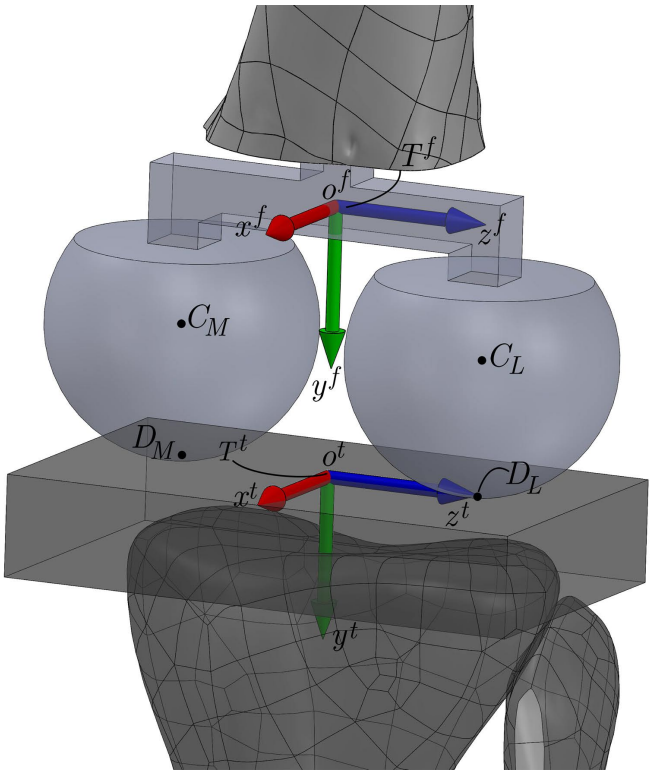

Figure 6.2: Kinematic model of the tibia and femur condyles in full extension and their corresponding coordinate systems, T^t and T^f.

Table 6.1: Coordinates of the origins o^f and o^t, sphere centers, C_M and C_L, and the sphere-plane contacts, D_M and D_L, relative to femur and tibia coordinate systems, T^f and T^t, during full extension of the kinematic knee model, (mm).

Point	**Coordinate system** (mm)					
	T^f			T^t		
o^f	0.0000	0.0000	0.0000	0.0000	-50.0000	0.0000
o^t	0.0000	50.0000	0.0000	0.0000	0.0000	0.0000
C_M	0.0000	25.0000	-30.0000	0.0000	-25.0000	-30.0000
C_L	0.0000	25.0000	30.0000	0.0000	-25.0000	30.0000
D_M	0.0000	50.0000	-30.0000	0.0000	0.0000	-30.0000
D_L	0.0000	50.0000	30.0000	0.0000	0.0000	30.0000

6.1.2 Cruciate and collateral ligaments

Studies [67,93,94] demostrated that the insertions of the ligaments specially the cruciates, can rotate around up to three perpendicular axes contributing to fibre recruitment during the knee motion. This statement allows to modelate the ligament insertions by spherical pairs.

The ligaments are viscoelastic anatomical structures with the main characteristic that their lengths vary tensing and slackening during knee motion. This length variation change the distance between the ligament insertions shortening it or lengthening it. This behaviour can be modelated by a prismatic pair.

Cruciate and collateral ligaments all have several important fibres or groups of fibres that have their particular length variation and insertion positions. In this work, all the ligaments are modeled as a single fibre by only one kinematic chain, to give a first approximation, but at the end of this chapter it will be easy to see that the presented procedure can be extended to any number of ligament fibres making the analysis as complete as desired.

After this, the cruciate and collateral ligaments are modeled by SPS (spherical-prismatic-spherical) kinematic chains as shown in Figure 6.3.

The cruciate ligaments, ACL and PCL as well as the collateral ligaments, MCL and LCL have important subject-specific variations both in their insertion positions and in their lengths during full extension. Averages of these anatomical characteristics of the knee were extracted from literature [7,95–97] to construct the kinematic knee model shown in Figure 6.3.

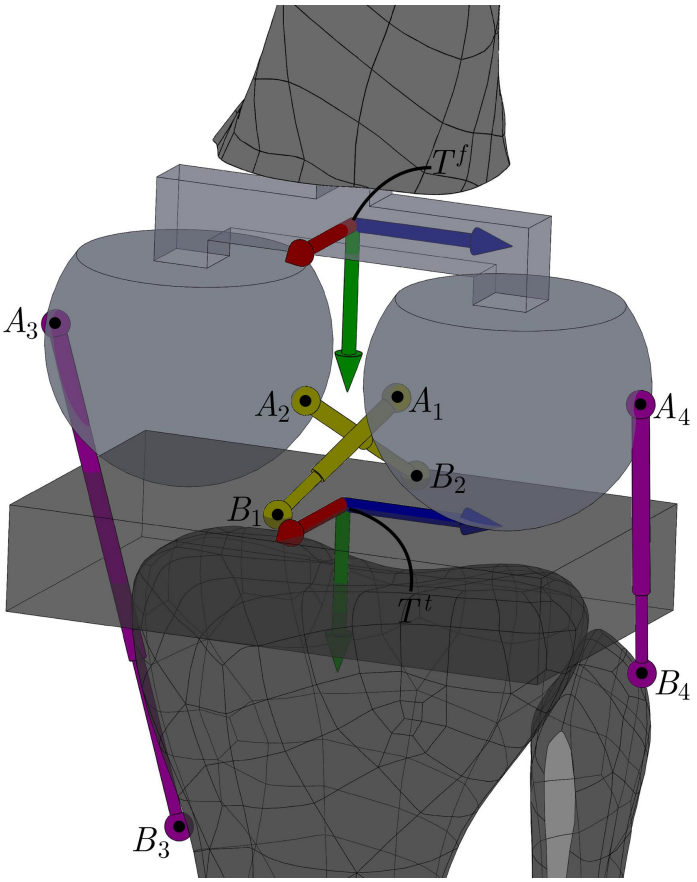

Figure 6.3: Kinematic model of the tibia and femur condyles with the ACL PCL, MCL and LCL ligaments modeled as SPS kinematic chains.

The lengths of the ligaments (SPS chains) and the coordinates of their insertion points, A_i, B_i $i = 1, ...4.$, in terms of the FCS and TCS during full extension, are presented in tables 6.2 and 6.3 respectively.

Table 6.2: Ligament lengths (ACL, PCL, MCL, LCL) of the kinematic knee model from Figure 6.3.

	ACL	**PCL**	**MCL**	**LCL**
Length (mm)	30	37	90	50

Table 6.3: Coordinates of the insertion points, A_i and B_i $i = 1, 2, 3, 4.$, of the kinematic knee model from Figure 6.3, (mm).

Ligament	**Insertion point**	**Coordinate system** T^f			T^t		
ACL	A_1	-7.4215	31.8355	6.1599	-7.4215	-18.1644	6.1599
	B_1	12.5000	50.0000	-7.0000	12.5000	0.0000	-7.0000
PCL	A_2	5.6028	30.9813	-5.4117	5.6028	-19.0186	-5.4117
	B_2	-25.0000	50.0000	3.0000	-25.0000	0.0000	3.0000
MCL	A_3	0.0000	25.0000	-55.0000	0.0000	-25.0000	-55.0000
	B_3	10.5656	114.0461	-47.3094	10.5656	64.0461	-47.3094
LCL	A_4	0.0000	25.0000	55.0000	0.0000	-25.0000	55.0000
	B_4	-14.4437	72.8653	55.5341	-14.4437	22.8653	55.5341

6.2 Kinematic knee model: kinematical approach

The model shown in the Figure 6.2 composed by the two spheres on a plane is a 4-DoF kinematic chain that allows sliding on the plane in the directions x^t and z^t, rotation around an axis parallel to z^f through the sphere centers, C_M and C_L, and rotation around the axis y^t perpendicular to the plane.

This 4-DoF model could be represented by an equivalent kinematic chain, RRPP as the one shown in the Figure 6.4, where distances d_1 and d_2 are equal to the sphere's radius.

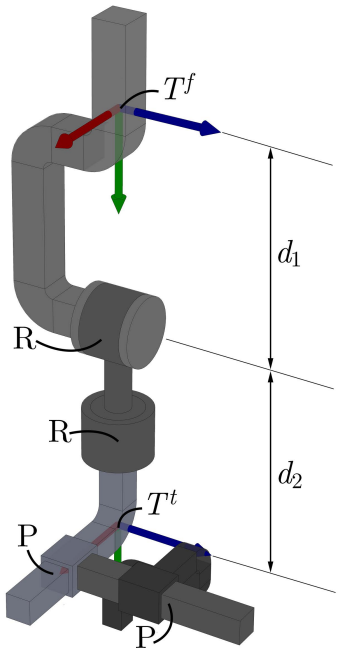

Figure 6.4: RRPP equivalent kinematic chain of the two spheres on plane model from Figure 6.2.

The ligament kinematic chains SPS are added to the RRPP main kinematic chain shown in the Figure 6.4, with the same features described in Tables 6.2 and 6.3. The complete equivalent mechanism as a RRPP+4-SPS parallel platform is shown in Figure 6.5.

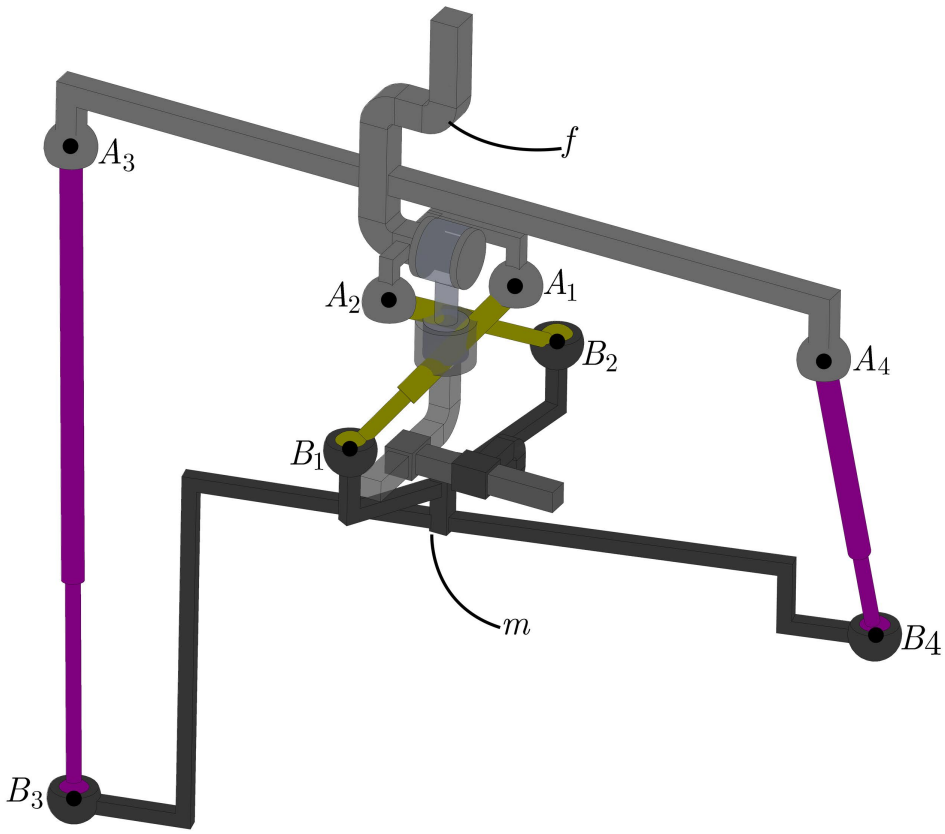

Figure 6.5: Equivalent RRPP+4-SPS parallel platform of the complete kinematic knee model including the ligaments.

6.2.1 Mobility of the complete parallel platform

The presented procedure to compute the mobility of the complete parallel platform shown in Figure 6.5, was based on the criterion developed by Rico et al. [98], for an in-depth treatment of the basic notions necessary to develop the criterion, readers are referred to [99–101].

Let's call the fixed platform f to the femur kinematic model and the moving platform m to the tibia kinematic model as shown in Figure 6.5.

The parallel platform is formed by five serial connecting chains. The first serial chain is formed by two revolute and two prismatic pairs. The other four chains are formed by a prismatic pair and two spherical pairs, the kinematic pairs of these four serial chains generate the complete Lie algebra $se(3)$. Thus:

$$V_1^{m/f} \neq A_1^{m/f} \neq se(3) \tag{6.1}$$

and

$$V_j^{m/f} = A_j^{m/f} = se(3) \qquad \forall j = 2, 3, 4, 5. \tag{6.2}$$

where $V^{m/f}$ is the infinitesimal mechanical liaison and $A^{m/f}$ is the closure algebra between the fixed and the moving platforms.

In addition,

$$\sum_{i=1}^{r1} f_{1i} = 4 = \dim\left(V_1^{m/f}\right). \tag{6.3}$$

where $r1$ is the number of pairs in the first kinematic chain.

Moreover, the absolute closure algebra is given by:

$$A_a^{m/f} = \bigcap_{j=1}^{5} A_j^{m/f} \neq se(3). \tag{6.4}$$

Therefore, the parallel platform is a trivial parallel platform of Tanev's type [98]. The number of DoF of the complete parallel platform is given by:

$$F = \dim\left(V_1^{m/f}\right) + \sum_{j=2}^{5}\left[\sum_{i=1}^{r_j} f_j - \dim\left(A_j^{m/f}\right)\right] = 4 + \sum_{j=2}^{5}[7-6] = \underline{4} + 4. \tag{6.5}$$

As indicated in [98], the active DoF between the moving and the fixed platforms are given by the first term of the right hand side of the equation, and they are four. The same as the first kinematic chain RRPP. Moreover, there are four passive DoF associated with the four chains SPS since they can rotate around their own axes without affecting the motion of the moving platform.

As the number of DoF of the parallel platform is four, the final pose of the moving platform could be determined by the four prismatic pairs acting as the actuators of the platform. This is a convenient way to modelate the kinematic knee model since the prismatic pairs are anatomically related with the ligament elongations.

6.3 Position analysis

The position analysis can be clasified into two types: forward and inverse analysis, both are described below:

- forward analysis: consist on determining the final pose of the end effector knowing the values of the actuator pairs.
- inverse analysis: consist on detrmining the values of the actuator pairs knowing the pose of the end effector.

Since the final pose of the moving platform is restricted by the RRPP kinematic chain work-space, it is possible to perform the position analysis of the complete parallel platform only by this RRPP kinematic chain.

The position analysis of the RRPP kinematic chain is developed below, based on the Denavit-Hartenberg parameters described in **section 2.2.1**.

6.3.1 Denavit-Hartenberg description

Figure 6.6(a) shows the RRPP kinematic chain with its five bodies numbered, the coordinate systems of the femur and tibia, T^f and T^t, and the distances between the kinematic pairs. All the five coordinate systems required for the Denavit-Hartenberg description are shown in the Figure 6.6(b). The orientation and location of the coordinate systems are based on the proximal variant convention due to the advantages that it has over the other conventions described in **section 3.3**.

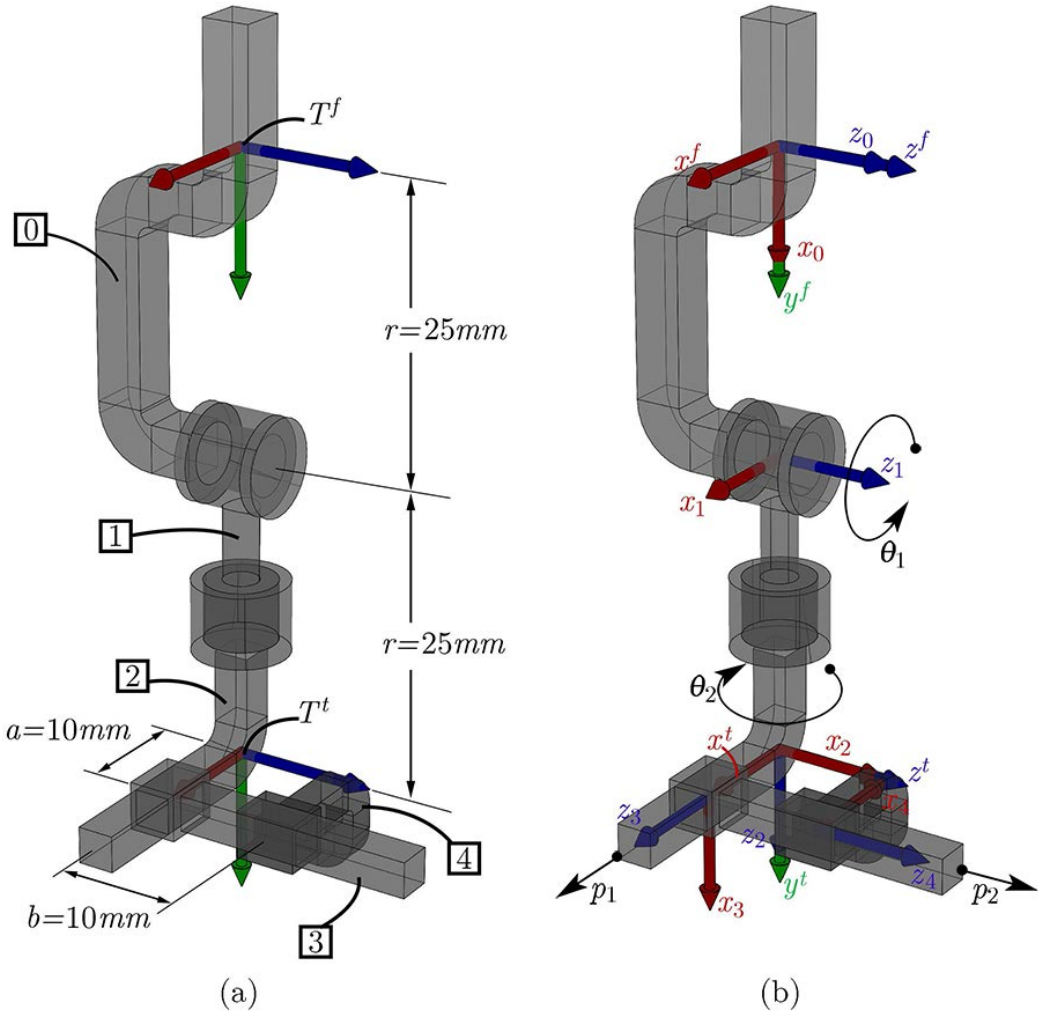

Figure 6.6: Kinematic chain RRPP with; (a) numbered bodies and distances between its kinematic pairs, and (b) Denavit-Hartenberg coordinate systems based on the proximal variant convention and the actuators of the kinematic chain.

The Denavit-Hartenberg parameters of the RRPP kinematic chain shown in Figure 6.6 are described in Table 6.4.

The homogeneous transform, ${}^f\mathbf{T}^t$, between the femur coordinate system T^f and the tibia coordinate system T^t is a composition of displacements and rotations along and

Table 6.4: Denavit-Hartenber parameters of the RRPP kinematic chain shown in Figure 6.6. Distances are in (mm) and angles are in (rad).

Coordinate system	a	α	d	θ
T^f	0	0	-	-
0	r	0	0	$\pi/2$
1	0	$-\pi/2$	0	$-\pi/2+\theta_1$
2	0	$-\pi/2$	r	$-\pi/2+\theta_2$
3	0	$-\pi/2$	$a+p_1$	$-\pi/2$
4	a	0	$b+p_2$	$\pi/2$
T^t	-	-	$-b$	π

around the x and z axes. This complete homogeneous transform is given by:

$$\begin{aligned} {}^f\mathbf{T}^t &= \mathbf{Z}(0,\pi/2)\,\mathbf{X}(r,0)\,\mathbf{Z}(0,-\pi/2+\theta_1)\,\mathbf{X}(0,-\pi/2)\,\mathbf{Z}(r,-\pi/2+\theta_2)\,\mathbf{X}(0,-\pi/2) \\ &\quad \mathbf{Z}(a+p_1,-\pi/2)\,\mathbf{X}(0,-\pi/2)\,\mathbf{Z}(b+p_2,\pi/2)\,\mathbf{X}(a,0)\,\mathbf{Z}(-b,\pi) \end{aligned} \tag{6.6}$$

This homogeneous transform has the form:

$${}^f\mathbf{T}^t = \begin{bmatrix} {}^f\mathbf{R}^t & {}^f\boldsymbol{t}^t \\ \mathbf{0} & 1 \end{bmatrix} \tag{6.7}$$

where

$${}^f\mathbf{R}^t = \begin{bmatrix} \cos\theta_1\cos\theta_2 & -\sin\theta_1 & \cos\theta_1\sin\theta_2 \\ \sin\theta_1\cos\theta_2 & \cos\theta_1 & \sin\theta_1\sin\theta_2 \\ -\sin\theta_2 & 0 & \cos\theta_2 \end{bmatrix}, \tag{6.8}$$

and

$${}^f\boldsymbol{t}^t = \begin{bmatrix} p_2\cos\theta_1\sin\theta_2 + p_1\cos\theta_1\cos\theta_2 - r\sin\theta_1 \\ p_2\sin\theta_1\sin\theta_2 + p_1\sin\theta_1\cos\theta_2 + r\cos\theta_1 + r \\ p_2\cos\theta_2 - p_1\sin\theta_2 \end{bmatrix}. \tag{6.9}$$

Equations (6.7), (6.8) and (6.9) define the pose of the T^t relative to T^f. The final position depends on the RRPP pair values; θ_1 around z_1, θ_2 around z_2, p_1 along z_3 and p_2 along z_4.

For the forward position analysis we can put the values of the actuator pairs θ_1, θ_2, p_1 and p_2 into the equations (6.8) and (6.9) to determine the pose of the tibia coordinate system relative to the femur coordinate system, ${}^f\mathbf{T}^t$. For the inverse position analysis, the elements of the orientation matrix ${}^f\mathbf{R}^t$ and the position vector ${}^f\boldsymbol{t}^t$ are matched with the corresponding in the goal pose and the equations are solved to compute the values of the actuator pairs necessary to reach that pose, ${}^f\mathbf{T}^t$.

6.3.2 Final pose approximation

As the kinematic chain RRPP has 4-DoF, it cannot reach any spatial position. Sometimes, it is necessary to compute the most similar spatial position to a given spatial position that the kinematic chain can reach.

The most similar spatial position is a relative problem that can be addressed in several ways. Here, an easy sequential procedure to compute the values of the actuator pairs to reach a similar spatial position is presented. Since the kinematic chain RRPP has great anatomical significance, important differences between the goal spatial position and the similar spatial position are not expected.

The process to compute the values of the actuator pairs to reach a similar spatial position to a given one, has the following steps:

1. Compute the values of θ_1 and θ_2 from the rotation matrix ${}^f\mathbf{R}^t$, equation (6.8), to set one of the three axes ${}^f x^t$, ${}^f y^t$ or ${}^f z^t$ in the direction of its corresponding axis in the goal orientation matrix.

   - To reach the direction of the axis ${}^f x^t$ lets solve the elements of the first column of ${}^f\mathbf{R}^t$ for θ_1 and θ_2.

2. With the values of θ_1 and θ_2, the orientation matrix ${}^f\mathbf{R}^t$ is completely defined and its other two axes must be similar to their corresponding ones in the goal orientation.

3. Once the values are computed of θ_1 and θ_2 they can be substituted into the position vector ${}^f\boldsymbol{t}^t$, equation (6.9), and two of its three elements are solved for p_1 and p_2 to reach the corresponding two components in the goal position vector.

   - Compute p_1 and p_2 with the first and second elements of the ${}^f\boldsymbol{t}^t$ that match with the ${}^f t_x^t$ and ${}^f t_y^t$ components in the goal position vector.

4. With the values of p_1 and p_2, the position vector ${}^f\boldsymbol{t}^t$ is completely defined and its remaining component must be similar to the corresponding one in the goal position vector.

6.4 Example: Inverse position analysis during flexion task

The inverse position analysis was performed for the MT3 of volunteer 2, see Figure 5.15, which is the semi-active flexion task starting from the full extension position. This motion task covers an angle of about 50° and it was divided in 21 spatial positions each 2.5°. In order to visualize the work-space of this MT in a better way, lets plot only 8 of the 21 spatial positions as shown in Figure 6.7.

First, the plane that best fits the origins of the systems T_i^B was computed, and then the circle that best fits the set of projected points on that plane. An arc segment of the circle that best fits the set of points as well as the axis perpendicular to the plane, $\hat{\boldsymbol{n}}$, through the center of the circle, c_c, are shown in Figure 6.8.

After that, the kinematic knee model is located with the y axis of the systems T^f and T^t aligned with the origin of the first spatial position T_1^B. The midpoint between the sphere centers located on the center of the circle c_c and with the z axis of the systems T^f and T^t in the direction of the vector perpendicular to the plane $\hat{\boldsymbol{n}}$, as shown in Figure 6.9.

Figure 6.7: 11 spatial positions of the MT3 work-space for the volunteer 2.

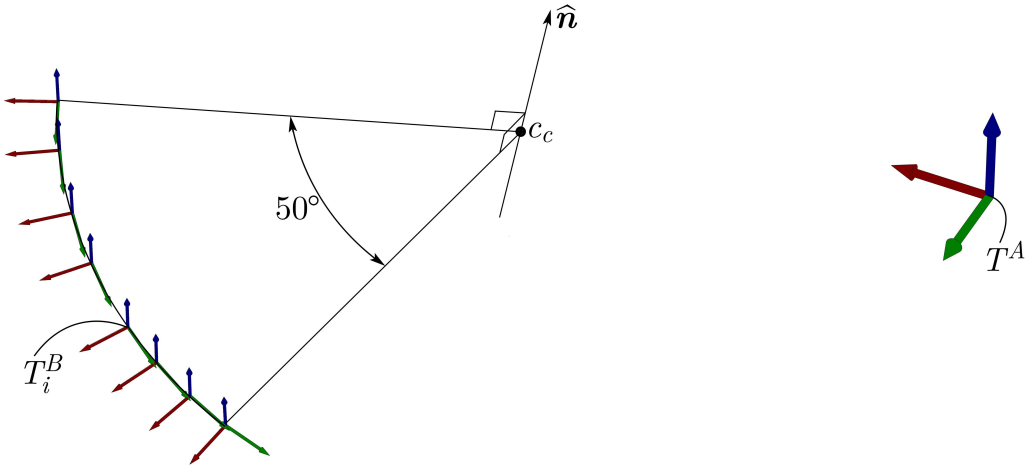

Figure 6.8: Arc segment of the circle that best fit the set of points of the work-space shown in Figure 6.7, and the axis perpendicular to the plane, $\hat{\boldsymbol{n}}$ through the center of the circle, c_c.

To perform the inverse position analysis it is necessary to refer both coordinate systems T^f and T^t of the kinematic knee model, relative to the fixed frame T^A, see Figure 6.9. As the femur model is fixed during the motion task, then the coordinate system of the femur T^f is also fixed, therefore, the homogeneous transform of the femur system T^f, relative to the fixed system T^A, ${}^A\mathbf{T}^f$, remains constant during the motion task. This homogeneous transform is composed by a rotation matrix ${}^A\mathbf{R}^f$ and a translation vector ${}^A\boldsymbol{t}^f$ defined by:

$$ {}^A\mathbf{R}^f = \begin{bmatrix} \hat{\boldsymbol{x}} & \hat{\boldsymbol{y}} & \hat{\boldsymbol{z}} \end{bmatrix}, \tag{6.10} $$

where:

$$ \hat{\boldsymbol{y}} = \frac{\boldsymbol{t}_1^B - \boldsymbol{c}_c}{|\boldsymbol{t}_1^B - \boldsymbol{c}_c|}, \qquad \hat{\boldsymbol{z}} = \hat{\boldsymbol{n}}, \qquad \hat{\boldsymbol{x}} = \hat{\boldsymbol{y}} \times \hat{\boldsymbol{z}}, $$

and

$$ {}^A\boldsymbol{t}^f = \boldsymbol{c}_c - r\,\hat{\boldsymbol{y}}. \tag{6.11} $$

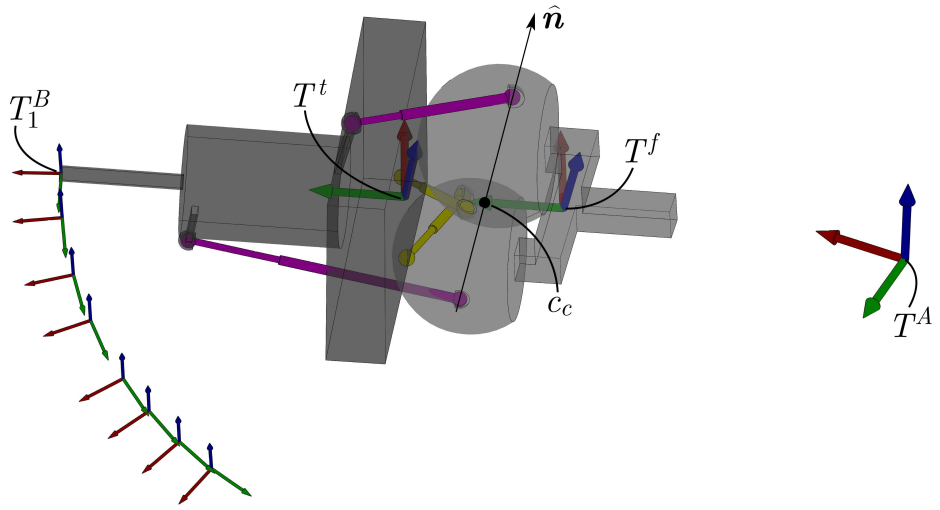

Figure 6.9: Location of the kinematic knee model to perform the inverse position analysis of the MT3.

The tibia coordinate system, T^t, changes its pose relative to the fixed coordinate system, T^A, during the motion task. The homogeneous transform of the tibia system T_i^t for each position i, relative to the fixed system T^A, ${}^A\mathbf{T}_i^t$ can be defined by:

$$ {}^A\mathbf{T}_i^t = {}^A\mathbf{T}_i^B({}^t\mathbf{T}^B)^{-1} \tag{6.12} $$

Since there is a rigid attachment between the system T_i^t and the final moving system T_i^B, the homogeneous transform ${}^t\mathbf{T}^B$ is a constant matrix during all the motion task. This constant homogeneous matrix ${}^t\mathbf{T}^B$ can be computed by using the first spatial position, $i = 1$, shown in Figure 6.9, and is given by:

$$ {}^t\mathbf{T}^B = ({}^A\mathbf{T}_1^t)^{-1}{}^A\mathbf{T}_1^B \tag{6.13} $$

where ${}^A\mathbf{T}_1^t$ is the homogeneous transform of the tibia coordinate system T^t relative to the fixed system T^A in the first spatial position, which has the same rotation matrix as the homogeneous transform of the femur coordinate system relative to the fixed frame ${}^A\mathbf{T}^f$, then:

$$ {}^A\mathbf{R}_1^t = {}^A\mathbf{R}^f, \tag{6.14} $$

and the translation vector is given by:

$$ {}^A\boldsymbol{t}_1^f = \boldsymbol{c}_c + r\,\hat{\boldsymbol{y}}. \tag{6.15} $$

The inverse position analysis was obtained by applying the procedure described in the **section 6.3.2** which consists on determining the values of the actuator pairs of the kinematic chain RRPP to reach an approximation of the goal pose. The error between the approximation pose and the goal pose are ploted in the Figures 6.10 and 6.11. These differences are in terms of the angle between the axes ${}^f\boldsymbol{x}^t$, ${}^f\boldsymbol{y}^t$ and ${}^f\boldsymbol{z}^t$ and the distance between points ${}^f\boldsymbol{t}^t$ in the approximation pose and the goal pose.

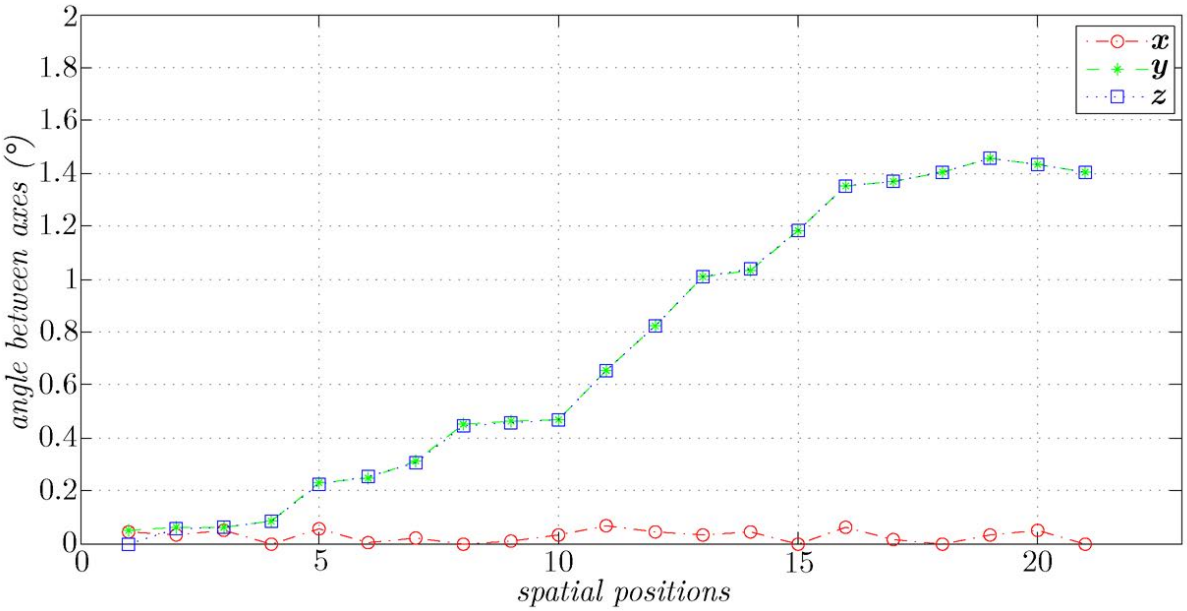

Figure 6.10: Orientation error: angle between the axes of the approximation pose and their corresponding in the goal pose.

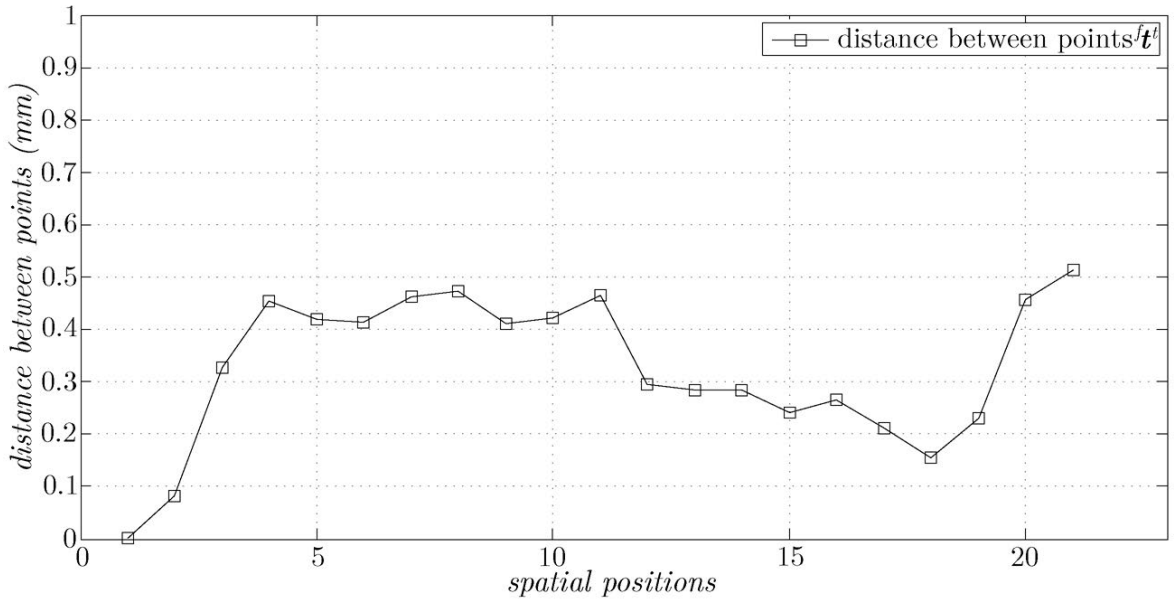

Figure 6.11: Position error: distance between the origin point of the approximation pose and its corresponding in the goal pose.

6.4.1 Ligament length variations

Once computed the homogeneous matrices ${}^A\mathbf{T}^f$ and ${}^A\mathbf{T}_i^t$ of the femur and tibia coordinate systems relative to the fixed frame T^A, it is possible to writte the vector position of the insertion points A_i and B_i, $\boldsymbol{a}_i$ and $\boldsymbol{b}_i$, $i = 1, 2, 3, 4.$ with respect to the fixed frame T^A as

follows:

$$\boldsymbol{a}_i^A = {}^A\mathbf{T}^f \boldsymbol{a}_i^f, \qquad i = 1, 2, 3, 4. \tag{6.16}$$

$$\boldsymbol{b}_{ij}^A = {}^A\mathbf{T}_j^t \boldsymbol{b}_i^t, \qquad i = 1, 2, 3, 4. \quad j = 1, 2, ..., 21. \tag{6.17}$$

Therefore, the length of each ligament chain in each spatial position can be computed by:

$$L_{ij} = \left| \boldsymbol{a}_i^A - \boldsymbol{b}_{ij}^A \right| \qquad i = 1, 2, 3, 4. \quad j = 1, 2, ..., 21. \tag{6.18}$$

Computing these lengths of the SPS chains for the 21 spatial positions of the MT, the ligament length variation of the ACL, PCL, MCL and LCL ligament chains during the first 50° of the semi-active flexion MT are obtained. The curves of the ligament length variations during the first 50° of the flexion of the MT3 are shown in Figure 6.12.

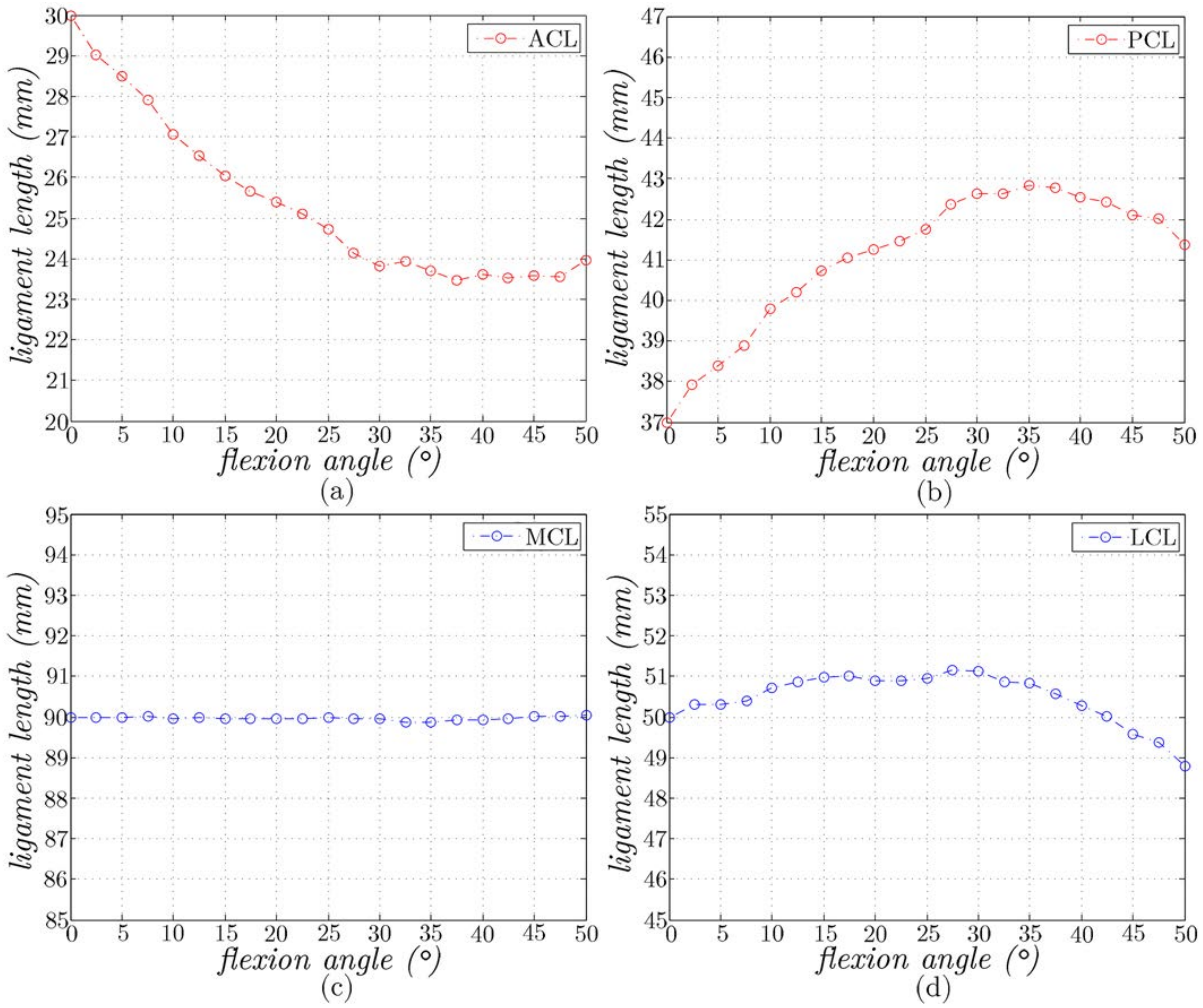

Figure 6.12: Ligament length variation during the first 50° of the flexion motion for; (a) ACL, (b) PCL, (c) MCL and (d) LCL.

6.4.2 Simulation

The simulation was performed in SolidWorks®. The prismatic pairs of the SPS kinematic chains were configurated as linear actuators with the values given by the ligament length variation curves as shown in the Figure 6.13.

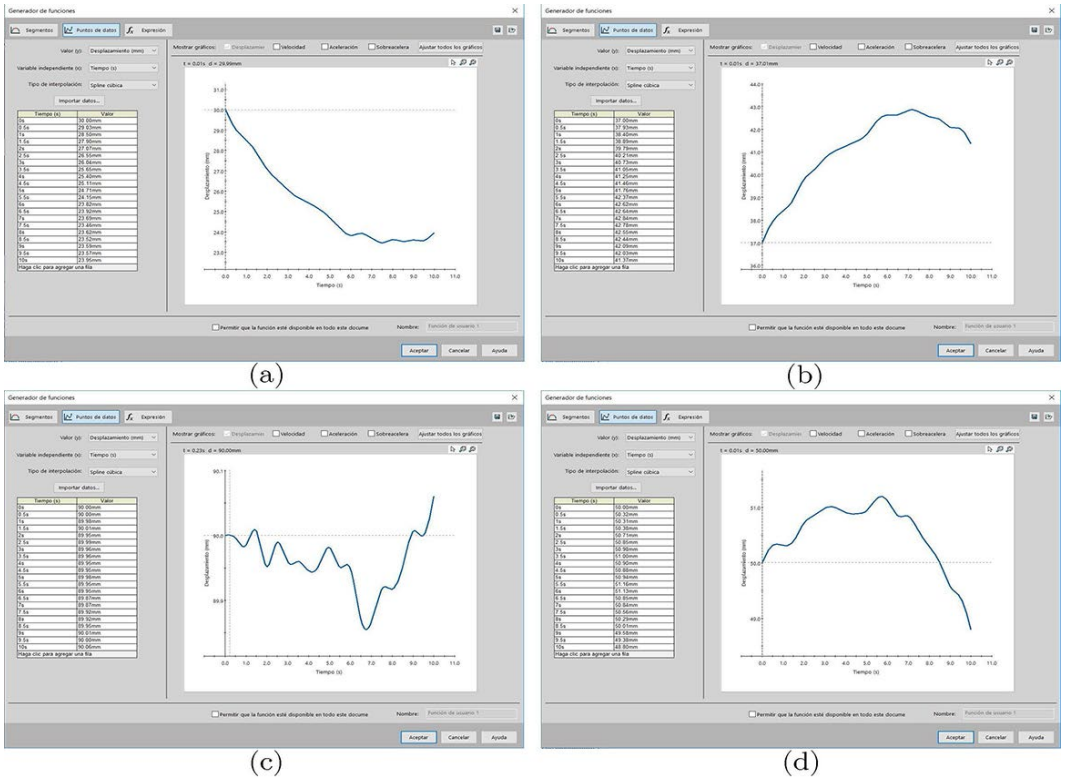

Figure 6.13: Configuration of the prismatic pairs of the SPS kinematic chains as linear actuators for the SolidWorks®'s simulation; (a) ACL, (b) PCL, (c) MCL and (d) LCL.

The kinematic knee model reaching four of the eight spatial positions of Figure 6.7 is shown in Figure 6.14.

6.5 Adjustment process: the ligament length variations

The kinematic knee model at this point is capable to reach a general work-space with high accuracy during the first 50° of flexion rotation. As described in the previous section, this is performed by the ligament lenght variations during the MT, which depends on the position of the insertions (spherical pairs) A_i and B_i, $i = 1, 2, 3, 4$ in the femur and tibia models.

Some studies performed with *in vitro* specimens, extracted the ligament length variations of ACL, PCL, MCL and LCL during the knee flexion rotation and are reported in the literature by means of graphical curves [7], polinomial aproximations [57] or simply tables of data [102]. The final objective of this thesis is a kinematic knee model capable

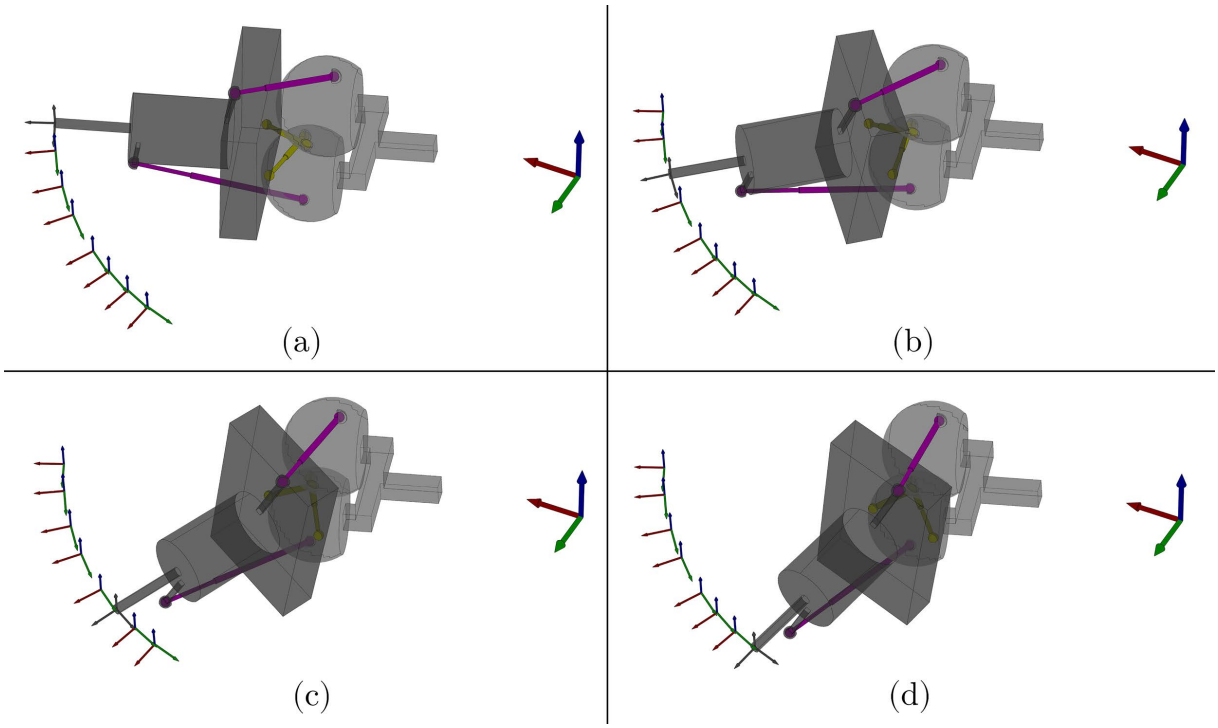

Figure 6.14: Complete kinematic knee model reaching four spatial positions during the simulation.

to reach a general WS of the knee and at the same time to modelate prescribed ligament length variations during that WS.

The ligaments have some principal fibres that have their own length variations, but in the proposed knee model the ligaments were simplified as only one fibre. The following procedure can be extended to any number of fibres by setting a SPS kinematic chain for each ligament fibre that is required in the analysis.

Let's define the prescribed ligament length variations as the reported by Belvedere et al. [7] in which the authors show the results by curves and polynomial functions in percentage of the ligament lengths vs the flexion angle. The selected fibres that act as the prescribed ligament length variations reported in [7] are ACL=AM, PCL=AL, MCL=pAB and LCL=pWB. These prescribed curves for the first 50° of the flexion, are shown in the Figure 6.15, and their corresponding polynomial functions are presented in Table 6.5.

Table 6.5: Prescribed polynomial functions, $L_i^*(\theta)$ of the ligament length curves shown in the Figure 6.15. Variable $L_i^*(\theta)$ is in (mm) and θ is in $(°)$.

Ligament	**Polynomio** $L_i^*(\theta)$						
	θ^6	θ^5	θ^4	θ^3	θ^2	θ^1	θ^0
ACL	6.271×10^{-9}	-1.018×10^{-6}	6.175×10^{-5}	-1.665×10^{-3}	0.0166	-0.0598	30
PCL	-1.694×10^{-8}	2.782×10^{-6}	-1.782×10^{-4}	5.562×10^{-3}	-0.0829	0.5837	37
MCL			1.294×10^{-6}	-1.659×10^{-4}	0.00794	-0.2365	90
LCL	-2.123×10^{-9}	4.195×10^{-7}	-2.942×10^{-5}	8.338×10^{-4}	-0.00613	-0.1485	50

The adjustment is possible by changing the positions of the ligament insertions A_i and B_i, locating them in the positions that minimize the distance betwen the actual length L_i

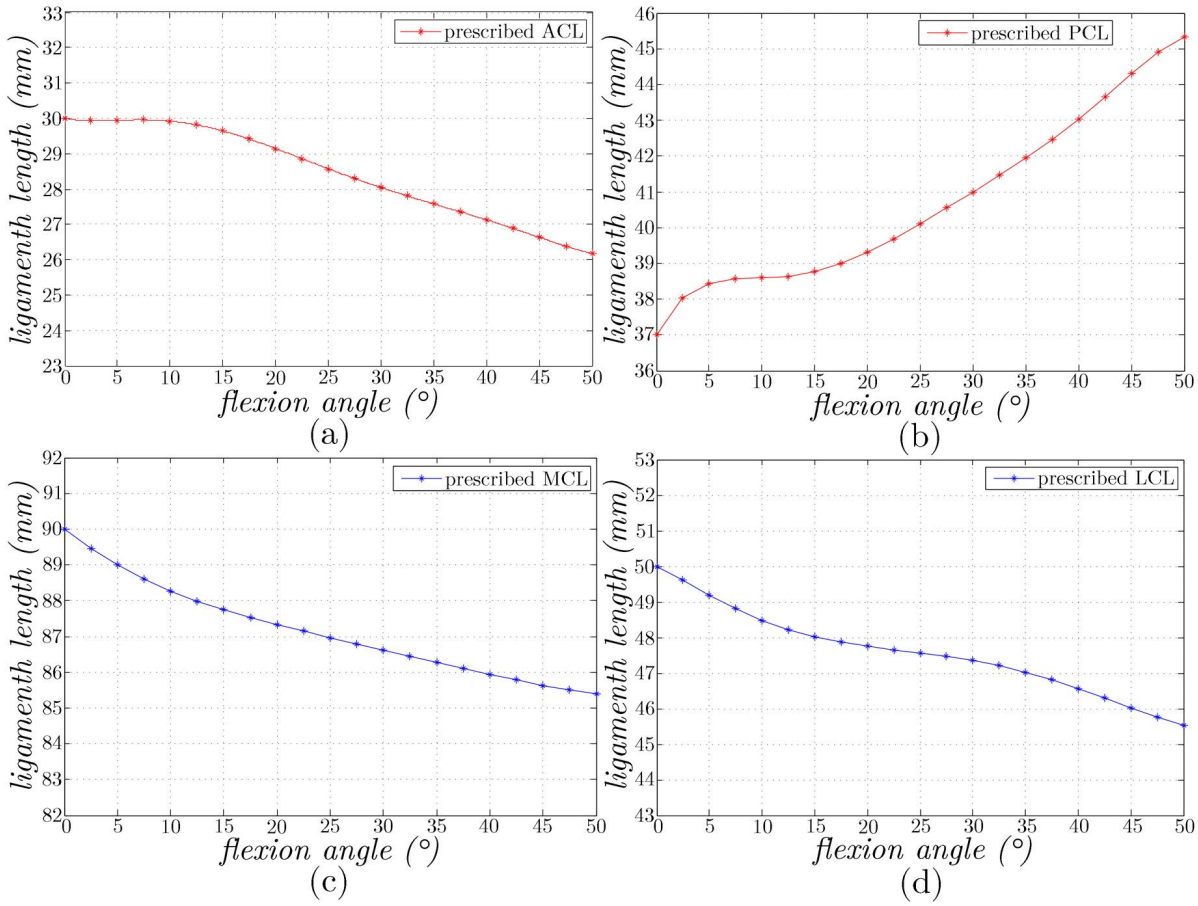

Figure 6.15: Prescribed ligament length curves modified from [7]; (a) ACL, (b) PCL, (c) MCL and (d) LCL.

and the prescribed length, L_i^*, during the motion. The mathematical formulation of this adjustment problem is described in the following section.

6.5.1 Mathematical description

The adjustment problem consists on determining the insertion positions for which the ligament length variation curves be the most similar as possible to the prescribed ligament length variation curves $L_i^*(\theta)$, see Table 6.5. This problem is solved by the least squares method in the non-linear sense, addressed in the **sections 3.1.1** and **3.1.2**.

The error functions to minimize are given by:

$$E_i = \sum_{j=1}^{n} \left(|\boldsymbol{a}_i^A - \boldsymbol{b}_{ij}^A| - L_i^* \right)^2, \qquad i = 1, 2, 3, 4. \tag{6.19}$$

where n is the number of spatial positions and:

$$\boldsymbol{a}_i^A = {}^A\mathbf{T}^f \boldsymbol{a}_i^f \qquad \boldsymbol{b}_{ij}^A = {}^A\mathbf{T}_j^t \boldsymbol{b}_i^t$$

Moreover, the vectors of the insertion points relative to the femur an tibia systems, $\boldsymbol{a}_i^f$ and $\boldsymbol{b}_i^t$, are given as:

$$\boldsymbol{a}_i^f = [x_{ai},\ y_{ai},\ z_{ai}]^T \qquad \boldsymbol{b}_i^t = [x_{bi},\ y_{bi},\ z_{bi}]^T \qquad i = 1, 2, 3, 4. \tag{6.20}$$

And, the functions to minimize can be written as:

$$E_i = \sum_{j=1}^{n} \left(d_{ij}(\boldsymbol{u})\right)^2, \qquad i = 1, 2, 3, 4. \tag{6.21}$$

where the vector of variables is $\boldsymbol{u} = [x_{ai}, y_{ai}, z_{ai}, x_{bi}, y_{bi}, z_{bi}]^T$ and $d_{ij}(\boldsymbol{u}) = |\boldsymbol{a}_i^A - \boldsymbol{b}_{ij}^A| - L_i^*$.

The Jacobian matrix $\mathbf{J}_i(\boldsymbol{u})$ and the vector $\boldsymbol{d}_i(\boldsymbol{u})$ are given by:

$$\mathbf{J}_i(\boldsymbol{u}) = \begin{bmatrix} \frac{\partial d_{i1}(\boldsymbol{u})}{\partial x_{ai}} & \frac{\partial d_{i1}(\boldsymbol{u})}{\partial y_{ai}} & \frac{\partial d_{i1}(\boldsymbol{u})}{\partial z_{ai}} & \frac{\partial d_{i1}(\boldsymbol{u})}{\partial x_{bi}} & \frac{\partial d_{i1}(\boldsymbol{u})}{\partial y_{bi}} & \frac{\partial d_{i1}(\boldsymbol{u})}{\partial z_{bi}} \\ \frac{\partial d_{i2}(\boldsymbol{u})}{\partial x_{ai}} & \frac{\partial d_{i2}(\boldsymbol{u})}{\partial y_{ai}} & \frac{\partial d_{i2}(\boldsymbol{u})}{\partial z_{ai}} & \frac{\partial d_{i2}(\boldsymbol{u})}{\partial x_{bi}} & \frac{\partial d_{i2}(\boldsymbol{u})}{\partial y_{bi}} & \frac{\partial d_{i2}(\boldsymbol{u})}{\partial z_{bi}} \\ \vdots & \vdots & \vdots & \vdots & \vdots & \vdots \\ \frac{\partial d_{in}(\boldsymbol{u})}{\partial x_{ai}} & \frac{\partial d_{in}(\boldsymbol{u})}{\partial y_{ai}} & \frac{\partial d_{in}(\boldsymbol{u})}{\partial z_{ai}} & \frac{\partial d_{in}(\boldsymbol{u})}{\partial x_{bi}} & \frac{\partial d_{in}(\boldsymbol{u})}{\partial y_{bi}} & \frac{\partial d_{in}(\boldsymbol{u})}{\partial z_{bi}} \end{bmatrix}, \qquad i = 1, 2, 3, 4. \tag{6.22}$$

$$\boldsymbol{d}_i(\boldsymbol{u}) = \begin{bmatrix} d_{i1}(\boldsymbol{u}) \\ d_{i2}(\boldsymbol{u}) \\ \vdots \\ d_{in}(\boldsymbol{u}) \end{bmatrix}, \qquad i = 1, 2, 3, 4. \tag{6.23}$$

The adjustment problem was solved for the four SPS ligament kinematic chains by the Gauss-Newton alghorithm given by equation (3.8) and the initial guesses were given by the ligament insertion positions described in Table 6.3. Additionally, in the **Appendix C** it is shown that the proposed adjustment problem leads to a convex function which means that the computed results are the best possible results.

6.5.2 Results

After the adjustment procedure, the kinematic knee model in full extension position with its adjusted insertion points is shown in the Figure 6.16, and the final coordinates of the insertion points relative to the tibia and femur systems are presented in the Table 6.6.

The graphical comparison of the prescribed ligament length variation curves and the obtained by the inverse position analysis with the insertion points in the adjusted locations, A_i^* and B_i^*, are shown in the Figure 6.17.

The error performance between the prescribed and the adjusted ligament length variations are shown in the Figure 6.18.

6.5.3 Simulation

The simulation was performed in SolidWorks®. The prismatic pairs of the SPS kinematic chains were configurated as linear actuators with the values given the ligament length variation curves after the adjustment procedure as shown in Figure 6.19.

The kinematic knee model with the ligament insertion points in the adjusted locations, reaching four of the eight spatial positions of the Figure 6.7 is shown in Figure 6.20.

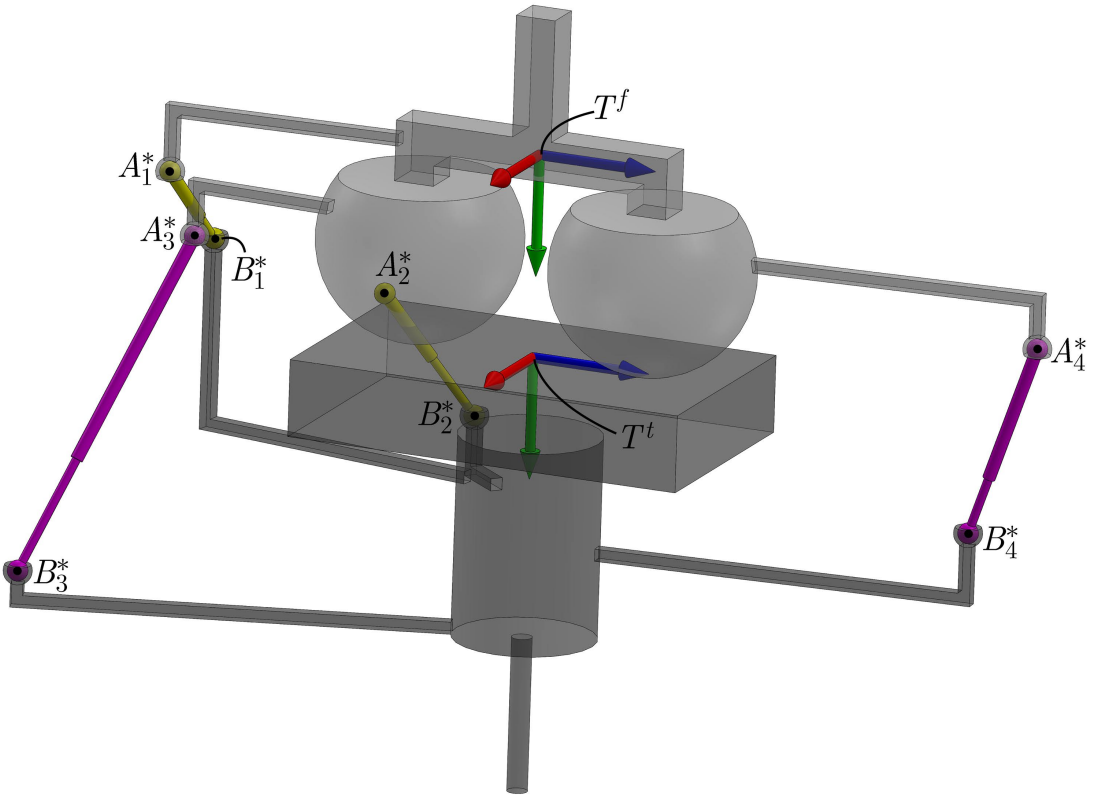

Figure 6.16: Kinematic knee model with the insertion points in the adjusted locations.

Table 6.6: Adjusted location of the insertion points, A_i^* and B_i^* $i = 1, 2, 3, 4.$, relative to the femur and tibia coordinate systems T^f and T^t, Figure 6.3, (mm).

Ligament	**Insertion point**	**Coordinate system** (mm)					
		T^f			T^t		
ACL	A_1^*	5.1193	15.6729	-92.6641			
	B_1^*				-15.8335	-13.0394	-89.5185
PCL	A_2^*	-8.7018	42.2388	-42.2467			
	B_2^*				-19.9715	22.4554	-22.9102
MCL	A_3^*	-4.6104	33.6192	-89.8926			
	B_3^*				34.0266	60.28026	-116.6599
LCL	A_4^*	-9.2292	32.8432	125.7161			
	B_4^*				-8.3645	30.2319	109.7748

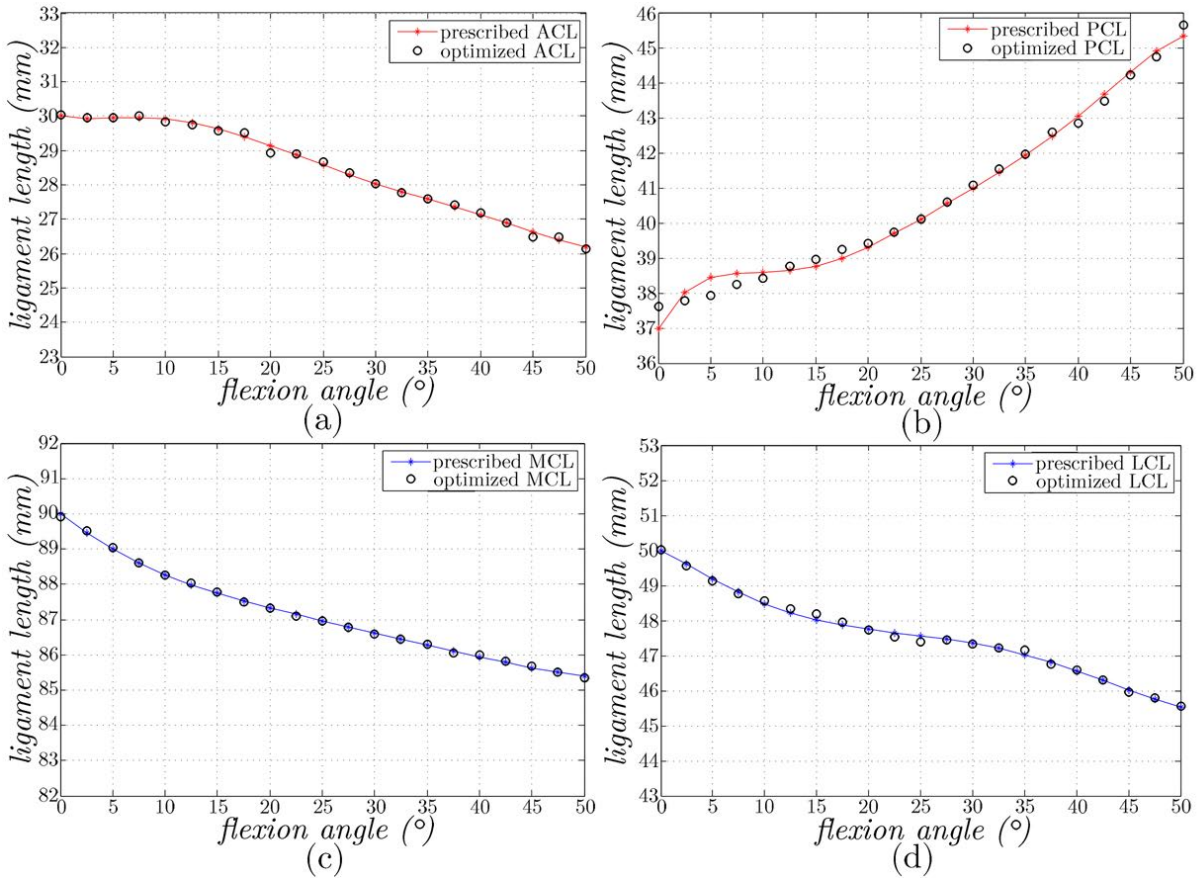

Figure 6.17: Prescribed ligament length variation curves and the obtained by inverse position analysis with the insertion points in the adjusted locations; (a) ACL, (b) PCL, (c) MCL and (d) LCL.

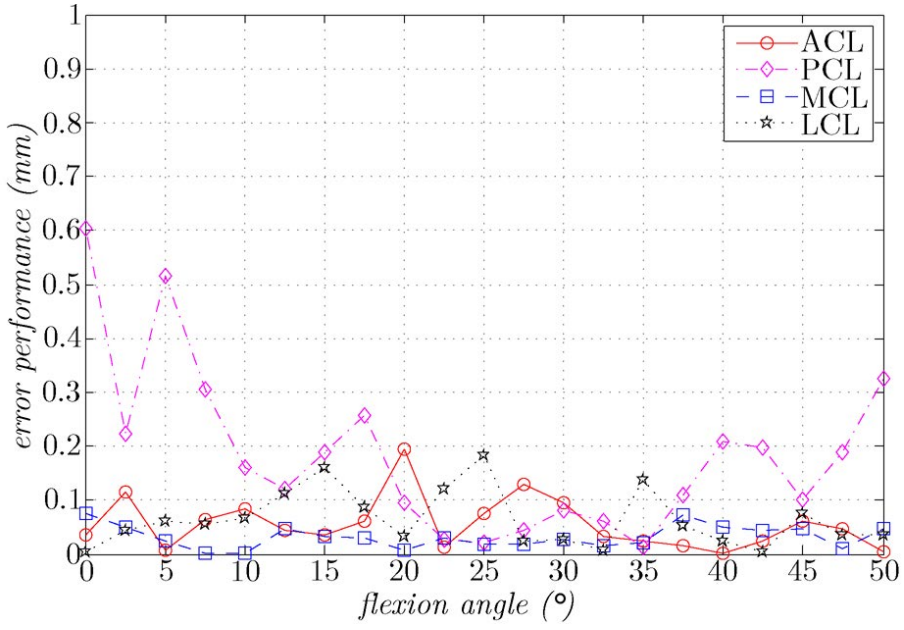

Figure 6.18: Error performance between the prescribed and the adjusted ligament length variations; (a) ACL, (b) PCL, (c) MCL and (d) LCL.

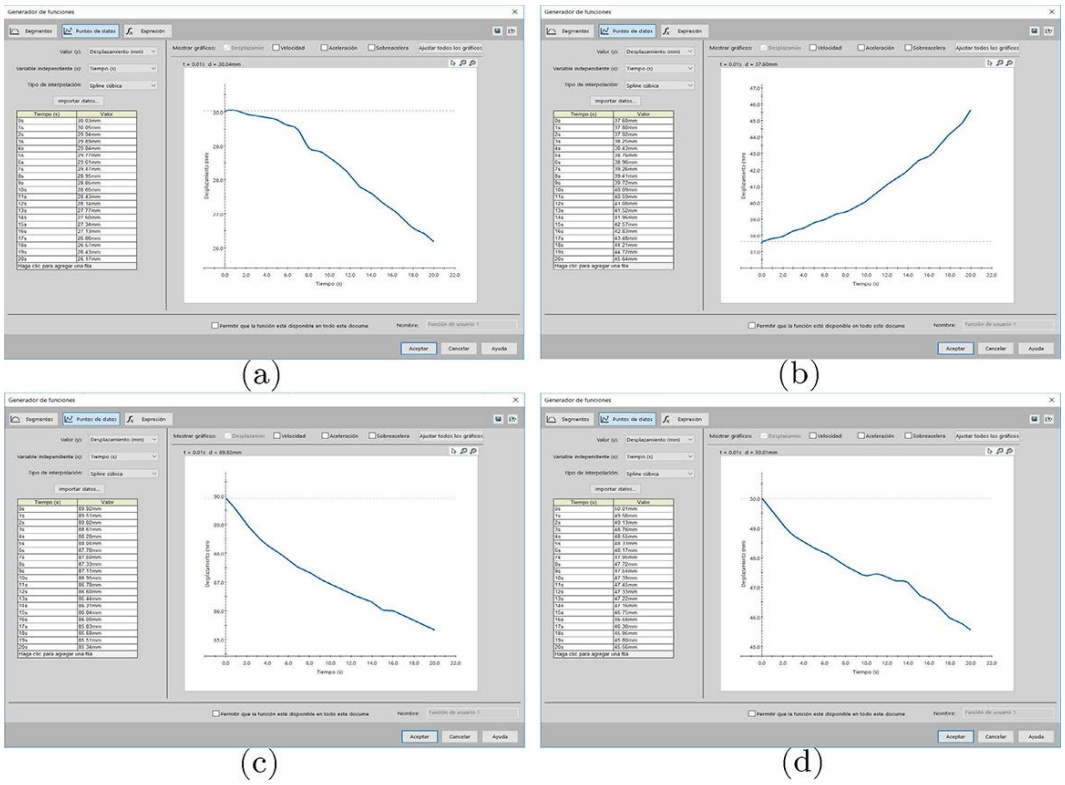

Figure 6.19: Configuration of the prismatic pairs of the SPS kinematic chains as linear actuators in the SolidWorks®'s simulation; (a) ACL, (b) PCL, (c) MCL and (d) LCL.

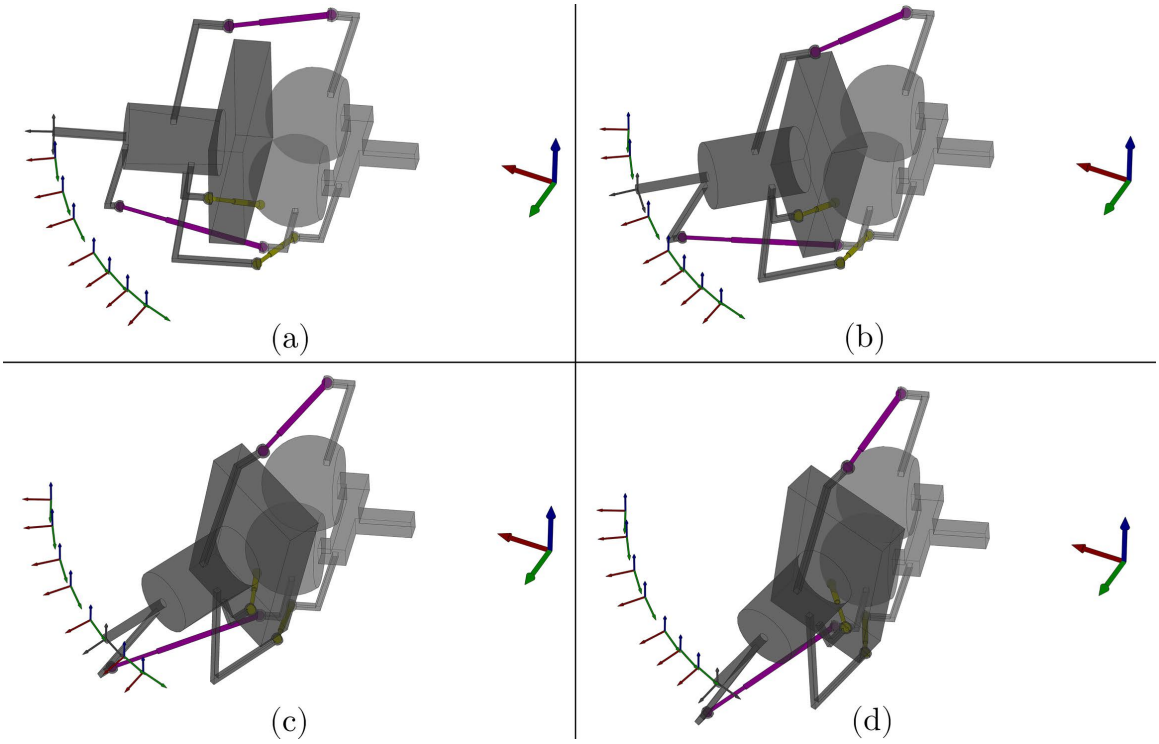

Figure 6.20: Complete kinematic knee model with the ligament insertion in the adjusted locations, reaching four spatial positions during the simulation.

Chapter 7

Conclusions and future work

In this chapter, the results obtained throughout this project are discussed and summarized. Moreover, as the kinematic knee model is a first approximation to more complex ones, this chapter also presents the bases and author's recommendations for future work.

7.1 Discussion and conclusions

In general, along with the development of this work, a new kinematic knee model with anatomical significance is proposed, which is capable to simulate ligament length variations of: ACL, PCL, MCL and LCL, and reach a 3D work-space experimentally obtained by a new measurement system based in photogrammetry that uses only one camera to extract 3D information.

First, a review of the measurement systems for joint motions of the human body is presented, specially for the knee joint, based on photogrammetric techniques and their main sources of error, such as: the STA which is the principal error source, allowing us to design an experiment with the least possible external error. Moreover, the basic recommendations on the reporting of kinematic data and extraction of the geometrical parameters of the knee joint were also reviewed, such as: the flexion-extension axis or the rotation center of the knee joint. The computation of geometrical parameters of the knee joint proved to be of great importance since it allows the location of the kinematic knee model during the evaluation of its capability to reach an experimental work-space.

After, a review of the kinematic knee models and their evolution over the years is presented, discovering that there is an opportunity area of including the behavior of the passive elements, such as the ligament length variations, into the model during a general motion task, remaining the model in a completely kinematic sense (no computational or finite element models).

Then, a photogrammetric measurement system is proposed with the principal characteristic that it uses only one camera to extract the 3-Dimensional information, making it cheaper and easier to implement than the conventional systems that use several cameras. Moreover, this measurement system has the advantage of not depending of markers placement. The calibration process of the measurement system is based on Zhang's algorithm and the homography matrix that allows the projection of 2D points of an image

into the 3D space and create spatial coordinate systems relative to the camera coordinate system. In addition, an accuracy study was proposed to evaluate the capability of the measurement system to extract reliable information during the data acquisition process. Concluding that the measurement system has the necessary reliability to be used in the proposed application.

Once the measurement system was evaluated, it can be included in the experimental procedure to obtain the knee work-space. This experimental procedure consists on the determination of the work-spaces of three different motion tasks (MT1: passive flexion-extension rotation, MT2: passive internal-external rotation and MT3: semi-active flexion-extension rotation). The displacement of two coordinate systems attached to the thigh and shank were collected to then get in the form of a work-space of all the spatial positions of the tibia coordinate system (system attached to the shank) relative to the femur coordinate system (system attached to the thigh). Then, the geometrical parameters of the knee during a motion task were computed based in mathematical and kinematical fundamentals as the fitting 3D geometries to a set of points and the screw line of a spatial displacement. Moreover, some processes were proposed to measure important characteristics of the knee motion such as: the so called automatic rotation of the knee during flexion-extension and the sliding between the tibia and femur bones. The results agree with the reported in the literature. These gratifying results suggest that this process can be used in the detection of knee issues and injuries by comparing the results with those of a healthy knee.

The measurement system is easy to implement and has enough accuracy for the proposed application, however, it has some limitations specially in the space that confines the motion tasks limiting the analysis to motion tasks that can be done in a small space as the gait analysis. Nevertheless, these limitations can be significantly reduced with a more powerful camera.

At the same time, a novel kinematic knee model with anatomical significance at the condyles of the femur and tibia, and at the ligament insertions and length variation behavior, that contains some important features of the kinematic knee models reported in the literature is proposed, which is also able to simulate ligament length variations in a completely kinematic sense; as far as the authors are aware there are not kinematic knee models proposed with this characteristic yet. The kinematic knee model is in a kinematical sense, a parallel platform RRPP+4-SPS with 4-DoF of Tanev's type with its mobility controlled by the RRPP kinematic chain. The parallel platform was evaluated by its capability to reach a semi-active motion task obtaining good results as extected since the model was based highly in the real knee anatomy and physiology.

An inverse kinematic analysis of the MT3 was performed to obtain the lengths of the SPS kinematics during the motion, which are related directly with the ligament length variations. As a last step, an adjustment process is performed where the ligament insertions (spherical pairs of the SPS chains) are relocated in order to obtain ligament length variation curves as similar to the prescribed ones.

These lead to a complete kinematic knee model capable to reach a 3D work-space with high accuracy and at the same time simulate the ligament length variations of the ACL, PCL, MCL and LCL, in the way that these would occur during the flexion task. This kinematic knee model is also able for subject-specific customization in the work-space and in the prescribed ligament length variations by modifying the kinematic parameters in

the model, such as: the spheres radii and the position of the insertion points, this is an important advantage over the computational models which are fully dependent of shapes and properties.

The complete and adjusted kinematic knee model laid the foundations for more complex model including more ligament fibres each with its specific length variation or models for dynamic analysis in a completely kinematic sense.

The kinematic knee model at this time is able to reproduce, with high accuracy, a workspace of the knee during passive and semi-active motion tasks. To extend the capability of this model to active motion tasks it is necessary to improve the kinematic constraints of the model and include other elements such as, the menisci. The model is also able to simulate prescribed ligament length variations during motion-tasks different than flexion, unfortunately this data are neither available in the literature nor for in vivo specimens.

7.2 Future work

As future work, it is planned to improve the measurement system by using a more powerful camera to compute geometric parameters and analyze more complex motion tasks of the knee and the human body in general.

The complete experimental procedure to extract kinematic data during a motion task has the additional advantage of not requiring clinicians to identify anatomical landmarks for markers placement, making the process accessible to be implemented by researchers without training in physioterapy. Then, it is necessary to perform the experimental procedure in a reasonably large sample of subjects with healthy knees to record a reliable database of the correct kinematic behavior of the knee. This database could be used to identify some issues and injuries by comparing the results with those of a healthy knee.

With respect to the kinematic knee model it is proposed to increase the complexity of it by including other passive elements such as the menisci or the patella, also more fibres to each of the modeled ligaments. After that, the next step is to transform the kinematic knee model into a dynamic knee model by including inertial features to the model and the addition of active elements such as the muscles.

The closest future work, is the use of the complete adjusted kinematic knee model to improve the design of important devices such as; active orthoses and rehabilitation mechanisms. And for the devices that currently exist the kinematic knee model could be used to develop exercises and rehabilitation trajectories that are more precise and focused on the specific elements that needed to recover.

References

[1] JJ O'Connor, TL Shercliff, E Biden, and JW Goodfellow. The geometry of the knee in the sagittal plane. *Proceedings of the Institution of Mechanical Engineers, Part H: Journal of Engineering in Medicine*, 203(4):223–233, 1989.

[2] DR Wilson and JJ O'Connor. A three-dimensional geometric model of the knee for the study of joint forces in gait. *Gait & Posture*, 5(2):108 – 115, 1997.

[3] R Di Gregorio and V Parenti-Castelli. A spatial mechanism with higher pairs for modelling the human knee joint. *Journal of Biomechanical Engineering*, 125(2):232 – 237, 2003.

[4] N Sancisi and V Parenti-Castelli. A new kinematic model of the passive motion of the knee inclusive of the patella. *Journal of Mechanisms and Robotics*, 3(4):041003, 2011.

[5] N Sancisi and V Parenti-Castelli. A novel 3d parallel mechanism for the passive motion simulation of the patella-femur-tibia complex. *Meccanica*, 46(1):207–220, 2011.

[6] Z Zhang et al. Flexible camera calibration by viewing a plane from unknown orientations. In *Iccv*, volume 99, pages 666–673, 1999.

[7] C Belvedere, A Ensini, A Feliciangeli, F Cenni, V D'Angeli, S Giannini, and A Leardini. Geometrical changes of knee ligaments and patellar tendon during passive flexion. *Journal of biomechanics*, 45(11):1886–1892, 2012.

[8] C Wilson. Knee joint anatomy.
url: https://www.knee-pain-explained.com/knee-joint-anatomy.html, 11/10/2018.
Reviewed by: KPE Medical Review Board.

[9] M Hoffman. Picture of the knee.
url:https://www.webmd.com/pain-management/knee-pain/picture-of-the-knee-1, 03/21/2017.

[10] KN Laubenthal, GL Smidt, and DB Kettelkamp. A quantitative analysis of knee motion during activities of daily living. *Physical therapy*, 52(1):34–43, 1972.

[11] GL Smidt. Biomechanical analysis of knee flexion and extension. *Journal of Biomechanics*, 6(1):79 – 92, 1973.

[12] We Tao, T Liu, R Zheng, and H Feng. Gait analysis using wearable sensors. *Sensors*, 12(2):2255–2283, 2012.

[13] E Papi, YN Bo, and AH McGregor. A flexible wearable sensor for knee flexion assessment during gait. *Gait & Posture*, 62:480 – 483, 2018.

[14] XS Papageorgiou, G Chalvatzaki, CS Tzafestas, and P Maragos. Hidden markov modeling of human normal gait using laser range finder for a mobility assistance robot. In *2014 IEEE International Conference on Robotics and Automation (ICRA)*, pages 482–487. IEEE, 2014.

[15] A Cappozzo, U Della Croce, A Leardini, and L Chiari. Human movement analysis using stereophotogrammetry: Part 1: theoretical background. *Gait & posture*, 21(2):186–196, 2005.

[16] G Wu and PR Cavanagh. Isb recommendations for standardization in the reporting of kinematic data. *Journal of biomechanics*, 28(10):1257–1261, 1995.

[17] G Wu, S Siegler, P Allard, C Kirtley, A Leardini, D Rosenbaum, M Whittle, D D D'Lima, L Cristofolini, H Witte, et al. Isb recommendation on definitions of joint coordinate system of various joints for the reporting of human joint motion—part i: ankle, hip, and spine. *Journal of biomechanics*, 35(4):543–548, 2002.

[18] R Stagni, S Fantozzi, and A Cappello. Double calibration vs. global optimisation: performance and effectiveness for clinical application. *Gait & posture*, 29(1):119–122, 2009.

[19] N. Spencer and J. Carter. Towards pose invariant gait reconstruction. In *IEEE International Conference on Image Processing 2005*, volume 3, pages III–261, Sep. 2005.

[20] L Chiari, U Della Croce, A Leardini, and A Cappozzo. Human movement analysis using stereophotogrammetry: Part 2: Instrumental errors. *Gait & posture*, 21(2):197–211, 2005.

[21] U Della Croce, A Leardini, L Chiari, and A Cappozzo. Human movement analysis using stereophotogrammetry: Part 4: assessment of anatomical landmark misplacement and its effects on joint kinematics. *Gait & posture*, 21(2):226–237, 2005.

[22] A Leardini, C Belvedere, F Nardini, N Sancisi, M Conconi, and V Parenti-Castelli. Kinematic models of lower limb joints for musculo-skeletal modelling and optimization in gait analysis. *Journal of Biomechanics*, 62:77–86, 2017.

[23] A Leardini, L Chiari, U Della Croce, and A Cappozzo. Human movement analysis using stereophotogrammetry: Part 3. soft tissue artifact assessment and compensation. *Gait & posture*, 21(2):212–225, 2005.

[24] A Cappozzo, F Catani, U Della Croce, and A Leardini. Position and orientation in space of bones during movement: anatomical frame definition and determination. *Clinical biomechanics*, 10(4):171–178, 1995.

[25] H Kainz, D Graham, J Edwards, HP Walsh, S Maine, R N Boyd, David G Ll, L Modenese, and CP Carty. Reliability of four models for clinical gait analysis. *Gait & posture*, 54:325–331, 2017.

[26] M Akbarshahi, AG Schache, JW Fernandez, R Baker, S Banks, and MG Pandy. Non-invasive assessment of soft-tissue artifact and its effect on knee joint kinematics during functional activity. *Journal of biomechanics*, 43(7):1292–1301, 2010.

[27] JP Holden, JA Orsini, KL Siegel, TM Kepple, LH Gerber, and Steven J S. Surface movement errors in shank kinematics and knee kinetics during gait. *Gait & Posture*, 5(3):217–227, 1997.

[28] FE Veldpaus, HJ Woltring, and LJMG Dortmans. A least-squares algorithm for the equiform transformation from spatial marker co-ordinates. *Journal of biomechanics*, 21(1):45–54, 1988.

[29] I Söderkvist and P Wedin. Determining the movements of the skeleton using well-configured markers. *Journal of biomechanics*, 26(12):1473–1477, 1993.

[30] L Cheze, BJ Fregly, and J Dimnet. A solidification procedure to facilitate kinematic analyses based on video system data. *Journal of biomechanics*, 28(7):879–884, 1995.

[31] TW Lu and JJ O'connor. Bone position estimation from skin marker co-ordinates using global optimisation with joint constraints. *Journal of biomechanics*, 32(2):129–134, 1999.

[32] MS Andersen, DL Benoit, M Damsgaard, DK Ramsey, and J Rasmussen. Do kinematic models reduce the effects of soft tissue artefacts in skin marker-based motion analysis? an in vivo study of knee kinematics. *Journal of biomechanics*, 43(2):268–273, 2010.

[33] S Duprey, L Cheze, and R Dumas. Influence of joint constraints on lower limb kinematics estimation from skin markers using global optimization. *Journal of biomechanics*, 43(14):2858–2862, 2010.

[34] X Gasparutto, N Sancisi, E Jacquelin, V Parenti-Castelli, and R Dumas. Validation of a multi-body optimization with knee kinematic models including ligament constraints. *Journal of biomechanics*, 48(6):1141–1146, 2015.

[35] G Valente, L Pitto, D Testi, A Seth, SL Delp, R Stagni, M Viceconti, and F Taddei. Are subject-specific musculoskeletal models robust to the uncertainties in parameter identification? *PLoS One*, 9(11):e112625, 2014.

[36] J Clément, R Dumas, N Hagemeister, and JA De Guise. Soft tissue artifact compensation in knee kinematics by multi-body optimization: performance of subject-specific knee joint models. *Journal of Biomechanics*, 48(14):3796–3802, 2015.

[37] J Ojeda, J Martínez-Reina, and J Mayo. The effect of kinematic constraints in the inverse dynamics problem in biomechanics. *Multibody System Dynamics*, 37(3):291–309, 2016.

[38] ES Grood and WJ Suntay. A joint coordinate system for the clinical description of three-dimensional motions: application to the knee. *Journal of biomechanical engineering*, 105(2):136–144, 1983.

[39] U Gamage, SS Hiniduma and J Lasenby. New least squares solutions for estimating the average centre of rotation and the axis of rotation. *Journal of biomechanics*, 35(1):87–93, 2002.

[40] K Halvorsen, M Lesser, and A Lundberg. A new method for estimating the axis of rotation and the center of rotation. *Journal of biomechanics*, 32(11):1221–1227, 1999.

[41] KL Markolf, PR Yang, NB Joshi, FA Petrigliano, and DR McAllister. In vitro determination of the passive knee flexion axis: Effects of axis alignment on coupled tibiofemoral motions. *Medical engineering & physics*, 2019.

[42] MH. Schwartz and A Rozumalski. A new method for estimating joint parameters from motion data. *Journal of Biomechanics*, 38(1):107 – 116, 2005.

[43] JR Essinger, PF Leyvraz, JH Heegard, and DD Robertson. A mathematical model for the evaluation of the behaviour during flexion of condylar-type knee prostheses. *Journal of Biomechanics*, 22(11-12):1229–1241, 1989.

[44] J Goodfellow and J O'Connor. The mechanics of the knee and prosthesis design. *The Journal of bone and joint surgery. British volume*, 60(3):358–369, 1978.

[45] L Blankevoort, R Huiskes, and A De Lange. The envelope of passive knee joint motion. *Journal of biomechanics*, 21(9):705–720, 1988.

[46] JM McCarthy. *21st century kinematics*. Springer, 2014.

[47] R Franci, V Parenti-Castelli, and N Sancisi. A three-step procedure for the modelling of human diarthrodial joints. *Int. J. Mech. Control*, 10(1):3–12, 2009.

[48] MH Moeinzadeh, AE Engin, and N Akkas. Two-dimensional dynamic modeling of human knee joint. *Journal of Biomechanics*, 15(4):346, 1982.

[49] TMGJ Van Eijden, E Kouwenhoven, J Verburg, and WA Weijs. A mathematical model of the patellofemoral joint. *Journal of biomechanics*, 19(3):219–229, 1986.

[50] E Abdel-Rahman and MS Hefzy. A two-dimensional dynamic anatomical model of the human knee joint. *Journal of biomechanical engineering*, 115(4A):357–365, 1993.

[51] HS Gill and JJ O'Connor. Biarticulating two-dimensional computer model of the human patellofemoral joint. *Clinical Biomechanics*, 11(2):81 – 89, 1996.

[52] N Sancisi and V Parenti-Castelli. A sequentially-defined stiffness model of the knee. *Mechanism and Machine Theory*, 46(12):1920 – 1928, 2011.

[53] V Parenti-Castelli and R Di Gregorio. Parallel mechanisms applied to the human knee passive motion simulation. In *Advances in Robot Kinematics*, pages 333–344. Springer, 2000.

[54] V Parenti-Castelli, A Leardini, R Di Gregorio, and JJ O'Connor. On the modeling of passive motion of the human knee joint by means of equivalent planar and spatial parallel mechanisms. *Autonomous Robots*, 16(2):219–232, 2004.

[55] DR Wilson, JD Feikes, and JJ O'connor. Ligaments and articular contact guide passive knee flexion. *Journal of biomechanics*, 31(12):1127–1136, 1998.

[56] A Ottoboni, V Parenti-Castelli, N Sancisi, C Belvedere, and A Leardini. Articular surface approximation in equivalent spatial parallel mechanism models of the human knee joint: an experiment-based assessment. *Proceedings of the Institution of Mechanical Engineers, Part H: Journal of Engineering in Medicine*, 224(9):1121–1132, 2010.

[57] E Bergamini, H Pillet, J Hausselle, P Thoreux, S Guerard, V Camomilla, A Cappozzo, and W Skalli. Tibio-femoral joint constraints for bone pose estimation during movement using multi-body optimization. *Gait & posture*, 33(4):706–711, 2011.

[58] X Gasparutto, R Dumas, and E Jacquelin. Multi-body optimisation with deformable ligament constraints: influence of ligament geometry. *Computer methods in biomechanics and biomedical engineering*, 15(sup1):191–193, 2012.

[59] N Sancisi and V Parenti-Castelli. A new 3d kinematic model of the tibio-femoral joint during knee passive motion. *Proceedings of AIMeTA*, pages 11–14, 2007.

[60] N Sancisi and V Parenti-Castelli. A 1-dof parallel spherical wrist for the modelling of the knee passive motion. *Mechanism and Machine Theory*, 45(4):658–665, 2010.

[61] I Sintini, N Sancisi, and V Parenti-Castelli. Comparison between anatomical and approximate surfaces in a 3d kinetostatic model of the knee for the study of the unloaded and loaded joint motion. *Meccanica*, 53(1-2):7–20, 2018.

[62] M Adouni, A Shirazi-Adl, and R Shirazi. Computational biodynamics of human knee joint in gait: from muscle forces to cartilage stresses. *Journal of biomechanics*, 45(12):2149–2156, 2012.

[63] TM Guess, H Liu, S Bhashyam, and G Thiagarajan. A multibody knee model with discrete cartilage prediction of tibio-femoral contact mechanics. *Computer methods in biomechanics and biomedical engineering*, 16(3):256–270, 2013.

[64] RL Lenhart, J Kaiser, CR Smith, and DG Thelen. Prediction and validation of load-dependent behavior of the tibiofemoral and patellofemoral joints during movement. *Annals of biomedical engineering*, 43(11):2675–2685, 2015.

[65] KB Shelburne, MG Pandy, FC Anderson, and MR Torry. Pattern of anterior cruciate ligament force in normal walking. *Journal of biomechanics*, 37(6):797–805, 2004.

[66] FH Netter. *Atlas of Human Anatomy E-Book*. Elsevier Health Sciences, 2017.

[67] IA Kapandji. The physiology of the joint. *lower limb.*, 2, 2010.

[68] M Pattnaik. *THE KNEE for Physiotherapists*. Jaypee Brothers, Medical Publishers Pvt. Limited, 2019.

[69] WE Weber. *Mechanik der menschlichen Gehwerkzeuge: eine anatomisch-physiologische Untersuchung*. Dieterich, 1836.

[70] A Steindler. *Kinesiology of the human body under normal and pathological conditions*. Thomas Springfield, 1955.

[71] Healthwise Staff. Menisci of the knee joint. url: https://myhealth.alberta.ca/Health/pages/conditions.aspx?hwid=tp12238, September 20, 2018.

[72] F Bonnel and JP Micaleff. Biomechanics of the ligaments of the human knee and of artificial ligaments. *Surgical and Radiologic Anatomy*, 10(3):221–227, 1988.

[73] G Strang and K Borre. *Linear algebra, geodesy, and GPS*. Siam, 1997.

[74] GB Arfken and HJ Weber. Mathematical methods for physicists, 1999.

[75] V Schomaker, J Waser, RE Marsh, , and G Bergman. To fit a plane or a line to a set of points by least squares. *Acta crystallographica*, 12(8):600–604, 1959.

[76] JM McCarthy and GS Soh. *Geometric design of linkages*, volume 11. Springer Science & Business Media, 2010.

[77] J Angeles. *Fundamentals of robotic mechanical systems*, volume 2. Springer, 2002.

[78] J Denavit and Hartenberg RS. A kinematic notation for low pair mechanisms based on matrices. *ASME J. Appl. Mech.*, 22:215–221, 1955.

[79] RP Paul. *Robot manipulators: mathematics, programming, and control: the computer control of robot manipulators*. Richard Paul, 1981.

[80] JJ Craig. Introduction to robotics machanics and control, addison wesley. 1986.

[81] Harvey Lipkin. A note on denavit-hartenberg notation in robotics. In *ASME 2005 International Design Engineering Technical Conferences and Computers and Information in Engineering Conference*, pages 921–926. American Society of Mechanical Engineers, 2005.

[82] Teledyne. Genie nano gige camera models. url: https://www.teledynedalsa.com/en/products/imaging/cameras/genie-nano-gige/.

[83] SJ Maybank and OD Faugeras. A theory of self-calibration of a moving camera. *International journal of computer vision*, 8(2):123–151, 1992.

[84] Jean-Yves Bouguet. Camera calibration toolbox for matlab. url: http://www.vision.caltech.edu/bouguetj/calibdoc/. Access: 03/28/2019.

[85] J Heikkila, O Silven, et al. A four-step camera calibration procedure with implicit image correction. In *cvpr*, volume 97, page 1106, 1997.

[86] JJ Moré. The levenberg-marquardt algorithm: implementation and theory. In *Numerical analysis*, pages 105–116. Springer, 1978.

[87] ISO International Organization for Standardization. Accuracy (trueness and precision) of measurement methods and results. url: https://www.iso.org/obp/ui/iso:std:iso:5725:-1:ed-1:v1:en, 12, 1994.

[88] Alex Lau. What are repeatability and reproducibility. url: https://www.astm.org/SNEWS/MA2009/datapointsma09.html, April 2019.

[89] ASTM American Society for Testing and Materials. A691m-18a, standard specification for carbon and alloy steel pipe, electric-fusion-welded for high-pressure service at high temperatures. url: http://www.astm.org/cgi-bin/resolver.cgi?A691A691M, 12, 1994.

[90] H Iwaki, V Pinskerova, and MAR Freeman. Tibiofemoral movement 1: the shapes and relative movements of the femur and tibia in the unloaded cadaver knee. *The Journal of bone and joint surgery. British volume*, 82(8):1189–1195, 2000.

[91] T Fukubayashi, PA Torzilli, MF Sherman, and RF Warren. An in vitro biomechanical evaluation of anterior-posterior motion of the knee. tibial displacement, rotation, and torque. *The Journal of bone and joint surgery. American volume*, 64(2):258–264, 1982.

[92] FM Griffin, K Math, GR Scuderi, JN Insall, and PL Poilvache. Anatomy of the epicondyles of the distal femur: Mri analysis of normal knees. *The Journal of arthroplasty*, 15(3):354–359, 2000.

[93] T Zantop, M Herbort, MJ. Raschke, FH Fu, and W Petersen. The role of the anteromedial and posterolateral bundles of the anterior cruciate ligament in anterior tibial translation and internal rotation. *The American Journal of Sports Medicine*, 35(2):223–227, 2007. PMID: 17158275.

[94] DL Gollehon, PA Torzilli, and RF Warren. The role of the posterolateral and cruciate ligaments in the stability of the human knee. a biomechanical study. *The Journal of bone and joint surgery. American volume*, 69(2):233–242, February 1987.

[95] RF LaPrade, TV Ly, FA Wentorf, and L Engebretsen. The posterolateral attachments of the knee. *The American journal of sports medicine*, 31(6):854–860, 2003.

[96] J Bradley, D FitzPatrick, D Daniel, T Shercliff, and J O'Connor. Orientation of the cruciate ligament in the sagittal plane. a method of predicting its length-change with flexion. *The Journal of bone and joint surgery. British volume*, 70(1):94–99, 1988.

[97] NF Friederich, W Müller, and WR O'Brien. Clinical application of biomechanic and functional anatomical findings of the knee joint. *Der Orthopade*, 21(1):41–50, 1992.

[98] JM Rico, LD Aguilera, J Gallardo, R Rodriguez, H Orozco, and JM Barrera. A more general mobility criterion for parallel platforms. *Journal of Mechanical Design*, 128(1):207–219, 2006.

[99] JM Rico and B Ravani. On mobility analysis of linkage using group theory. *Journal of Mechanical Design*, 125:70–80, 2003.

[100] D Aguilera, JM Rico, and J Gallardo. Computer implementation of an improved kutzbach-grubler mobility criterion. In *ASME 2002 International Design Engineering Technical Conferences and Computers and Information in Engineering Conference*, pages 549–557. American Society of Mechanical Engineers, 2002.

[101] JM Rico, J Gallardo, and B Ravani. Lie algebra and the mobility of kinematic chains. *Journal of Robotic Systems*, 20(8):477–499, 2003.

[102] CJ Wang, PS Walker, and B Wolf. The effects of flexion and rotation on the length patterns of the ligaments of the knee. *Journal of biomechanics*, 6(6):587–596, 1973.

[103] S Boyd and L Vandenberghe. *Convex optimization*. Cambridge university press, 2004.

Appendix A

Trueness study

The maximum and minimum errors of the trueness study at distances from 50 cm to 80 cm are listed in Table A.1.

Table A.1: Minimum and maximum errors of the trueness study at distances from 50 cm to 80 cm.

Distance	Direction	Displacement	Error (mm)	s (mm)
50 cm	Paralell	0.2 mm	0.0046085	0.0034145
		0.5 mm	0.0016697	0.0022707
	Perpendicular	0.2 mm	0.0182044	0.0122556
		0.5 mm	0.0104325	0.0125644
60 cm	Paralell	0.2 mm	0.0049685	0.0020032
		0.5 mm	0.0033765	0.0020787
	Perpendicular	0.2 mm	0.0227286	0.0194751
		0.5 mm	0.0159151	0.0184662
70 cm	Paralell	0.2 mm	0.0053802	0.0030745
		0.5 mm	0.0049134	0.0053840
	Perpendicular	0.2 mm	0.0386569	0.0174816
		0.5 mm	0.0262411	0.0181512
80 cm	Paralell	0.2 mm	0.0077891	0.0061106
		0.5 mm	0.0049776	0.0017505
	Perpendicular	0.2 mm	0.0474422	0.0269506
		0.5 mm	0.0322825	0.0340259

Appendix B

Camera calibration process

The camera calibration process consist on three main steps.

1. Take the images of the pattern: It is of great importance to have a set of images of the planar pattern in non-degenerate configurations covering the entire field of visibility of the camera, as reviewed in the **Section 4.3.2**. For the actual calibration process has been used a set of 30 images of the planar pattern at a distance of about 60 *cm* from the camera. In the Figure B.1 are shown 9 of those 30 images.

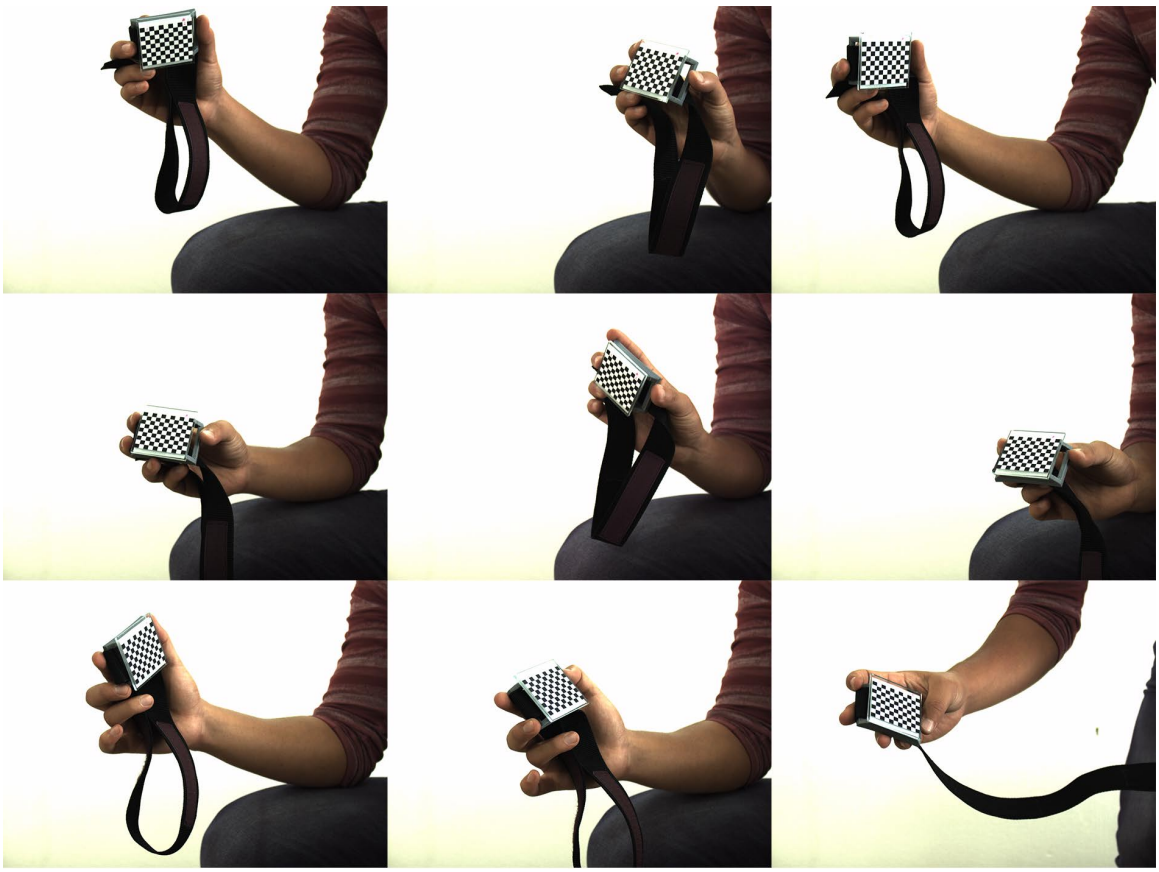

Figure B.1: 9 of the 30 images of the planar pattern used in the camera calibration process.

2. Compute the intrinsic and extrinsic parameters: This step is actually the camera calibration process which is composed mainly by the Zhang's algorithm described in the **Section 4.2.2**. This process is performed through the **Camera Calibration Toolbox** of Matlab® whose graphical user interface is shown in Figure B.2.

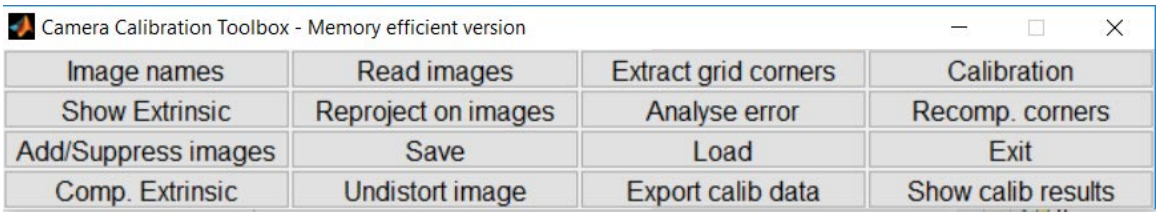

Figure B.2: Graphical user interface of the Camera Calibration Toolbox of Matlab®.

First, it is necessary the extraction of grid corners of the patterns and then push on the calibration button to compute the best homography matrix and therefore the best intrinsic and extrinsic parameters.

3. Analyse the error: Once the first two steps are completed, the camera calibration process is also complete, but in order to improve the results, it is possible to analyse the error performance, make some relevant changes and recalibrate. By pushing the analyse error button, a graph of the error performance will be displayed, see Figure B.3(a), the most scattered markers in the graph indicate the images with the biggest error. This graphic representation of the error allow us to see the images that require a more careful extraction of the grid corners or even those that must be suppressed of the camera calibration process.

A good camera calibration process must end with a graph of the error performance as the shown in Figure B.3(b), where the markers are distributed in a small space.

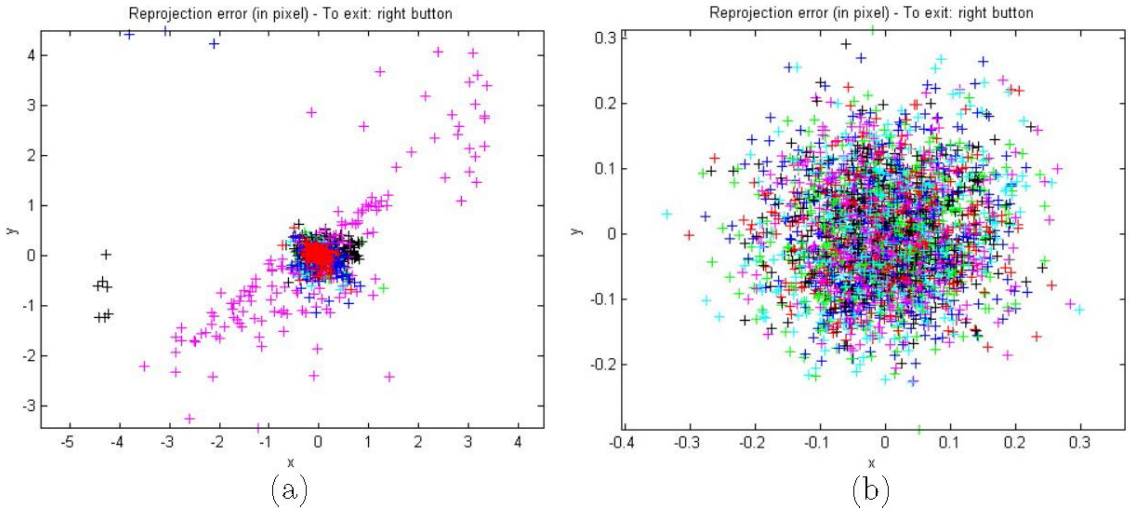

Figure B.3: Graphs of the error performance; (a) big error with scattered markers and (b) small error with markers distributed in a small space.

Steps 2 and 3 can be repeated any times, to obtain the best results.

For a more detailed camera calibration process by the Camera Calibration Toolbox of Matlab®, the readers are referred to [84].

Appendix C

Proof of the convex optimization problem

Let's rewrite the error function of the optimization problem as:

$$E_i(\boldsymbol{u}) = \sum_{j=1}^{n} \left(|\boldsymbol{a}_i^A - \boldsymbol{b}_{ij}^A| - L_i^* \right)^2 = \sum_{j=1}^{n} \left(d_{ij} \left(\boldsymbol{u} \right) \right)^2 \qquad i = 1, 2, 3, 4. \tag{C.1}$$

where $\boldsymbol{u} = \left[\boldsymbol{a}_i^f \; \boldsymbol{b}_i^t \right]^T = [x_{ai},\, y_{ai},\, z_{ai},\, x_{bi},\, y_{bi},\, z_{bi}]$ and:

$$\boldsymbol{a}_i^A = {}^A\mathbf{T}^f \boldsymbol{a}_i^f \qquad \boldsymbol{b}_{ij}^A = {}^A\mathbf{T}_j^t \boldsymbol{b}_i^t \tag{C.2}$$

The objective is to show that the function $E_i(\boldsymbol{u})$ is a convex function, based in the statement that an affine function that has the following form:

$$f(x) = Ax + b \tag{C.3}$$

is always a convex function[1].

Writing the vectors $\boldsymbol{a}_i^A$ and $\boldsymbol{b}_{ij}^A$ from (C.2) in the three components form, leads to:

$$\boldsymbol{a}_i^A = {}^A\mathbf{R}^f \boldsymbol{a}_i^f + {}^A\boldsymbol{t}^f \tag{C.4}$$

$$\boldsymbol{b}_{ij}^A = {}^A\mathbf{R}_j^t \, \boldsymbol{b}_i^t + {}^A\boldsymbol{t}_j^t \tag{C.5}$$

This shows that vectors $\boldsymbol{a}_i^A$ and $\boldsymbol{b}_{ij}^A$ are affine functions with respect to the vector of variables $\boldsymbol{u}$.

The spatial displacements ${}^A\mathbf{T}^f$ and ${}^A\mathbf{T}_j^t$ are constant matrices during the optimization problem, therefore, the rotation matrices ${}^A\mathbf{R}^f$ and ${}^A\mathbf{R}_j^t$, as well as the translation vectors ${}^A\boldsymbol{t}^f$ and ${}^A\boldsymbol{t}_j^t$ can be written as:

$${}^A\mathbf{R}^f = \begin{bmatrix} \alpha_{11} & \alpha_{12} & \alpha_{13} \\ \alpha_{21} & \alpha_{22} & \alpha_{23} \\ \alpha_{31} & \alpha_{32} & \alpha_{33} \end{bmatrix} \qquad {}^A\mathbf{R}_j^t = \begin{bmatrix} \beta_{11j} & \beta_{12j} & \beta_{13j} \\ \beta_{21j} & \beta_{22j} & \beta_{23j} \\ \beta_{31j} & \beta_{32j} & \beta_{33j} \end{bmatrix},$$

[1] For an in-depth treatment of the basic notions necessary to develop the proof, the readers are referred to [103]

and:

$$ {}^{A}\boldsymbol{t}^{f} = \begin{bmatrix} x_f \\ y_f \\ z_f \end{bmatrix} \qquad {}^{A}\boldsymbol{t}^{t}_{j} = \begin{bmatrix} x_{tj} \\ y_{tj} \\ z_{tj} \end{bmatrix}, $$

where all the elements of the matrices and vectors are real numbers.

Then, equations (C.4) and (C.5) can be rewritten as:

$$ \boldsymbol{a}^{A}_{i} = \begin{bmatrix} \alpha_{11}x_{ai} + \alpha_{12}y_{ai} + \alpha_{13}z_{ai} + x_f \\ \alpha_{21}x_{ai} + \alpha_{22}y_{ai} + \alpha_{23}z_{ai} + y_f \\ \alpha_{31}x_{ai} + \alpha_{32}y_{ai} + \alpha_{33}z_{ai} + z_f \end{bmatrix}, \tag{C.6} $$

$$ \boldsymbol{b}^{A}_{ij} = \begin{bmatrix} \beta_{11j}x_{bi} + \beta_{12j}y_{bi} + \beta_{13j}z_{bi} + x_{tj} \\ \beta_{21j}x_{bi} + \beta_{22j}y_{bi} + \beta_{23j}z_{bi} + y_{tj} \\ \beta_{31j}x_{bi} + \beta_{32j}y_{bi} + \beta_{33j}z_{bi} + z_{tj} \end{bmatrix}. \tag{C.7} $$

Now, let's analyze the difference $\boldsymbol{a}^{A}_{i} - \boldsymbol{b}^{A}_{ij}$ by its first component, as follows:

$$ \begin{aligned} \left[\boldsymbol{a}^{A}_{i} - \boldsymbol{b}^{A}_{ij}\right]_1 &= \alpha_{11}x_{ai} + \alpha_{12}y_{ai} + \alpha_{13}z_{ai} + x_f - (\beta_{11j}x_{bi} + \beta_{12j}y_{bi} + \beta_{13j}z_{bi} + x_{tj}) \\ &= [\alpha_{11},\, \alpha_{12},\, \alpha_{13},\, -\beta_{11j},\, -\beta_{12j},\, -\beta_{13j}]\,[x_{ai},\, y_{ai},\, z_{ai},\, x_{bi},\, y_{bi},\, z_{bi}]^{T} \\ &= \left[\left({}^{A}\mathbf{R}^{f}\right)_1 - \left({}^{A}\mathbf{R}^{t}_{j}\right)_1\right]\boldsymbol{u} + (x_f - x_{tj}), \end{aligned} \tag{C.8} $$

where $(\mathbf{R})_m$ is the notation for the m-row of the matrix $\mathbf{R}$.

As a result, the difference $\boldsymbol{a}^{A}_{i} - \boldsymbol{b}^{A}_{ij}$ can be written in a matrix form as:

$$ \boldsymbol{a}^{A}_{i} - \boldsymbol{b}^{A}_{ij} = \begin{bmatrix} \left({}^{A}\mathbf{R}^{f}\right)_1 - \left({}^{A}\mathbf{R}^{t}_{j}\right)_1 \\ \left({}^{A}\mathbf{R}^{f}\right)_2 - \left({}^{A}\mathbf{R}^{t}_{j}\right)_2 \\ \left({}^{A}\mathbf{R}^{f}\right)_3 - \left({}^{A}\mathbf{R}^{t}_{j}\right)_3 \end{bmatrix} \boldsymbol{u} + \begin{bmatrix} x_f - x_{tj} \\ y_f - y_{tj} \\ z_f - z_{tj} \end{bmatrix}. \tag{C.9} $$

Equation (C.9) is in the form given by (C.3) which is the proof that $\boldsymbol{a}^{A}_{i} - \boldsymbol{b}^{A}_{ij}$ is an affine function with respect to the vector of variables $\boldsymbol{u}$.

The modulus of the previous difference $|\boldsymbol{a}^{A}_{i} - \boldsymbol{b}^{A}_{ij}|$, is also a convex function since the modulus preserves convexity.

To prove convexity in the function, given by:

$$ f(\boldsymbol{u}) = |\boldsymbol{a}^{A}_{i} - \boldsymbol{b}^{A}_{ij}| - L^{*}_{i}, \tag{C.10} $$

let's define the two additional convex functions:

$$ h(\boldsymbol{r}) = \mathbf{I}\boldsymbol{r} - L^{*}_{i} \qquad \text{and} \qquad g(\boldsymbol{u}) = |\boldsymbol{a}^{A}_{i} - \boldsymbol{b}^{A}_{ij}| $$

It is easy to see that $f(\boldsymbol{u})$ can be defined through $h(\boldsymbol{r})$ and $g(\boldsymbol{u})$, by the function composition $f(\boldsymbol{u}) = h \circ g = h(g(\boldsymbol{u}))$.

A function composition is convex if both functions involved are convex.

Function $\left(|\boldsymbol{a}^{A}_{i} - \boldsymbol{b}^{A}_{ij}| - L^{*}_{i}\right)^2$ is convex because it is a scalar power of a convex function, and scalar power preserves convexity.

Finally, function $E_i(\boldsymbol{u}) = \sum_{j=1}^{n}\left(|\boldsymbol{a}^{A}_{i} - \boldsymbol{b}^{A}_{ij}| - L^{*}_{i}\right)^2$ is convex because it is a sum of convex functions and the addition preserves convexity.